Ph.D. Dissertation of Engineering

Monitoring vegetation changes by enhancing the spatiotemporal resolution of satellite imagery

시공간 해상도 향상을 통한 식생 변화 모니터링

February 2023

Graduate School
Seoul National University
Interdisciplinary Program in Landscape Architecture

Juwon Kong

Monitoring vegetation changes by enhancing the spatiotemporal resolution of satellite imagery

Advisor: Youngryel Ryu

Submitting a Ph.D. Dissertation of
Engineering

January 2023

Graduate School
Seoul National University
Interdisciplinary Program in Landscape Architecture

Juwon Kong

Confirming the Ph.D. Dissertation written by
Juwon Kong

January 2023

Chair _____(Seal)
Vice Chair _____(Seal)
Examiner _____(Seal)
Examiner _____(Seal)
Examiner _____(Seal)

Abstract

Monitoring vegetation changes by enhancing spatial and temporal resolution of satellite imagery

Juwon Kong

Interdisciplinary Program in Landscape Architecture

Graduate School

Seoul National University

Supervised by Professor Youngryel Ryu

Monitoring changes in terrestrial vegetation is essential to understanding interactions between atmosphere and biosphere, especially terrestrial ecosystem. To this end, satellite remote sensing offer maps for examining land surface in different scales. However, the detailed information was hindered under the clouds or limited by the spatial resolution of satellite imagery. Moreover, the impacts of spatial and temporal resolution in photosynthesis monitoring were not fully revealed.

In this dissertation, I aimed to enhance the spatial and temporal resolution of satellite imagery towards daily gap-free vegetation maps with high spatial resolution. In order to expand vegetation change monitoring in time and space using high-resolution satellite images, I 1) improved temporal resolution of satellite dataset through image fusion using geostationary satellites, 2) improved spatial resolution of satellite dataset using generative adversarial networks, and 3) showed the use of high spatiotemporal resolution maps for monitoring plant photosynthesis especially over heterogeneous

landscapes. With the advent of new techniques in satellite remote sensing, current and past datasets can be fully utilized for monitoring vegetation changes in the respect of spatial and temporal resolution.

In Chapter 2, I developed the integrated system that implemented geostationary satellite products in the spatiotemporal image fusion method for monitoring canopy photosynthesis. The integrated system contains the series of process (i.e., cloud masking, nadir bidirectional reflectance function adjustment, spatial registration, spatiotemporal image fusion, spatial gap-filling, temporal-gap-filling). I conducted the evaluation of the integrated system over heterogeneous rice paddy landscape where the drastic land cover changes were caused by cultivation management and deciduous forest where consecutive changes occurred in time. The results showed that the integrated system well predict *in situ* measurements without data gaps (R^2 = 0.71, relative bias = 5.64% at rice paddy site; R^2 = 0.79, relative bias = −13.8% at deciduous forest site). The integrated system gradually improved the spatiotemporal resolution of vegetation maps, reducing the underestimation of *in situ* measurements, especially during peak growing season. Since the integrated system generates daily canopy photosynthesis maps for monitoring dynamics among regions of interest worldwide with high spatial resolution. I anticipate future efforts to reveal the hindered information by the limited spatial and temporal resolution of satellite imagery.

Detailed spatial representations of terrestrial vegetation are essential for precision agricultural applications and the monitoring of land cover changes in heterogeneous landscapes. The advent of satellite-based remote sensing has facilitated daily observations of the Earth's surface with high spatial resolution. In particular, a data

fusion product such as Planet Fusion has realized the delivery of daily, gap-free surface reflectance data with 3-m pixel resolution through full utilization of relatively recent (i.e., 2018-) CubeSat constellation data. However, the spatial resolution of past satellite sensors (i.e., 30-60 m for Landsat) has restricted the detailed spatial analysis of past changes in vegetation. In Chapter 3, to overcome the spatial resolution constraint of Landsat data for long-term vegetation monitoring, we propose a dual remote-sensing super-resolution generative adversarial network (dual RSS-GAN) combining Planet Fusion and Landsat 8 data to simulate spatially enhanced long-term time-series of the normalized difference vegetation index (NDVI) and near-infrared reflectance from vegetation (NIRv). We evaluated the performance of the dual RSS-GAN against in situ tower-based continuous measurements (up to 8 years) and remotely piloted aerial system-based maps of cropland and deciduous forest in the Republic of Korea. The dual RSS-GAN enhanced spatial representations in Landsat 8 images and captured seasonal variation in vegetation indices ($R2 > 0.95$, for the dual RSS-GAN maps vs. in situ data from all sites). Overall, the dual RSS-GAN reduced Landsat 8 vegetation index underestimations compared with in situ measurements; relative bias values of NDVI ranged from -3.2% to 1.2% and -12.4% to -3.7% for the dual RSS-GAN and Landsat 8, respectively. This improvement was caused by spatial enhancement through the dual RSS-GAN, which captured fine-scale information from Planet Fusion. This study presents a new approach for the restoration of hidden sub-pixel spatial information in Landsat images.

Mapping canopy photosynthesis in both high spatial and temporal resolution is essential for carbon cycle monitoring in heterogeneous areas. However, well established satellites in sun-synchronous

orbits such as Sentinel-2, Landsat and MODIS can only provide either high spatial or high temporal resolution but not both. Recently established CubeSat satellite constellations have created an opportunity to overcome this resolution trade-off. In particular, Planet Fusion allows full utilization of the CubeSat data resolution and coverage while maintaining high radiometric quality. In Chapter 4, I used the Planet Fusion surface reflectance product to calculate daily, 3-m resolution, gap-free maps of the near-infrared radiation reflected from vegetation (NIRvP). I then evaluated the performance of these NIRvP maps for estimating canopy photosynthesis by comparing with data from a flux tower network in Sacramento-San Joaquin Delta, California, USA. Overall, NIRvP maps captured temporal variations in canopy photosynthesis of individual sites, despite changes in water extent in the wetlands and frequent mowing in the crop fields. When combining data from all sites, however, I found that robust agreement between NIRvP maps and canopy photosynthesis could only be achieved when matching NIRvP maps to the flux tower footprints. In this case of matched footprints, NIRvP maps showed considerably better performance than *in situ* NIRvP in estimating canopy photosynthesis both for daily sum and data around the time of satellite overpass (R^2 = 0.78 vs. 0.60, for maps vs. *in situ* for the satellite overpass time case). This difference in performance was mostly due to the higher degree of consistency in slopes of NIRvP-canopy photosynthesis relationships across the study sites for flux tower footprint-matched maps. Our results show the importance of matching satellite observations to the flux tower footprint and demonstrate the potential of CubeSat constellation imagery to monitor canopy photosynthesis remotely at high spatio-temporal resolution.

Keyword: Super-resolution, Satellite remote sensing, Canopy photosynthesis, CubeSat, Geostationary satellite, Generative adversarial network

Student Number: 2019-39602

Table of Contents

List of Figures

Chapter 2

Chapter 3

Chapter 4

List of Tables

Chapter 2

Chapter 3

Chapter 4

Publications

Please note that portions of this dissertation have been reprinted, with permission, from previously published materials. Chapters 3 have been submitted to ISPRS Journal of Photogrammetry and Remote Sensing, Elsevier. Chapter 4 has been reprinted from Agricultural and Forest Meteorology, Elsevier. Both Chapter 3 and 4 were licensed under a Creative Commons Attribution 4.0 International License.

1. Kong, J., Ryu, Y., Liu, J., Dechant, B., Rey-Sanchez, C., Shortt, R., Szutu, D., Verfaillie, J., Houborg, R., & Baldocchi, D.D. (2022). Matching high resolution satellite data and flux tower footprints improves their agreement in photosynthesis estimates. Agricultural and Forest Meteorology, 316, 108878
2. Kong, J., Ryu, Y., Zhong, Z., Jeong, S., Choi, W., Kim, J., Houborg, R. (2023) Super-resolution of historic Landsat imagery using a dual generative adversarial network (GAN) model with CubeSat constellation imagery for monitoring vegetation changes, ISPRS Journal of Photogrammetry and Remote Sensing, (Under review).

Publication included in this dissertation was conducted with support of the National Research Foundation of Korea (NRF-2019R1A2C2084626), National Institute of Forest Science (FM0103-2021-01, 564 FM0103-2021-02), and the Cooperative Research Program for Agriculture Science & Technology Development (Project No. PJ01475502), Rural Development Administration, Republic of Korea.

Chapter 1. Introduction

1. Background

High spatial and temporal resolution satellite imagery is in demand for monitoring vegetation changes over heterogeneous landscape. Although daily satellite imagery with high spatial resolution is not available for historical data, previous studies showed some clues to enhance the spatial and temporal resolution of satellite dataset.

1.1 Daily gap-free surface reflectance using geostationary satellite products

In space-born observation, geostationary satellites can harmonize an uneasy mix of terrestrial monitoring and clouds. While clouds cause inevitable data gaps in optical satellite products that monitor terrestrial surfaces (Ju and Roy, 2008), geostationary satellites detect clouds for continuous meteorological observation (Bessho et al., 2016; Chung et al., 2020; McCorkel et al., 2020). In these disparate purposes of satellites, an opportunity for gap-filled satellite products can arise from continuous observation itself (Khan et al., 2021; Xiao et al., 2021). Compared to snapshots from polar-orbiting satellites, geostationary satellite products have the potential to measure surface reflectance as the clouds flow with time (Hashimoto et al., 2021; Miura et al., 2019; Yan et al., 2016a; Yeom et al., 2018). These non-cloudy measurements from the geostationary satellite products improved our understanding of land surface seasonal dynamics (Hashimoto et al., 2021; Miura et al., 2019; Tran et al., 2020) and phenology detection (Wheeler and Dietze, 2021). In heterogeneous areas, nonetheless, the spatial resolution of geostationary products is not enough to monitor both phenological

and land cover changes in landscape scale (Atkinson and Curran, 1995; Roth et al., 2015; Turner et al., 1989; Woodcock and Strahler, 1987). Moreover, diurnal changes of sun–target–sensor geometry affect the retrieval of the surface reflectance (Morton et al., 2014; Proud et al., 2014; Yeom et al., 2020) when applied in vegetation monitoring (Feng et al., 2002; Fensholt et al., 2010; Fensholt et al., 2006; Seong et al., 2020). Although previous studies attempted to solve each limitation (He et al., 2019; Lee et al., 2020; Wu et al., 2015), it has not been an integrated implementation to generate daily gap–filled surface reflectance products with high spatial resolution using geostationary satellite products.

1.2 Monitoring past vegetation changes with high–spatial–resolution

High–spatial–resolution monitoring of changes in terrestrial vegetation is increasingly important for precision agricultural applications and for the quantification of changes in land cover, among other uses. In the context of concerns about increasing food demand caused by population growth (Gebbers and Adamchuk, 2010), precision agriculture reduces variations in temporal yield related to yield stability and increases crop resilience to climate change (Yost et al., 2017). Precision agriculture requires high–spatial–resolution data for site–specific information, particularly over heterogeneous landscapes (Duveiller and Defourny, 2010; Gebbers and Adamchuk, 2010; Sishodia et al., 2020). The monitoring of changes in land cover is essential for quantifying anthropogenic impacts on climate change (Pielke Sr, 2005) because such changes have both biogeochemical

and biogeophysical effects on the global climate (Feddema et al., 2005). High-spatial-resolution time-series data can be used to detect changes in land cover with less uncertainty associated with misclassification (Shendryk et al., 2019).

1.3 High spatiotemporal resolution vegetation photosynthesis maps

Being able to estimate terrestrial gross primary productivity (GPP) accurately with remote sensing techniques is important for monitoring climate change effects, vegetation responses to environmental extremes and agricultural applications, among other uses. Apart from the chosen approach to estimate GPP from remote sensing variables, the spatial and temporal resolution of the data are important. High spatial resolution satellite data are needed for agricultural applications and monitoring of heterogeneous natural ecosystems. For example, small-scale agricultural fields, which can be fine scale heterogeneous ecosystems, require spatial GPP details to distinguish boundaries between fields and to understand sub-field variation in crop growth (Duveiller and Defourny, 2010; Houborg and McCabe, 2016; Kimm et al., 2020). High temporal resolution is also important within short periods during transition season or extreme environmental events such as droughts.

2. Purpose of Research

In this dissertation, I aimed to enhance the spatial and temporal resolution of satellite dataset in order to expand vegetation change monitoring in time and space. For that, I generated canopy photosynthesis maps with high spatiotemporal resolution, extending spatial resolution of past dataset towards long-term vegetation

monitoring. With the high-resolution canopy photosynthesis maps, I quantified the impact of spatial and temporal resolution of maps when spatially upscaling in situ measurements.

In Chapter 2, I implemented geostationary satellite products in the image fusion method towards daily gap-free surface reflectance product in visible (i.e., red, green, and blue) and near-infrared (VNIR) bands with high spatial resolution. For that, I integrated the series of processes that include cloud masking, nadir BRDF adjustment, spatial registration, spatiotemporal image fusion, spatial gap-filling, and temporal gap-filling.

In Chapter 3, I present an approach for overcoming the spatial resolution gap between past and new datasets to generate consistent long-term terrestrial vegetation records. The dual generative adversarial network (GAN) model uses original and downscaled new datasets to train GAN models; it uses the output of one GAN as input for another model. I designed the dual GAN to improve spatial differences between past and new datasets in a sequential manner, beginning with the generation of long-term vegetation index maps with high spatial resolution.

In Chapter 4, I facilitated daily, 3 m canopy photosynthesis maps from CubeSat NIRvP to link the satellite-based GPP to the tower observations, considering different scenarios. In particular, I attempted to answer the scientific questions about the impact of matching daily flux tower footprints with high resolution canopy photosynthesis maps.

Chapter 2. Generating daily gap-filled BRDF adjusted surface reflectance product at 10 m resolution using geostationary satellite product for monitoring daily canopy photosynthesis

1. Introduction

Utilizing the satellite products from different platforms can solve the weakness of geostationary satellite products in the spatial details. As Earth observations from single-satellite have constraints on either spatial resolution or revisit frequency due to the trade-off between pixel and swath width, researchers in environmental science need to select the satellite products based on the purposes. Among the widely used polar-orbiting satellites, for instance, the MODerate resolution Imaging Spectroradiometer (MODIS) can provide daily product with coarse spatial resolution on the global scale (Justice et al., 2002) when Landsat 8 Operational Land Imager (OLI) can acquire the 16-day product with relatively fine resolution over the same area (Roy et al., 2014a). Thus, the coarse spatial resolution of geostationary satellite products caused by the coninuous observation limits sensing spatial changes of the Earth in landscape-scale, mainly where spatial heterogeneity occurs within a pixel. One of the solutions to overcome the spatiotemporal limitation is the fusion of daily temporal resolution products (e.g., MODIS) with higher spatial resolution products (e.g., Landsat 8 and Sentinel 2) (Pohl and Van Genderen, 1998; Zhu et al., 2018). For example, the Flexible Spatiotemporal DAta Fusion (FSDAF) (Zhu et al., 2016) improved the performance of image fusion products by combining the ideas from weighted function-based methods (Feng et al., 2006; Zhu et al.,

2010), unmixing-based methods (Gevaert and García-Haro, 2015; Zhukov et al., 1999), and spatial interpolation. In addition, FSDAF predicted the spatial and temporal variations of in situ dataset measured from the hyper-spectrometer in a heterogeneous rice paddy landscape (Kong et al., 2021). Furthermore, SFSDAF enhanced FSDAF method by considering sub-pixel class fraction change information (Li et al., 2020). Another solution could be harmonizing the products from the different satellites into a single dataset to complement the data gaps (Claverie et al., 2018; Frantz, 2019a). Particularly, the processes that include spatial co-registration between the scenes (Gao et al., 2009; Scheffler et al., 2017; Yan et al., 2016b), spectral adjustment of each band (Houborg and McCabe, 2018a; Shang and Zhu, 2019; Wang et al., 2020a) enable us to achieve seamless products. When facilitating the image fusion of satellite products for enhancing the spatial resolution of geostationary products, the rigorous pre-processing, which includes atmospheric correction (Duffy et al., 2019; Lyapustin et al., 2011; Vermote et al., 1997) and cloud masking (Qiu et al., 2019; Zhu and Helmer, 2018), is an essential prerequisite (Choi et al., 2013; Claverie et al., 2018).

Using diurnal changes of solar angles in continuous observations can reduce the effect of sun-target-sensor geometry on daily surface reflectance products. As sun-target-sensor geometry influences the instantaneous surface reflectance that depends on the land surface structure and optical properties, surface reflectance products from geostationary satellites vary within a day (Fensholt et al., 2010; He et al., 2019). When implementing a bidirectional reflectance distribution function (BRDF) using the varied

observations from different solar angles within a day, the daily surface reflectance at specific solar and viewing angles can be retrieved (He et al., 2019; Lee et al., 2020; Proud et al., 2014; Wheeler and Dietze, 2019; Yeom et al., 2020). On the other hand, the BRDF adjusted daily surface reflectance products from polar-orbiting satellite, which are the composite of daily snapshots over several days (Schaaf et al., 2002; Wang et al., 2018b), has a limitation on monitoring the land surface changes in that period (Fensholt et al., 2010). In the results of the semiempirical BRDF model (e.g., RossThick LiSparse (RTLSR) model (Li and Strahler, 1986; Lucht et al., 2000; Wanner et al., 1995) and Roujean model (Roujean et al., 1992)), for example, the geostationary satellite products better-captured terrestrial vegetation changes than polar-orbiting satellite products (Feng et al., 2006; Fensholt et al., 2010; Proud et al., 2014).

Towards the gap-free product, the spatial and temporal gap-filling processes is an integral part of the robustness of daily surface reflectance product from geostationary products. Even if the geostationary satellites continuously observe the Earth's surface, clouds and shadows will affect the data gaps or quality of satellite products, especially during the rainy season (Hashimoto et al., 2021). Unlike homogeneous areas, where simple interpolation methods can resolve missing-data problems, restoring the cloud-contaminated pixels is problematic over heterogeneous areas (Pringle et al., 2009; Weiss et al., 2014). As enhancing the spatial resolution of surface reflectance product magnify both homogeneous and heterogeneous areas (Zhu et al., 2010), the spatial gap-filling method should be adequate to predict small or narrow objects (Chen et al., 2011b; Zhu et al., 2012). For instance, the Neighborhood Similar Pixel

Interpolator (NSPI) (Chen et al., 2011b), which can fill the spatial gaps in the images in heterogeneous regions, was improved to Geostatistical NSPI (GNSPI) (Zhu et al., 2012) by embedding the geostatistical theory. In aspect of time, regression methods can temporally interpolate missing pixels using the pixels from different times, particularly, when temporal gaps between the data were short, surface reflectance tend to change linearly (Luo et al., 2018; Luo et al., 2020). Moreover, Gaussian process regression (GPR) – which uses the basis of multivariable normal distribution, nonparametric approach, and joint and conditional probability – can predict the nonlinear variation of land surfaces in time (Adeluyi et al., 2021; Yin et al., 2019). Thus, spatially and temporally gap-filled geostationary satellite products can give an insight into Earth surface processes, which cannot be recognized from satellite products with data gaps.

In this paper, I implemented geostationary satellite products in the image fusion method towards daily gap-free surface reflectance product in visible (i.e., red, green, and blue) and near-infrared (VNIR) bands with high spatial resolution. For that, I integrated the series of processes that include cloud masking (i.e., Function of mask; Fmask), nadir BRDF adjustment (i.e., RTLSR model), spatial registration (i.e., An Automated and Robust Open-Source Image Co-Registration Software; AROSICS), spatiotemporal image fusion (i.e., SFSDAF), spatial gap-filling (i.e., NPSI), and temporal gap-filling (i.e., GPR). I decided to utilize the advantages of both spatiotemporal image fusion (i.e., SFSDAF) in large clouds and of gap-filling method (i.e., NPSI) in spatially small cloud patches (Shu et al., 2022) rather than choosing between them. In the integrated process, I used surface reflectance products from three polar-orbiting satellites (i.e.,

Sentinel 2, Landsat 8, and MODIS) and a geostationary satellite (i.e., Geo-KOMPSAT 2A; GK2A). The results are from heterogeneous rice paddy landscape where the drastic land cover changes were caused by cultivation management like irrigation and harvesting, and deciduous forest where consecutive changes occurred in time. For rigorous assessment, I evaluated the results in both space and time using hyperspectral maps derived from unmanned aerial vehicle (UAV) and in situ tower-based continuous spectral measurements. Our key scientific question is how much the daily gap-free surface reflectance products empower us to sense the changes of the Earth in space and time.

2. Methods

2.1 Study sites

To evaluate the performance of daily gap−free surface reflectance product, I included cropland (rice) and forest sites (deciduous forest; needleleaf forest) in Republic of Korea, which include flux towers registered in the Korea Flux Network (Figure 2.1; Table 2.1). The rice paddy site (Site ID: CRK) is predominantly covered by rice (Oryza sativa L. ssp. Japonica) and flat with a mean canopy height of less than 1m. (Dechant et al., 2020; Dechant et al., 2019; Huang et al., 2018; Hwang et al., 2020; Yang et al., 2018). The deciduous forest (Site ID: GDK) is covered by are Konara oak (Quercus spp.) and hornbeam (Carpinus spp), which are the dominant overstory species, in mountain with a mean canopy height of approximately 18 m (Cho et al., 2021; Ryu et al., 2008; Ryu et al., 2014). The climates of sites are temperate monsoon climate and clouds are frequently cover the study sites with high precipitation during June to August.

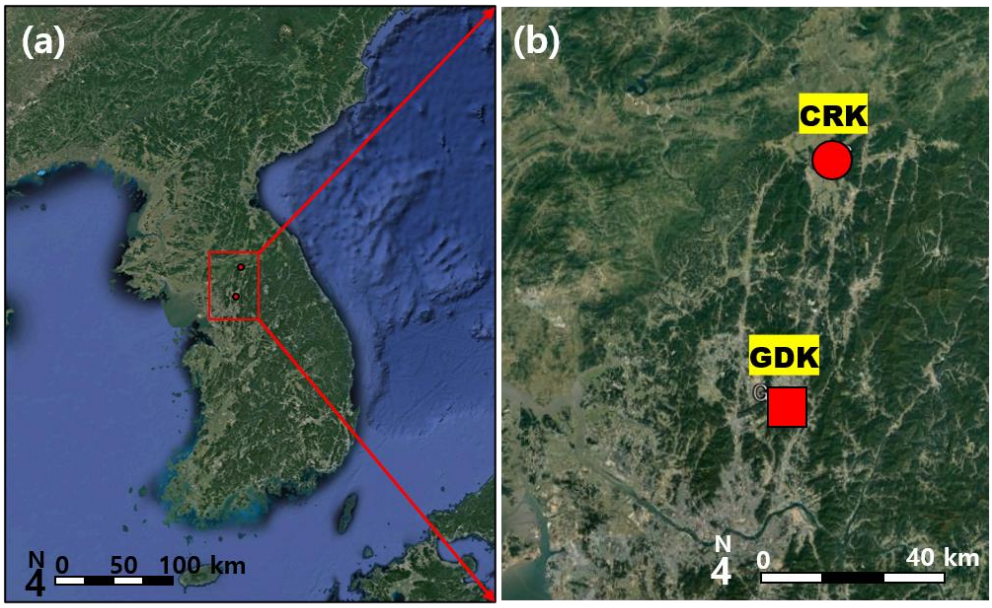

Figure 2.1 (a) Map of the Korean peninsula (image source: Google Earth) indicating the location of the study area. (b) Locations of study sites and flux towers over cropland (CRK, red circle) and deciduous forest (GDK, yellow square). Further details are provided in Table 2.1.

Table 2.1 List of study sites. Planet functional types are cropland (CRO) and deciduous broadleaf forest (DBF). Spectroradiometer position indicates sensor heights (m) from the ground.

Site name (Site ID)	Type	Spectro radiometer position (m)	Canopy height (m)	Latitude (° N) Longitude (° E)
Cheorwon Rice Paddy (CRK)	CRO	5 m	0.5 m	38.2013, 127.2507
Gwangreung Deciduous Forest (GDK)	DBF	40 m	18 m	37.7487, 127.1489

2.2 In situ measurements

To evaluate daily gap-free surface reflectance products, I compared them with *in situ* surface reflectance data from tower-based hyperspectral and multi-spectral spectroradiometers and remotely piloted aviation system-based hyperspectral imager. From tower-based hyperspectral spectroradiometer (Jaz, Ocean Optics, Dunedin, FL, USA over rice paddy; Frame, Ocean Insight, Orlando, FL, USA over deciduous forest), I continuously measured canopy reflectance around each flux tower. Fiber optics with cosine correctors (Ocean Insight, Orlando, FL, USA) were equipped in hyperspectral spectroradiometers to measure bi-hemispheric reflectance. Additionally, LED-based multi-spectral spectroradiometer (Kim et al., 2019; Ryu et al., 2010; Ryu et al., 2014) measured bi-hemispheric reflectance in deciduous forest (GDK). As satellite products provide the bidirectional reflectance factor, I used vegetation indices (e.g., Normalized Difference Vegetation Index (NDVI), approximated near infrared (NIR) reflectance from vegetation (NIRv)), which showed negligible impact on difference reflectance quantities (Feng et al., 2002; Kong et al., 2021) to evaluate daily gap-free products. Based on difference between the sensor height from the ground and canopy height, I approximate the area of 80 % upwelling irradiance of bi-hemispherical measurements. The estimated diameters of hyperspectral spectroradiometer footprints were 19.3 m (CRK) and 17.2 m (GDK). To measure the bidirectional reflectance factor over the sites, I used hyperspectral imager (Nano-hyperspec, Analytik, Swavesey, UK) on remotely piloted aviation systems (DJI-600 pro and DJI-RONIN MX, Shenzhen, People's Republic of China).

Hyperspectral imager scanned around 250 m by 250 m area centered on the flux towers of CRK and GDK (Figure 2.2). Further details were in original dataset paper (Choi et. al., in prep).

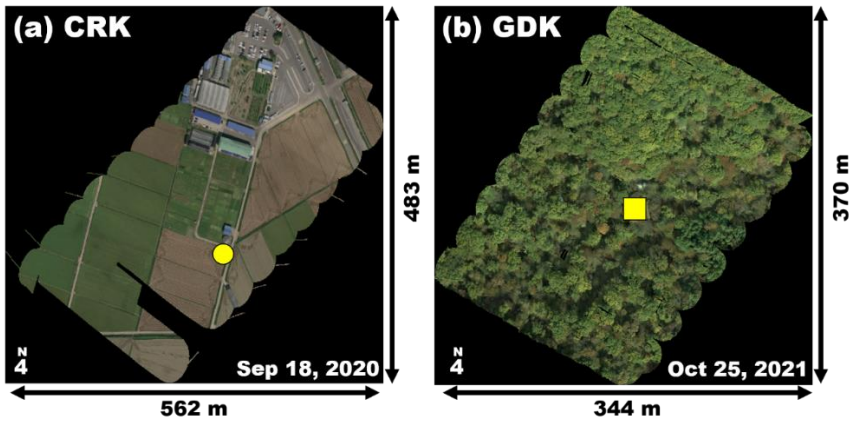

Figure 2.2 *In situ* hyperspectral images (projection, WGS84/UTM zone 52N; red-green-black (RGB) true color; 5-cm resolution). (a) Cropland (CRK) and (b) deciduous forest (GDK). Yellow symbols indicate flux tower locations. Black shading on the CRK map indicates data excluded from the final analysis.

2.3 Satellite products

Satellite data from different platform and sensors were used to generate daily gap-free surface reflectance products in VNIR bands (Table 2.2). I set the study period during 1 Jan 2020 to 31 Dec 2021. Geostationary-Korea Multi-Purpose Satellite-2 (GK2A) Advanced Meteorological Imager (AMI) scanned from East Asia to Australia with 0.5 km to 2 km resolution every 2 to 10 minutes depending on the region (Chung et al., 2020). I used GK2A AMI level 2 fixed viewing BRDF-adjusted reflectance (FVBAR) product with 2 km resolution, which is the daily normalized the reflectance that considered attribute of geostationary satellite observation (Lee et al., 2020; Yeom and Kim, 2013). GK2A FVBAR daily surface reflectance

data were computed from BRDF model (i.e., Roujean model) inversion using cloud-free pixels in 10-minute interval GK2A data within five days before the day of interest. From Terra and Aqua MODIS data, daily Nadir view BRDF-adjusted reflectance (NBAR) product were retrieved (MCD43A4; Schaaf et al. (2002)) with 500 m resolution. The inputs for daily MODIS NBAR product were the possible MODIS pixels within 16-day range in center of the day of interest. When sufficient (more than seven) high quality (e.g., cloud-free) observations were available for semiempirical BRDF model (i.e., RTLSR model), a full BRDF inversion retrieval can be attempted. I used only pixels from full BRDF inversion retrievals in MCD43A4 product (collection version 6) as an input for the integrated system. Landsat 8 OLI (Roy et al., 2014a) provide 16-day product with 30 m resolution. I used level 2 (Surface reflectance) and angle parameter from Landsat 8 collection 2 level 1 (Top-of-atmosphere; TOA) to generate Landsat 8 NBAR data. Sentinel 2 A/B Multispectral Instrument (MSI) (Drusch et al., 2012b) provide 5-day product with 10 m resolution for VNIR bands (band 2, 3, 4, and 8). I generated Sentinel 2 NBAR data using level 2 surface reflectance and angle parameter from Sentinel 2 A/B level 1 TOA.

Table 2.2 List of satellite data for generating daily gap-free surface reflectance products. Satellite data were measured from Geostationary-Korea Multi-Purpose Satellite-2 (GK2A) Advanced Meteorological Imager (AMI), Terra and Aqua Moderate Resolution Imaging Spectroradiometer (MODIS), Landsat 8 Operational Land Imager (OLI), and Sentinel 2 Multispectral Instrument (MSI). Spatial resolutions are for visible (red, green, and blue) and near-infrared bands.

Satellite sensor	Data	Spatial resolution	Temporal resolution	Band number for VNIR
GK2A AMI	Fixed viewing BRDF-adjusted reflectance (FVBAR)	2 km	Daily	Blue = 1 Green = 2 Red = 3 NIR = 4
MODIS	Nadir Bidirectional Reflectance Distribution Function (BRDF)-Adjusted Reflectance (NBAR)	500 m	Daily	Blue = 3 Green = 4 Red = 1 NIR = 2
Landsat 8 OLI	Level1 (Top-of-atmosphere), Level2 (Surface reflectance)	30 m	16 days	Blue = 2 Green = 3 Red = 4 NIR = 5
Sentinel 2 MSI	Level1 (Top-of-atmosphere), Level2 (Surface reflectance)	10 m	5 days	Blue = 2 Green = 3 Red = 4 NIR = 8

2.4 Integrated system

To implement the integrated system, I designed the process including the preprocessing forcing data for image fusion methods (Figure 2.3). The system has three steps: 1) Preprocessing the coarse spatial resolution data (i.e., GK2A and MODIS), 2) Preprocessing the fine spatial resolution data (Landsat 8 and Sentinel 2), and 3) Image fusion and gap-filling process.

2.4.1 Step 1: Daily gap-free 480 m resolution data

I combined daily GK2A FVBAR and MODIS NBAR data into one dataset to prepare daily gap-free 480 m resolution data. First, I cropped the region of interest in GK2A FVBAR and MODIS NBAR data that contains only complete pixels in rather than segmented pixels on the boundary of the region of interest. Second, the coordinates of GK2A FVBAR and MODIS NBAR were re-projected to that of fine resolution data (e.g., WGS84 UTM 52N, ESPG:32652) and resampled the pixel size of NBAR data into 480 m by using cubic spline interpolation method in geospatial data abstraction library (GDAL). For image fusion processing, the ratio of the pixel size of coarse resolution to that of fine resolution should be integer. I set 480 m, which is the common multiple of pixel sizes of fine spatial resolution data (i.e., 30 m for Landsat 8 and 10 m for Sentinel 2) near the pixel size of MODIS data (i.e., 500 m), as the coarse spatial resolution dataset. Third, missing pixels of daily MODIS NBAR (480 m) due to insufficient high-quality observations for BRDF inversion retrievals were substituted by pixels of daily GK2A FVBAR (480 m) as GK2A have enough observations for generating almost gap-free daily FVBAR within five days before the day of interest. Last, I used

Gaussian process regression (GPR) model (fitrgp; MATLAB; The MathWorks, Inc., Natick, MA, USA) on time-series dataset at each location to fill the remained gaps. Gaussian process (Rasmussen, 2004) is an example of random (stochastic) process that has random variables following the linear combination of multivariable normal distribution. When the nonlinear function that represent the dataset in time is a probability model with error bar, GPR estimates the normal distribution of that function with mean function and covariance (=kernel) function. After optimizing the hyper-parameters that controls functional covariance, I can use that posterior mean and covariance to predict the values in gaps. To minimize the prediction error, I selected the options of fitrgp function as follows: an exact GPR method to make prediction, a squared exponential kernel function, and the unconstrained nonlinear optimization for parameter estimation (i.e, 'fminuc' in fitrgp function). When the number of pixels were insufficient for GPR model, I estimated missing values by smoothing (i.e., robust quadratic regression method) nearby pixels within the window whose sizes were computed by own heuristic basis (smoothdata; MATLAB; The MathWorks, Inc., Natick, MA, USA).

2.4.2 Step 2: Landsat 8 and Sentinel 2 preprocessing

I prepared the cloud mask using automated cloud and cloud shadow detection algorithm (i.e., Fmask 4.6, https://github.com/GERSL/Fmask; (Qiu et al., 2019)) to filter out low quality pixels in Landsat 8 and Sentinel 2 level 2 data. Fmask, which is a widely used physical-rule-based algorithm, derives the physical characteristics of cloud (e.g., white, bright, cold, and high in elevation) using different spectral bands and auxiliary data (i.e., Global Surface

Water Occurrence data and Digital Elevation Model data). Then, Fmask classifies pixels of Landsat 8 and Sentinel 2 into land and water or distinguishes snow/ice from clouds. At the same time, I generated Landsat 8 and Sentinel 2 NBAR data using RTLSR model with kernel parameters written in Roy et al. (2016b) and Roy et al. (2017) as official NBAR products are not available over the study sites. The kernel parameters were derived from MODIS spectral BRDF model parameters of MODIS bands that were spectrally equivalent to Landsat 8 and Sentinel 2 bands. I extracted angle parameters (i.e., VZA, SZA, RAA) of Landsat 8 and Sentinel 2 from Landsat 8 level 1 data using Landsat 8 Angle Creation Tool and metadata of Sentinel 2 level 1 data in MTL format, respectively. Additionally, I conducted geospatial co-registration between Landsat 8 and Sentinel 2 NBAR to reduce the impact of misregistration on multi-sensor temporal data analysis. The AROSICS (Scheffler et al., 2017) co-registers the satellite data based on a moving window analysis that estimate sub-pixel shift using the Fourier shift theorem. As AROSICS automatically detects and corrects the misalignments between the satellite datasets, its implementation is suitable for our integrated system. Further details on AROSICS methodology can be found in Scheffler et al. (2017). Finally, I cropped the Landsat 8 NBAR and Sentinel 2 NBAR based on the region that daily gap-free 480 m resolution data covers.

2.4.3 Step 3: Image fusion and gap-filling process

I used image fusion algorithm (i.e., SFSDAF) to enhance the spatial resolution and used spatial gap-filling methods (i.e., NSPI) to fill up the missing pixels. SFSDAF inherits the strengths of FSDAF that are

the minimum requirement for input data and the prediction of abrupt change over heterogeneous land surface (Zhu et al., 2016). Based on FSDAF, SFSDAF were proposed to incorporate sub-pixel class fraction changes into spatiotemporal image fusion (STIF) process. Therefore, SFSDAF products retain the information to derive phenological changes and land cover class changes (Li et al., 2020). I decided to use SFSDAF among the STIF methods to utilize the full potential of multiple satellite dataset in the system. NSPI restores the missing pixels using neighboring pixels in the same-class (Chen et al., 2011b). With this simple assumption, NSPI effectively interpolated the pixel values even in heterogeneous landscape areas. Although I considered GNSPI as an alternative candidate (Zhu et al., 2012), its implementation is more complicated including the high computation cost compared to NSPI. Moreover, the performance of NSPI is comparable with GNSPI in many situations, including heterogeneous landscape. I fused daily gap-free NBAR with 480 m resolution and Landsat 8 NBAR using SFSDAF to produce daily NBAR with 30 m resolution (denoted as STIF 30 m). Then, I make pairs of the STIF 30m data and Landsat 8 mask data at an equivalent or nearest date. I implemented spatial gap-filling algorithm (i.e., NSPI) with the pairs to fill the missing pixels by the cloud-contaminated pixels in Landsat 8 data. Through the spatial gap-filling process, I generated daily gap-free NBAR with 30 m resolution (denoted as GF STIF 30 m). In the same way, I proceeded SFSDAF and NSPI using GF STIF 30 m and Sentinel 2 NBAR to obtain daily gap-free NBAR with 10 m resolution (denoted as GF STIF 10 m).

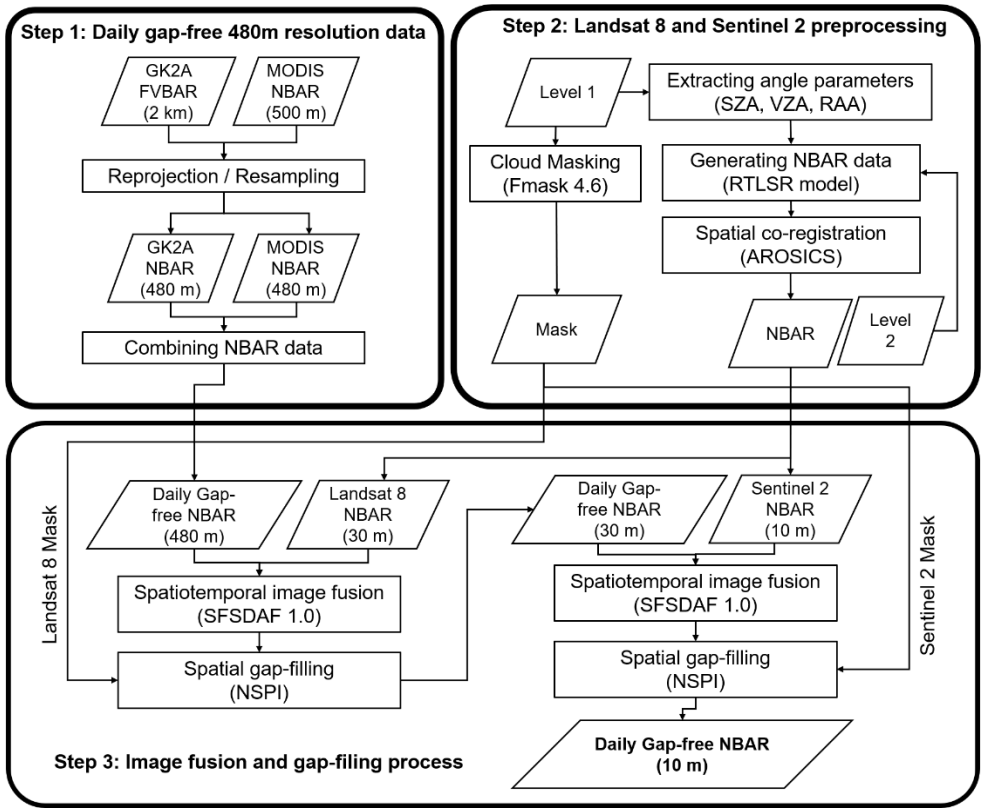

Figure 2.3 The flowchart of the integrated system

2.5 Canopy photosynthesis

I used NIR radiation reflected from vegetation (NIRvP) as a proxy of canopy photosynthesis. From the approximated NIR reflectance from vegetation (NIRv; Eq. [1]) that is the product of the normalized difference vegetation index (NDVI) and NIR reflectance, NIRvP (Eq. [2]) were derived using the amount of incoming photosynthetically active radiation (PAR). Since NIRvP was proposed as a structural proxy for GPP estimation, it had been widely adopted to estimate GPP at hourly to daily timescales for plot to continental scale (Baldocchi et al., 2020; Dechant et al., 2022; Dechant et al., 2020; Jiang et al., 2021; Kong et al., 2022; Liu et al., 2020).

$$\mathbf{NDVI} = \frac{\boldsymbol{\rho NIR - \rho Red}}{\boldsymbol{\rho NIR + \rho Red}} \quad \text{Eq. (1)}$$

$$\mathbf{NIRv} = \boldsymbol{\rho NIR} \times \mathbf{NDVI} \quad \text{Eq. (2)}$$

$$\mathbf{NIRvP} = \mathbf{NIRv} \times \mathbf{PAR} \quad \text{Eq. (3)}$$

where ρNIR and ρRed are reflectance in the NIR and red regions, respectively.

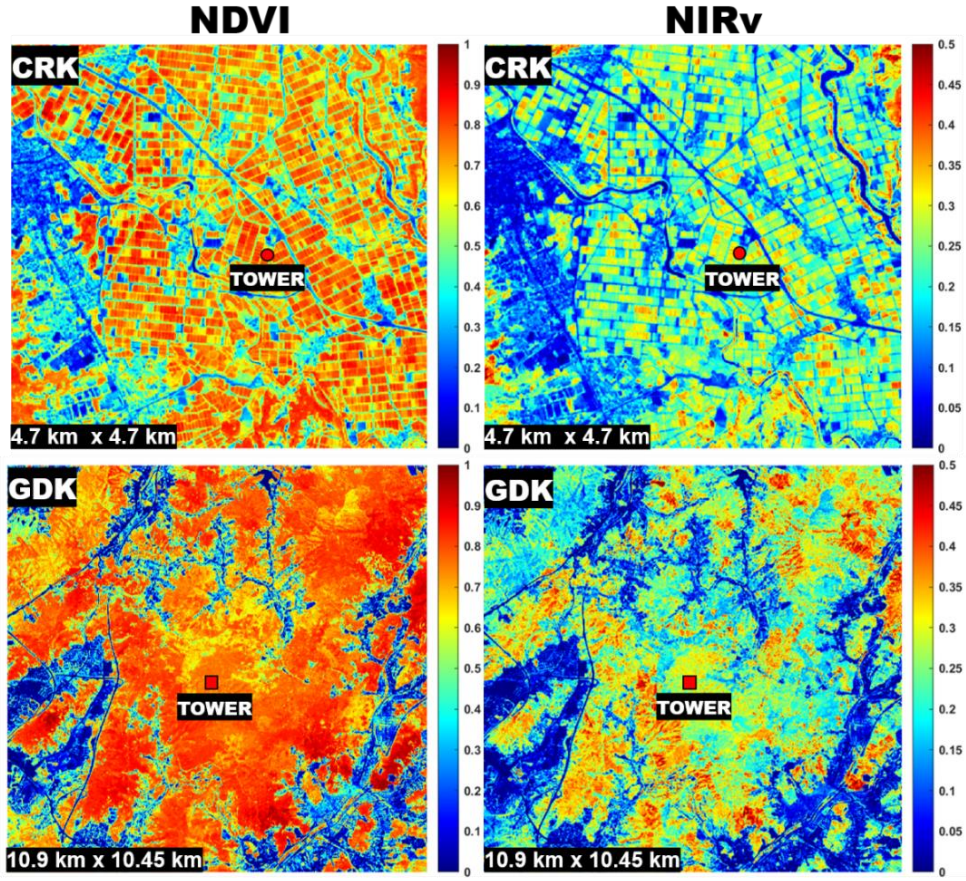

Figure 2.4 Example NDVI and NIRv images produced by the integrated system (i.e., STIF step2 GF) over CRK (red circle) and GDK (red square) sites on July 1, 2020.

2.6 Evaluation

To evaluated the performance of GF STIF data, I compared GF STIF-derived NIRvP to *in situ* measurements used several metrics. I followed previous studies (Chen et al., 2015; Kong et al., 2021; Zhu et al., 2018) that used the coefficient of determination (R^2) of linear regression models, relative bias (rbias; Eq. [4]), and the relative root mean square error (rRMSE; Eq. [5]) to evaluate the image fusion products.

$$\mathbf{rbias} = \frac{\mathbf{E}(\|\mathbf{A}-\mathbf{B}\|)}{\mathbf{E}(\mathbf{B})} \quad \text{Eq. (4)}$$

$$\mathbf{rRMSE}(\mathbf{A}) = \frac{\sqrt{\mathbf{E}((\mathbf{B}-\mathbf{A})^2)}}{\mathbf{E}(\mathbf{B})} \quad \text{Eq. (5)}$$

where A is fusion NIRvP products, B is *in situ* NIRvP, and E is the mean operator.

I compared GF STIF NIRvP to GPP from the eddy covariance systems. As the footprint of EC system is the source area of detected trace gases by an EC system, I used for GF STIF pixel selection for GPP estimation. The daily flux footprints were calculated with the model from Kljun et al. (2015). When extracting GF STIF pixels within the daily footprint of EC system, I weighted the pixel values based on footprint contribution at satellite overpass time for each day (1000hh – 1130hh). I split the weighting factors from 10 % to 80 % in each 10 % interval (Eq. [6]).

$$\mathbf{NIRv(P)_{ECfootprint}} = \sum_{\mathbf{k=1}}^{\mathbf{N}}\left(\frac{\mathbf{NIRv_k\ within\ CL_{10\,\%}}}{\mathbf{N\ within\ CL_{10\,\%}}} \times \frac{\mathbf{10}}{\mathbf{80}}\right) + \sum_{\mathbf{i=1}}^{\mathbf{8}}\sum_{\mathbf{k=1}}^{\mathbf{N}}\left(\frac{\mathbf{NIRv_k\ between\ CL_{(i+1)\times 10\,\%}\ and\ CL_{i\times 10\,\%}}}{\mathbf{N\ between\ CL_{(i+1)\times 10\,\%}\ and\ CL_{i\times 10\,\%}}} \times \frac{\mathbf{10}}{\mathbf{80}}\right) \quad \text{Eq. (6)}$$

where k is each pixel number in the total number(N) of pixels within the footprint area, $CL_{D\,\%}$ is D % footprint contour line.

3. Results and discussion

3.1 Comparison of STIF NDVI and NIRv with in situ NDVI and NIRv

STIF step2 GF NDVI performed better than STIF step1 GF NDVI in terms of tracking changes in *in situ* NDVI (Figure 2.5). STIF step2 GF NDVI showed strong linear relationships with *in situ* NDVI (R^2 = 0.76, rRMSE = 28.19 % at CRK; R^2 = 0.83, rRMSE = 14.68 % at GDK), compared to STIF step1 GF NDVI (R^2 = 0.74, rRMSE = 33.06 % at CRK; R^2=0.75, rRMSE = 17.15 % at GDK). Although all STIF NDVI results were negatively biased against *in situ* NDVI, the underestimations of STIF step2 GF NDVI (rbias = −7.24 % at CRK; rbias = −10.07 % at GDK) were smaller than STIF step2 GF NDVI (rbias = −14.29 % at CRK; rbias = −13.89 % at GDK), especially growing season (Figure 2.5).

STIF step2 GF NIRv did not performed better than STIF step1 GF NIRv in terms of tracking changes in *in situ* NDVI (Figure 2.5). STIF step1 GF NIRv showed strong linear relationships with *in situ* NIRv (R^2 = 0.703 at CRK; R^2 = 0.617 at GDK), compared to STIF step2 GF NIRv (R^2 = 0.701 at CRK; R^2 = 0.462 at GDK). However, STIF step2 GF NIRv showed smaller rRMSE and rbias (rRMSE = 48.71 %, rbias = −7 % at CRK; rRMSE = 36.17 %, rbias = −21.26 % at GDK) than STIF step1 GF NIRv (rRMSE = 60.13 %, rbias = −25.48 % at CRK; rRMSE = 37.65 %, rbias = −29.57 % at GDK).

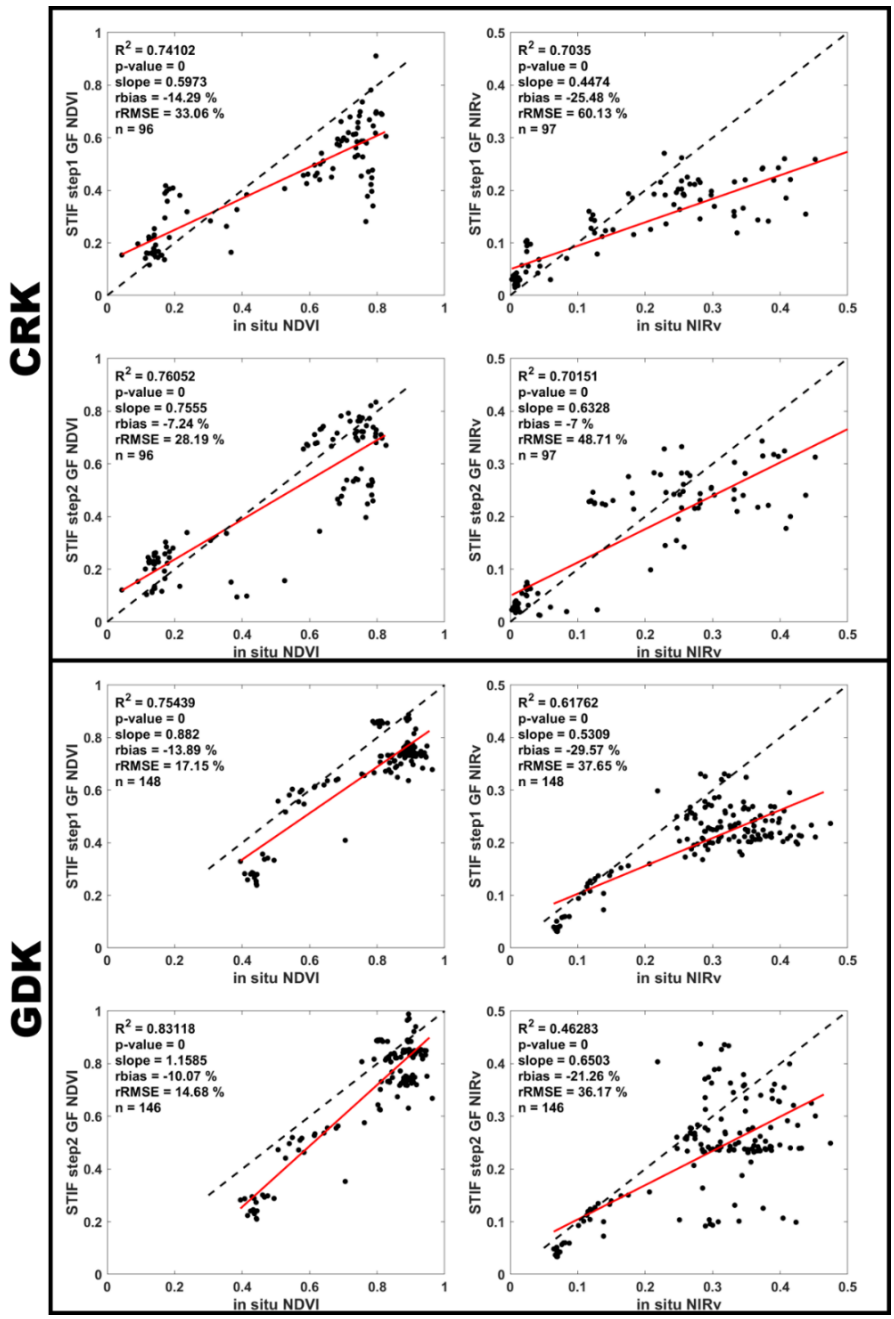

Figure 2.5 Comparison of measured *in situ* normalized vegetation difference index (NDVI) and near-infrared radiation reflected from vegetation (NIRv) around the satellite passing time with STIF step 1 GF and STIF step 2 GF data to calculate the coefficient of determination (R^2), the significance of the linear regression (p-value), the slope of the linear regression (slope), relative root mean square error (rRMSE), and relative bias (rbias). Dashed black lines are 1:1 line (y = x) and n is the number of samples used in the linear regression model.

STIF results followed the seasonal variation of *in situ* NDVI and NIRv (Figure 2.6). STIF step 1 GF NDVI and NIRv over CRK and GDK underestimated the *in situ* NDVI and NIRv during the peak growing season (Figure 2.6).

Since the NDVI and NIRv are used in the calculation of NIRvP (Dechant et al., 2022), the performance of NDVI and NIRv derived from the integrated system (comprising STIF step1 GF and STIF step2 GF) can assured the quality of NIRvP from the integrated system for monitoring canopy photosynthesis. The improvement in estimating in situ NDVI and NIRv were occurred when enhancing spatial resolution. This result is consistent with the previous studies that quantified the impact of land cover mixing within image pixels (Kong et al., 2021).

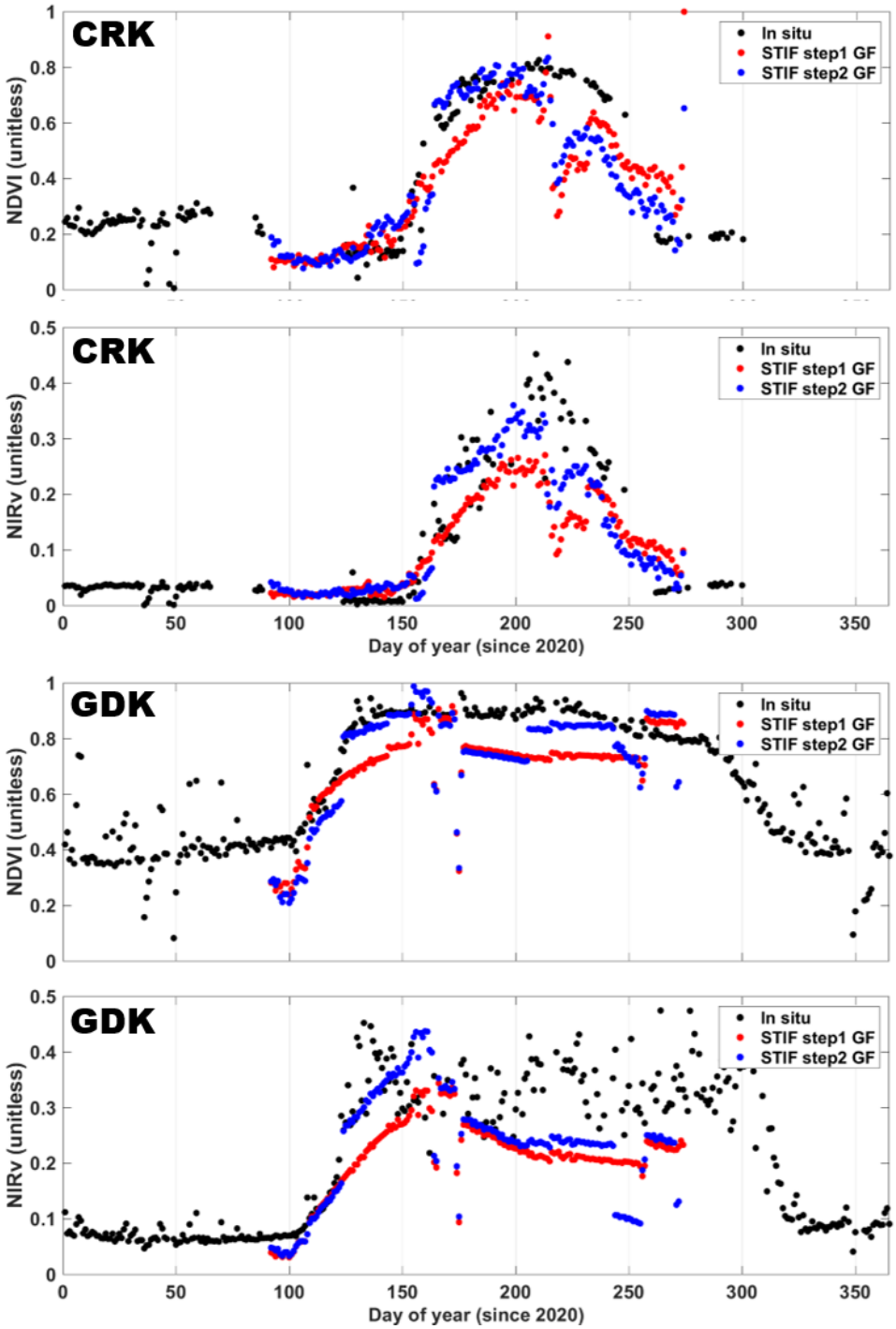

Figure 2.6 Seasonal variations of NDVI and NIRv derived from integrated system (comprising STIF step1 GF and STIF step2 GF) and *in situ* measurements at cropland site (CRK) and deciduous forest site (GDK).

3.2 Comparison of STIF NIRvP with in situ NIRvP

NIRvP derived from the integrated system show good performance to estimate *in situ* NIRvP (Figure 2.7). STIF step1 GF NIRvP showed strong linear relationships with *in situ* NIRvP (R^2 = 0.73, rRMSE = 45.56 % at CRK; R^2 = 0.84, rRMSE = 32.12 % at GDK), compared to STIF step1 GF NIRvP (R^2 = 0.71, rRMSE = 51.90 % at CRK; R^2 = 0.79, rRMSE = 33.48 % at GDK). Compared to STIF step1 NIRvP results, which were negatively biased against *in situ* NIRvP (rbias = −15.98 % at CRK; rbias = −13.89 % at GDK), the underestimations of STIF step2 GF NIRvP (rbias = 5.64 % at CRK; rbias = −13.80 % at GDK) were smaller (Figure 2.7).

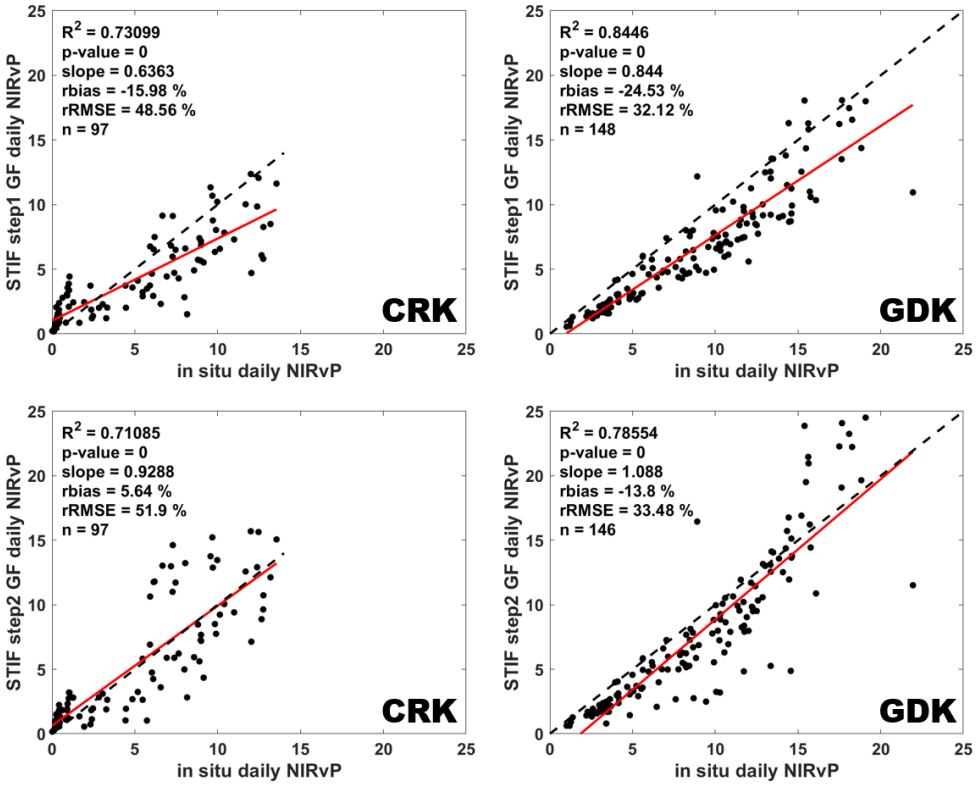

Figure 2.7 Comparison of measured *in situ* near−infrared radiation reflected from vegetation multiplied by incoming sunlight (NIRvP) around the satellite passing time with STIF step 1 GF and STIF step 2 GF data to calculate the coefficient of determination (R^2), the significance of the linear regression (p−value), the slope of the linear regression (slope), relative root mean square error (rRMSE), and relative bias (rbias). Dashed black lines are 1:1 line (y = x) and n is the number of samples used in the linear regression model.

STIF results followed the seasonal variation of *in situ* NIRvP (Figure 2.8). STIF step 1 GF NIRvP over CRK and GDK underestimated the *in situ* NDVI and NIRv during the peak growing season, compared to STIF step 2 GF NIRvP (Figure2. 8).

Integrated system NIRvP showed strong linear relationship with in situ NIRvP, compared to integrated system NDVI (NIRv) with in situ NDVI (NIRv). Compared to STIF step1 GF, STIF step2 GF did not underestimate *in situ* NIRvP during peak growing season. Thus, I can utilize the integrated system NIRvP for estimating high

spatiotemporal resolution canopy photosynthesis map (Baldocchi et al., 2020; Dechant et al., 2022; Kong et al., 2022).

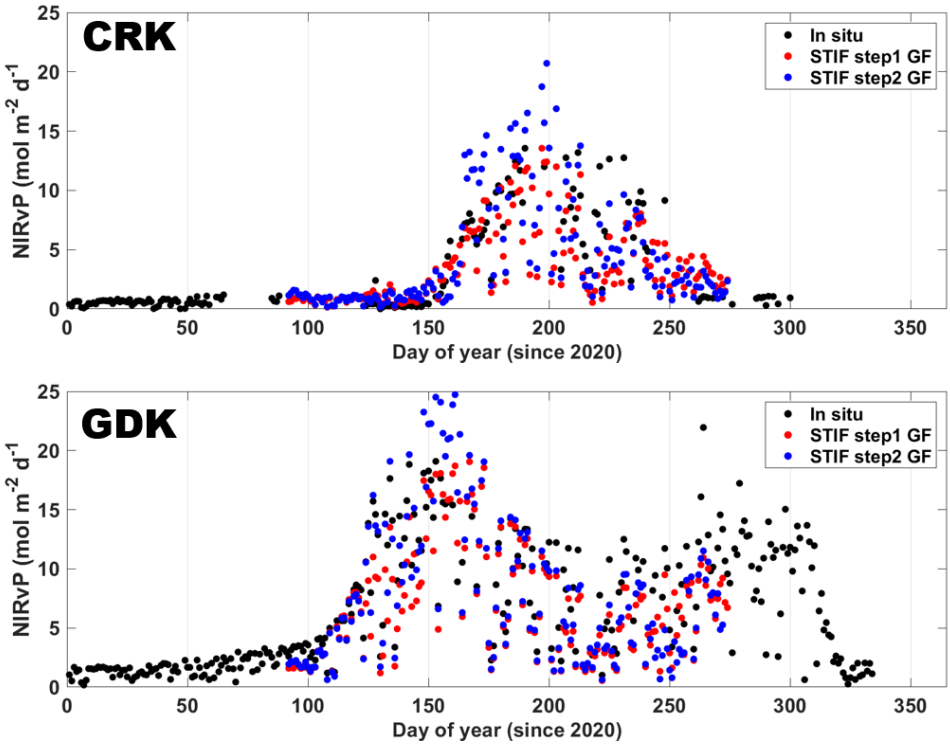

Figure 2.8 Seasonal variations of NIRvP derived from integrated system (comprising STIF step1 GF and STIF step2 GF) and *in situ* measurements at cropland site (CRK) and deciduous forest site (GDK).

4. Conclusion

Enhancement of the spatiotemporal resolution of satellite imagery is important for monitoring daily changes in vegetation, especially heterogeneous landscape areas. In this study, I proposed the integrated system that conduct the series of processes, including cloud masking, nadir BRDF adjustment, spatial registration, spatiotemporal image fusion, spatial and temporal gap-filling. I demonstrated the performance of the integrated system with respect to *in situ* measurements over cropland and deciduous forest in 2020. The proposed system enables us to monitor daily canopy photosynthesis dynamics among regions of interest worldwide with high spatial resolution. I added geostationary satellite images that were not used in the existing image fusion method to lower the uncertainty when increasing time resolution of image fusion products. I anticipate future efforts to use our system in various ecosystems including tropical forest that have been hindered by the limited spatial and temporal resolution of satellite imagery or conifer forest that show small variations of vegetation index throughout a year.

Chapter 3. Super-resolution of historic Landsat imagery using a dual Generative Adversarial Network (GAN) model with CubeSat constellation imagery for monitoring vegetation changes

1. Introduction

Advances in remote sensing have improved the spatial resolution of satellite observations of the Earth's surface. For > 40 years, the Landsat mission has obtained spectral information regarding the Earth's surface with 30–60-m resolution (Irons et al., 2012; Masek et al., 2020; Roy et al., 2014b; Wulder et al., 2019). Since the launch of the Sentinel 2 mission in 2015, multispectral imagery with 10–20 m resolution has become available for global-scale land monitoring (Drusch et al., 2012a). CubeSat constellations (e.g., PlanetScope), which comprise satellites with multiple cubic units (i.e., < 1.33 kg unit^{-1}) (Puig-Suari et al., 2001), have enabled global satellite datasets with 3-m resolution at a near-daily frequency (Roy et al., 2021). For example, vegetation index maps derived from PlanetScope data have demonstrated ability to robustly capture spatial and temporal variations in canopy photosynthesis, crop yield, and phenology (Houborg and McCabe, 2018b; Houborg and McCabe, 2018c; Johansen et al., 2022; Kong et al., 2021; Kong et al., 2022; Ziliani et al., 2022). The recently released Planet Fusion dataset (Planet Fusion Team, 2022), which overcomes cross-sensor inconsistencies in the CubeSat constellation (Houborg and McCabe, 2018a) and cloud-induced data gaps, has shown promise in terms of vegetation monitoring, even in heterogeneous areas (Johansen et al., 2022; Kong et al., 2022; Ziliani et al., 2022).

Despite the emergence of new satellite datasets with high spatial

resolution (< 5 m), longer term historic satellite datasets remain limited by relatively low resolution. Compared to the Planet Fusion 3-m-resolution dataset, datasets with resolutions in the range of tens of meters are often insufficient for effectively detecting vegetation dynamcis in regions characterized by heterogeneous land cover (Kong et al., 2022), and for supporting precision agriculture (Stoy et al., 2022). Multiple approaches have been proposed to enhance the spatial resolution of satellite images, such as image fusion and interpolation-based (e.g., nearest-neighbor or bilinear) methods (Rahmani et al., 2010). Although image fusion methods, including pan-sharpening, were developed for spatial enhancement, they require additional datasets with high spatial resolution for the same time period (Zhu et al., 2018). In contrast, interpolation methods can enhance the spatial resolution of a single image without requiring additional datasets; however, the results are hindered by noise amplification and blurred details. Interpolation methods also magnify the noise of satellite datasets over heterogeneous landscapes because high-spatial-resolution pixels are not always linearly mixed into low-spatial-resolution pixels (Teillet et al., 1997). Therefore, rather than fully exploiting the abundant details in high-spatial-resolution satellite imagery, these datasets are often downscaled to generate long-term datasets with a consistent spatial resolution (Claverie et al., 2018; Griffiths et al., 2019).

Generative adversarial networks (GANs) have shown promise in terms of increasing the spatial resolution of images, through a process known as super-resolution. Super-resolution is an ill-posed inverse problem that may not have an ideal solution for the estimation of perfect observations from imperfect datasets; thus, multiple deep learning-based methods have been suggested to

achieve single-image super-resolution (Dong et al., 2015; Kawulok et al., 2021; Latte and Lejeune, 2020; Ledig et al., 2017; Wang et al., 2021; Wang et al., 2018a). Among deep learning-based methods, GAN-based approaches enable robust restoration of images containing blur, resizing, and noise artifacts (Wang et al., 2021). Because the architecture of GAN-based methods uses both unsupervised and supervised learning (Goodfellow et al., 2014), this architecture can restore spatial representations in past datasets by learning from the detailed spatial representations in new, high-spatial-resolution satellite datasets. The first application of a GAN to enhance image spatial resolution was the Super-Resolution GAN (SRGAN; (Ledig et al., 2017), followed by Enhanced-SRGAN (ESRGAN; (Wang et al., 2018a) and Real-ESRGAN (Wang et al., 2021), all of which improved the ability of GAN-based approaches to manage artifacts. Few studies have used GAN models for object detection in 1–10-m-resolution satellite data (Beaulieu et al., 2018; Ren et al., 2020; Salgueiro Romero et al., 2020; Wang et al., 2020d); to our knowledge, no studies have used GAN models for long-term vegetation monitoring.

Multiple factors have restricted the use of GAN-based super-resolution methods for detailed vegetation monitoring with past satellite datasets. Vegetation monitoring via super-resolution in heterogeneous areas requires high perceptual quality to distinguish vegetated areas from other land cover types, as well as low distortion in terms of spectral information. However, the trade-off between increasing perceptual quality and decreasing distortion limits the performance of GAN models (Blau and Michaeli, 2018). Although spectral information can be preserved by harmonizing image pairs before GAN model training (Salgueiro Romero et al., 2020), the

spatial resolution of Landsat datasets (e.g., Landsat 8 surface reflectance product, 30 m) is 10-fold lower than the spatial resolution of PlanetScope datasets (e.g., Planet Fusion product, 3 m). This large spatial resolution discrepancy complicates accurate co-registration of low- and high-spatial-resolution image pairs (Ren et al., 2020), as well as the restoration of image spatial representation. Differences among satellite sensors (Claverie et al., 2018; Scheffler et al., 2017; Storey et al., 2016; Yan et al., 2016b), caused by variations in sun-target-sensor geometry (Roy et al., 2017; Roy et al., 2016b) and spectral sensitivity, can degrade the performance of the GAN model in super-resolution (Beaulieu et al., 2018) Finally, a robust GAN model requires large amounts of cloud-free low- and high-spatial-resolution image pairs to learn surface changes at different scales; however, it is challenging to pair images for the same date because of clouds (Ju and Roy, 2008) and differences in satellite revisit frequency.

High frequency and high spatial resolution satellite data from CubeSat constellations meet the quality and quantity requirements for image pairs needed to effectively train GAN models. Variations in sun-target-sensor geometry in archived Landsat datasets can be reduced by transforming these datasets to nadir-view bidirectional reflectance distribution function (BRDF)-adjusted reflectance (NBAR) products (Roy et al., 2016b). The Planet Fusion product harmonizes near-daily CubeSat imagery against BRDF-corrected Landsat 8 and Sentinel 2 data (Frantz, 2019b; Planet Fusion Team, 2022), which makes it suitable for the formation of image pairs with Landsat datasets. In addition to the importance of cross-sensor calibration for long-term observation (Wulder et al., 2021), the Planet Fusion product delivers cloud-free surface reflectance values

on a continuous daily basis, which enables straightforward pairing with day-coincident Landsat images. Since the upscaling range allowed by the super-resolution GAN model (i.e., a scale factor of 4) is smaller than the spatial resolution ratio between Landsat and Planet Fusion (i.e., a scale factor of 10), multi-scaled approach is needed (Lai et al., 2017). Because the downscaling process cannot determine values outside of the observation range, downscaled Planet Fusion products inherit the quality of the original Planet Fusion dataset. Accordingly, high-quality image pairs may be constructed between Landsat and Planet Fusion products in multi-scale. When images within a pair have different scales, a sequential GAN model that uses the outputs of a GAN as inputs for another model can be applied (e.g., a boosting meta-algorithm in ensemble machine learning).

In this study, we present an approach for overcoming the spatial resolution gap between long-term (i.e., Landsat archive) and more recent (i.e., Planet Fusion) imagery datasets to generate consistent, high spatial resolution, long-term terrestrial vegetation records. A series of GANs (referred to as "dual GAN") uses the original and downscaled Planet Fusion data to train GAN models; it uses the output of one GAN as input for another model. We designed the dual GAN to reduce spatial differences between past and new datasets in a sequential manner, beginning with the generation of long-term vegetation index maps with high spatial resolution as follows. We prepared Landsat 8 NBAR products to reduce the impacts of directional effects among the different satellite products (i.e., Landsat 8, Sentinel 2, and Planet Fusion). Then, we trained the Remote Sensing Super-resolution dual-GAN (dual RSS-GAN) to emulate Landsat 8 datasets with 10- and 3-m resolution, using a 2

year record of satellite image pairs (i.e., Landsat 8 and Planet Fusion from 2020 and 2021). Next, we used the dual RSS-GAN model to simulate historic Landsat 8 vegetation index maps (2013–2019) with 10- and 3-m spatial resolution over cropland and deciduous forest landscapes. Finally, we compared vegetation index maps from the dual RSS-GAN models with *in situ* tower-based continuous measurements (over a period of up to 8 years) and vegetation index maps acquired using a remotely piloted aerial system (RPAS). These evaluations serve to demonstrate the spatial and temporal robustness of the outlined approach for enhancing the spatial resolution of long-term vegetation observations.

2. Methods

2.1 Real-ESRGAN model

To generate vegetation maps similar to real landscapes, I based the dual RSS-GAN on the Real-ESRGAN model (Wang et al., 2021), which effectively restores detailed spatial representations and suppresses artifacts in low-resolution images. Generally, a GAN consists of two neural networks: the discriminator, which classifies data into real and generator-derived artificial types, and the generator, which creates artificial data that will mislead the discriminator (i.e., leading to labeling as real data). Whereas the generator is updated to reduce differences between model-generated and actual data (i.e., loss), the discriminator is trained to minimize instances of misclassification. Thus, the generator is both unsupervised and constrained by binary supervised classification loss (true vs. artificial data). Successive degradation processes such as image blur, resizing, noise, and compression are repeated twice as high-order degradation during Real-ESRGAN model training with low- and high-spatial-resolution image pairs. In the last step of high-order degradation, the *sinc* filter kernel, which eliminates high frequencies, is utilized to reduce ringing and overshoot artifacts that often appear near sharp transitions, as follows:

$$\mathbf{sinc\ kernel}(\mathbf{i},\mathbf{j}) = \frac{\mathbf{w_c}}{\mathbf{2\pi\sqrt{i^2+j^2}}}\mathbf{J_1}(\mathbf{w_c}\sqrt{\mathbf{i^2+j^2}}) \quad \text{Eq. (1)}$$

where (i, j) are the kernel coordinates; w_c is the cut-off frequency; and J_1 is the first-order Bessel function of the first kind.

To train high-order degradation, the discriminator in Real-ESRGAN was designed to have a U-Net structure with skip connections that capture general context information among pixels

and detailed localization for up-sampling (Ronneberger et al., 2015). Because of the complicated degradation and structure of U-Net, spectral normalization (Miyato et al., 2018) is performed to stabilize the training dynamics of the discriminator. During the training process, a discriminator with L1 loss [Eq. (2)] initializes the generator; Real-ESRGAN is trained using a combination of L1 loss, perceptual loss [Eq. (3), also known as style loss], and GAN loss [Eq. (4)]:

$$\textbf{L1 loss} = \sum |\mathbf{y_{target}} - \mathbf{y_{predicted}}| \quad \text{Eq. (2)}$$

$$\textbf{Perceptual loss} = \frac{1}{\mathbf{W_{i,j}H_{i,j}}} \sum_{\mathbf{x=1}}^{\mathbf{W_{i,j}}} \sum_{\mathbf{y=1}}^{\mathbf{H_{i,j}}} (\boldsymbol{\phi}_{\mathbf{i,j}}(\mathbf{I^{HR}})_{\mathbf{x,y}} - \boldsymbol{\phi}_{\mathbf{i,j}}\left(\mathbf{G_{\theta G}}(\mathbf{I^{LR}})\right)_{\mathbf{x,y}})^{\mathbf{2}}) \quad \text{Eq. (3)}$$

$$\textbf{GAN loss} = \min_{\mathbf{\theta G}} \max_{\mathbf{\theta D}} \mathbf{E}_{\mathbf{I^{HR}} \sim \mathbf{p_{train}}(\mathbf{I^{HR}})}[\mathbf{log D_{\theta D}}(\mathbf{I^{HR}})] + \mathbf{E}_{\mathbf{I^{LR}} \sim \mathbf{p_G}(\mathbf{I^{LR}})}[\mathbf{log}(\mathbf{1} - \mathbf{D_{\theta D}}(\mathbf{G_{\theta G}}(\mathbf{I^{LR}})))] \quad \text{Eq. (4)}$$

where H_j, W_j are the dimensions of the U-Net input feature map; $\phi_{i,j}$ is the feature map for the j^{th} convolution before the i^{th} maxpooling layer; D is the discriminator; G is the generator; θ represents weights and biases; E is the expectation operator; I^{HR} is a high-resolution image; I^{LR} is a low-resolution image; p is the probability distribution; and $D(x)$ is the probability for data x.

In this study, we used the generator and discriminator structure of Real-ESRGAN (Wang et al., 2021) to train the dual RSS-GAN models to generate vegetation index maps at different scales. Because Real-ESRGAN is one of the state-of-art image super-resolution models, the pre-trained generator and discriminator were already trained to capture artifacts introduced by scale

changes; therefore, we adapted the dual RSS-ESRGAN for satellite images. The detailed dual RSS-GAN training process is described in Section 2.7.

2.2 Study sites

We compared 30-, 10-, and 3-m-resolution vegetation index maps with *in situ* measurements at study sites with flux towers where the variation of vegetation indices is large (e.g, cropland and deciduous forest) within the Republic of Korea. Flux towers in rice croplands and deciduous forests are part of the the Korea Flux Network (Figure 3.1; Table 3.1). The deciduous forest site (GDK) is in a mountainous area, where the dominant overstory species are Konara oak (*Quercus* spp.) and hornbeam (*Carpinus* spp.), with a mean canopy height of approximately 18 m, and the dominant understory species are Korean spindletree (*Euonymus oxyphyllus*) and cornel (*Cornus kousa*) (Cho et al., 2021; Ryu et al., 2008; Ryu et al., 2014). The rice paddy site (CRK) has flat terrain, and the predominant species in the flux tower area is rice (*Oryza sativa* L. ssp. *japonica*), with a mean canopy height of around 0.5 m at peak growing season. (Dechant et al., 2020; Dechant et al., 2019; Huang et al., 2018; Hwang et al., 2020; Kim et al., 2019; Yang et al., 2018). Each site has a temperate monsoon climate, with frequent cloud cover and high precipitation from June to August. The vegetations in agricultural land is close to herbaceous with relatively short and simple vegetation structure, compared to deciduous forest that has tall tree with complex vegetation structures. On the other hand, agricultural land is not spatially homogeneous because each field was managed in different dates by the owners when deciduous forest showed stable land cover changes.

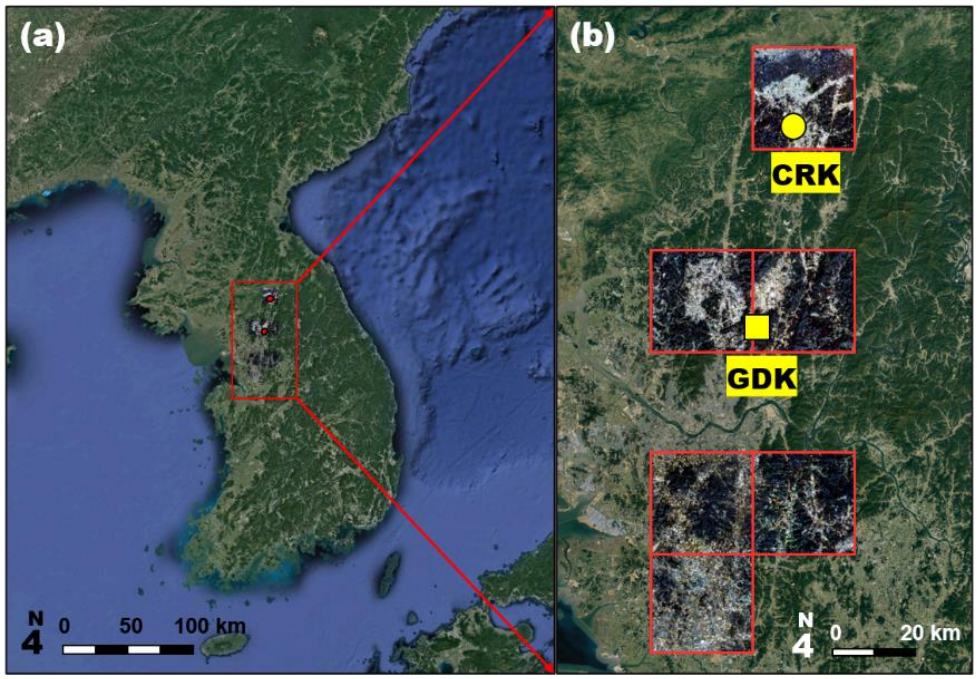

Figure 3.1 (a) Map of the Korean peninsula (image source: Google Earth) indicating the location of the study area. (b) Locations of Planet Fusion tiles (red squares; 24 km × 24 km per tile) and flux towers over cropland (CRK, yellow circle) and deciduous forest (GDK, yellow square). Further details are provided in Table 3.1.

Table 3.1 Description of study sites. Spectroradiometer position indicates sensor height (m). CRO, cropland; DBF, deciduous broadleaf forest. Spectroradiometer position indicates the sensor heights (m) from the ground.

Site (ID)	Land cover Type	Spectro-radiometer position (m)	Canopy height (m)	Latitude (° N) Longitude (° E)	*In situ* measurements period
Gwangreung deciduous forest (GDK)	DBF	22	18	37.7487, 127.1489	2013-2020
Cheorwon rice paddy (CRK)	CRO	5	0.5	38.2013, 127.2507	2016-2021

2.3 *In situ* measurements

To evaluate temporal variation in vegetation index maps with 30-, 10-, and 3-m resolution, we used *in situ* spectral reflectance measured with Jaz hyperspectral radiometers (350-1000nm, 1.5 nm resolution, Ocean Insight, Dunedin, FL, USA) and a light-emitting diode (LED)-based near-surface remote-sensing system (Kim et al., 2019). In the rice paddy, Jaz spectroradiometers with two fiber optic probes and cosine correctors were installed 5 m above the ground (Table 3.1). In the deciduous forest site, the LED-based near-surface remote-sensing system, which automatically collects, transfers and processes vegetation indices using blue, green, red, and NIR LEDs with a quality comparable to the Jaz hyperspectral radiometers (Kim et al., 2019), was installed 4 m above the canopy (Ryu et al., 2014). Because all *in situ* spectral measurements were bi-hemispheric reflectance measurements (Schaepman-Strub et al.,

2006), we estimated 80% cumulative reflectance footprints according to the sensor heights above the canopy (Liu et al., 2017b). The estimated footprint diameters of the *in situ* hyperspectral and LED measurement footprints were approximately 19 m (CRK, rice) and 17 m (GDK, deciduous forest), respectively. To match the tower-based *in situ* collection time to the Landsat 8 satellite overpass time (approximately 1015hh-1030hh), we used *in situ* data at 1030hh. We converted *in situ* hyperspectral data to Landsat [red band: 640-670 nm, near-infrared (NIR) band: 850-880 nm] and Sentinel 2 [red band: 650-680 nm, NIR band: 789-898 nm] broad-band data using the spectral response functions of the Landsat 8 Operational Land Imager (OLI) and Sentinel 2 Multispectral Instrument (MSI), respectively. The LED-based GDK data consist of only 4 bands (peak sensitivity/full-width half maximum): blue (440/65), green (525/80), red (646/56), and NIR (843/72) (Ryu et al., 2014).

To evaluate spatial patterns in the vegetation index maps, we used spectral reflectance maps (5-cm resolution) from a hyperspectral imager (Nano-Hyperspec, visible and NIR model; Headwall Photonics, Fitchburg, MA, USA) mounted on a remotely piloted aerial system (RPAS; DJI-M600pro, DJI, Shenzheng, China). To create the surface reflectance map, we calculated the ratio of outgoing radiance, measured by a hyperspectral imager, to incoming irradiance, measured by a tripod mounted hyper-spectrometer (350 nm-2500 nm, 3nm resolution at 700nm, FieldSpec 4 Wide-ResField Spectroradiometer; ASD, Boulder, CO, USA) at 10-s intervals. The *in situ* surface reflectance data were then exposed to spectral aggregation in accordance with the satellite spectral response functions. In addition, generic BRDF normalization (Roy et al., 2017;

Roy et al., 2016b), co-registration, spatial aggregation, and orthorectification were applied to ensure consistency with Landsat 8 NBAR imagery. Further details concerning the RPAS-derived NBAR processing will be included in a future publication. We used RPAS-derived NBAR maps (5-cm resolution) of rice paddy and deciduous forest sites within ± 1 day of the Landsat 8 overpass dates (i.e., CRK, September 18, 2020) (Figure 3.2).

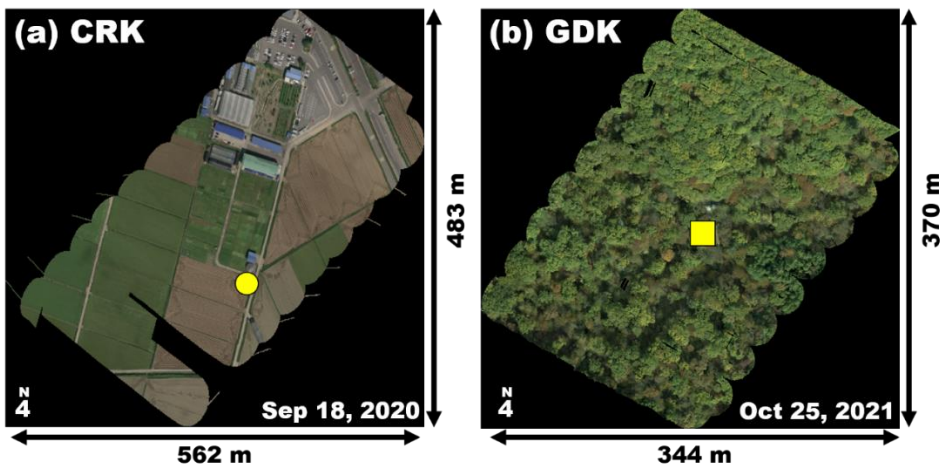

Figure 3.2 *In situ* hyperspectral images (projection, WGS84/UTM zone 52N; red-green-black (RGB) true color; 5-cm resolution). (a) Cropland (CRK) and (b) deciduous forest (GDK). Yellow symbols indicate flux tower locations. Black shading on the CRK map indicates data excluded from the final analysis.

2.4 Vegetation index

Changes in vegetation over time were monitored using the vegetation index map, which included the normalized difference vegetation index (NDVI) (Rouse, 1974; Tucker, 1979) and the NIR vegetation reflectance index (NIRv) (Badgley et al., 2017). NDVI maps, which show the normalized difference between NIR and red light [Eq. (5)], can be used to assess plant health in the target area

because vegetation reflects NIR light while absorbing red light for photosynthesis. The NDVI has frequently been used as a proxy for the chlorophyll content and leaf area index in a target area (Haboudane et al., 2004; Haboudane et al., 2008; Le Maire et al., 2008; Myneni et al., 1995). Moreover, the NDVI can be derived from long-term satellite remote-sensing observational records, including datasets from Landsat multispectral sensors, Moderate Resolution Imaging Spectroradiometer (MODIS), and Advanced Very High-Resolution Radiometer (AVHRR). NIRv is the fraction of vegetation NIR reflected within a mixed pixel, obtained through the multiplication of NIR by NDVI [Eq. (6)] (Badgley et al., 2017). NIRv, which exhibits robust performance in terms of capturing terrestrial photosynthesis from the site-specific scale to the global scale (Badgley et al., 2019), is calculated as the proportion of canopy-intercepted visible light to the vegetation-reflected NIR (Sellers, 1987; Sellers et al., 1992):

$$\mathbf{NDVI} = \frac{\boldsymbol{\rho}\mathbf{NIR}-\boldsymbol{\rho}\mathbf{Red}}{\boldsymbol{\rho}\mathbf{NIR}+\boldsymbol{\rho}\mathbf{Red}} \quad \text{Eq. (5)}$$

$$\mathbf{NIRv} = \mathbf{NDVI} \times \boldsymbol{\rho}\mathbf{NIR} \quad \text{Eq. (6)}$$

where ρNIR and ρRed are reflectance in the NIR and red regions, respectively.

2.5 Satellite data

For dual RSS-GAN training, I used the Landsat 8 OLI dataset (Roy et al., 2014b), including Collection 2 Level 1 (Landsat 8 C2 L1) and Level 2 (Landsat 8 C2 L2) data. I applied the angle parameters from Level 1 products and surface reflectance from Level 2 products to the NBAR derivation method [i.e., the RossThick LiSparse (RTLSR) model (Li and Strahler, 1986; Lucht et al., 2000; Wanner et al.,

1995)], using the parameters of the MODIS BRDF model (Roy et al., 2017; Roy et al., 2016b) (Figure 3). Although the effect of BRDF in NDVI is not significant (Kong et al., 2021), however, a standardized format is required to use multi-source satellite images Landsat 8 NBAR products have 30-m resolution and 16-day temporal resolution (Table 3.2).

To confirm the quality of the Landsat 8 NBAR and Planet Fusion land monitoring products, I also used the Sentinel 2 NBAR product to evaluate the dual RSS-GAN training datasets. I downloaded the Sentinel 2 A/B dataset, including Level 1 (Sentinel 2 L1C) and Level 2 (Sentinel 2 L2A) data from the Sentinel 2 mission (Drusch et al., 2012a), in which Sentinel 2A and 2B carry MSI. Next, I generated Sentinel 2 NBAR products (10-m resolution with 5-day temporal resolution) (Table 3.2) in NBAR processing, which is equivalent to Landsat 8 NBAR processing but uses different BRDF model parameters (Figure 3) (Roy et al., 2017).

I also used an automated cloud and cloud shadow detection method (Fmask 4.6; (Qiu et al., 2019) to flag contaminated pixels in both the Landsat 8 NBAR and Sentinel 2 NBAR datasets (Figure 3.3). I used clear pixels in the Landsat 8 NBAR and Sentinel 2 data to generate NDVI and NIRv vegetation index maps via the red and NIR bands.

Table 3.2 List of satellite-derived datasets used in this study. Satellite data were obtained from Landsat 8 Operational Land Imager (OLI), Sentinel 2 Multispectral Instrument, and PlanetScope Dove measurements. Spatial resolution refers to pixel size in the red and near-infrared (NIR) bands.

Satellite sensor	Data	Spatial resolution	Temporal resolution	Band numbers	Data period
Landsat 8 OLI	Level 1 (top-of-atmosphere), Level 2 (surface reflectance)	30 m	16 days	Red = 4 NIR = 5	2013-2021 (8 years)
Sentinel 2 MSI	Level 1 (top-of-atmosphere), Level 2 (surface reflectance)	10 m	5 days	Red = 4 NIR = 8	2019-2021 (3 years)
PlanetScope Doves	Planet Fusion*	3 m	Near-Daily	Red = 3 NIR = 4	2020-2021 (2 years)

* PlanetScope Ortho Tile Product is the main satellite dataset for Planet Fusion products.

2.6 Planet Fusion

To train the dual RSS-GAN, I used Planet Fusion (Planet Fusion Team, 2022) as a reference dataset. Planet Fusion incorporates reliable-quality datasets from Sentinel-2, Landsat 8, MODIS, and the Visible Infrared Imaging Radiometer Suite (VIIRS) for multi-sensor inter-calibration, harmonization, fusion, and gap-filling of PlanetScope data (Table 2) based on the CubeSat-enabled Spatio-Temporal Enhancement Method (CESTEM) algorithm (Houborg and McCabe, 2018a), which leverages the harmonized Sentinel 2 and Landsat 8/9 bidirectional reflectance distribution function (BRDF)-adjusted 30-m surface reflectance product generated from the Framework for Operational Radiometric Correction for Environmental Monitoring (FORCE) (Frantz, 2019b). Detailed information concerning the harmonization method is provided elsewhere (Houborg and McCabe (2018a). After rigorous detection of clouds and cloud shadows in the PlanetScope data, Planet Fusion fills gaps in the contaminated pixels by fusing Sentinel 2 and Landsat 8 data (Planet Fusion Team, 2022). Thus, the Planet Fusion product contains daily, gap-filled, 3-m-resolution, 4-band surface reflectance (blue: 0.45–0.51 μm; green: 0.53–0.59 μm; red: 0.64–0.67 μm; NIR: 0.85–0.88 μm) with gridded raster tiles (24 km × 24 km) in UTM projection. In this study, six Planet Fusion product tiles from 2020 to 2021 including the CRK and GDK flux tower sites and nearby areas (e.g., urban, mountain, and cropland) were used to generate NDVI and NIRv vegetation index maps (Figure 3.1).

2.7 Dual RSS-GAN via fine-tuned Real-ESRGAN

To generate high-spatial-resolution NDVI and NIRv vegetation index maps derived from Landsat 8 datasets, we trained the dual RSS-GAN using Planet Fusion and Landsat 8 NBAR products from 2020 to 2021 (Figure 3.3). We prepared image pairs for use in training the dual RSS-GAN model by cropping Landsat 8 NBAR products and cloud masks to overlay on Planet Fusion tiles. To exclude pixels in Planet Fusion when corresponding pixels in Landsat 8 NBAR data were contaminated, we superimposed the cropped Landsat 8 cloud masks on Planet Fusion tiles. To reduce computational costs and effectively learn the Planet Fusion tile areas, we sliced the image pair tiles (i.e., Planet Fusion tiles and cropped Landsat 8 NBAR) into sub-tiles using slicing windows with a moving interval of one-half of the window size. The size of the slicing window was sufficient to distinguish land surface features through visual inspection by human eyes. By considering the computation resource for training GAN model, the size of sub-tile of each image pairs was determined as 360 × 360 and 120 × 120. When the ratio of contaminated pixels to all pixels in a sub-tile was > 50%, we excluded the sub-tile from the fine-tuning step. The finalized sub-tiles comprised red, NIR, and NDVI bands (3 channels; false color), which are the bands required for generating the NDVI and NIRv vegetation index maps. To improve data format consistency between the Real-ESRGAN and dual RSS-GAN, sub-tiles in the Geo-TIF format were converted to 16-bit 3-channel Portable Network Graphics (PNG) files. PNG is a lossless compression graphic file format that supports transparency. Because a 16-bit PNG file contains values ranging from 0 to 65535, surface reflectance values (from 0 to 1, with intervals of 0.0001) in Geo-TIF images are

sufficiently converted into pixel values in PNG files. Since Planet Fusion resembles the radiometry of Sentinel 2 products, which is closely resembles Landsat 8 products, we cross-calibrated Planet Fusion sub-tiles against Landsat 8 sub-tiles using band-specific histogram matching (Yang and Lo, 2000), which adjusts the mean and standard deviation of a Gaussian distribution histogram via linear transformation (Wang et al., 2020a), to ensure radiometric consistency between PF and Landsat irrespective of the file conversion (Salgueiro Romero et al., 2020). To avoid rescaling errors, we regarded values > 96% of 16-bit value range (i.e., > 62914) as outliers when reconverting PNG-format model outcomes to Geo-TIF files. Since the spatial resolution ratio (i.e., scale factor) between Landsat and Planet Fusion is 10, we used the multi-scale two-step GAN approach as a mechanism to reduce the scale factor from 10 to 4. The first GAN model in the dual RSS-GAN is designated LP10; it generates Landsat 8 NBAR-like red, NIR, and NDVI data with 10-m resolution using Landsat 8 NBAR 30-m-resolution data. For LP10 training, Planet Fusion products on Landsat 8 overpass dates were resampled on a 10-m interval grid using the nearest-neighbor method, which achieves better performance in spectral-spatial remote-sensing rescaling, compared with bilinear, bicubic, and sinc spatial interpolation methods (Belov and Denisova, 2019). The sub-tiles used for LP10 training were image pairs that consisted of a resampled Planet Fusion (10 m) image with 360 × 360 pixels and a Landsat 8 NBAR (30 m) image with 120 × 120 pixels. Because we set the scale factor of the dual RSS-GAN to 4, Landsat 8 NBAR (30 m) images with 120 × 120 pixels were resampled on a 40-m grid with 90 × 90 pixels using nearest-neighbor interpolation (Figure 4). The 15,033 generated image pairs,

each representing an area of 3.6 km × 3.6 km, were used for LP10 training (batch size = 8; 42 epochs; 40,000 iterations). Because the batch size was set to 8, the LP10 network weights were updated using features from eight images (28.8 km × 28.8 km) in each iteration. We trained the LP10 model on two NVIDIA A100 (80GB) GPU computers for 10 hours.

The final GAN model in the dual RSS-GAN is designated LP3; it generates Landsat 8 NBAR-like red, NIR, and NDVI data with 3-m resolution using Landsat 8 NBAR-like 10-m resolution data from LP10. For LP3 training, we prepared 3-m Planet Fusion tiles on Landsat 8 overpass dates and used 10-m resolution Landsat 8 NBAR-like red, NIR, NDVI data generated by LP10. The sub-tiles used for LP3 training were 3-m Planet Fusion image pairs with 360 × 360 pixels and 10-m Landsat 8 NBAR-like images with 108 × 108 pixels. To obtain a consistent scale factor for the LP10 data, we resampled the 10-m Landsat 8 NBAR-like sub-tiles using a 12-m grid with 90 × 90 pixels using nearest-neighbor interpolation (Figure 4). LP3 was trained using 188,875 image pairs (each representing an area of 1.08 km × 1.08 km) (batch size = 8; 22 epochs; 270,000 iterations). In each iteration, the LP3 network weights were updated using features from eight images (8.64 km × 8.64 km area). We trained the LP3 model on two NVIDIA A100 (80GB) GPU computers for 74 hours.

We applied the dual (i.e., LP10 and LP3) RSS-GAN model to 30-m and 10-m Landsat 8 NBAR-like data from 2013 to 2021, respectively. After comparing calculated NDVI to the model-produce NDVI (R^2>0.98, Figure S1), we used NDVI and NIRv that were calculated directly from the emulated red and NIR channels, rather than the model-produced NDVI channel.

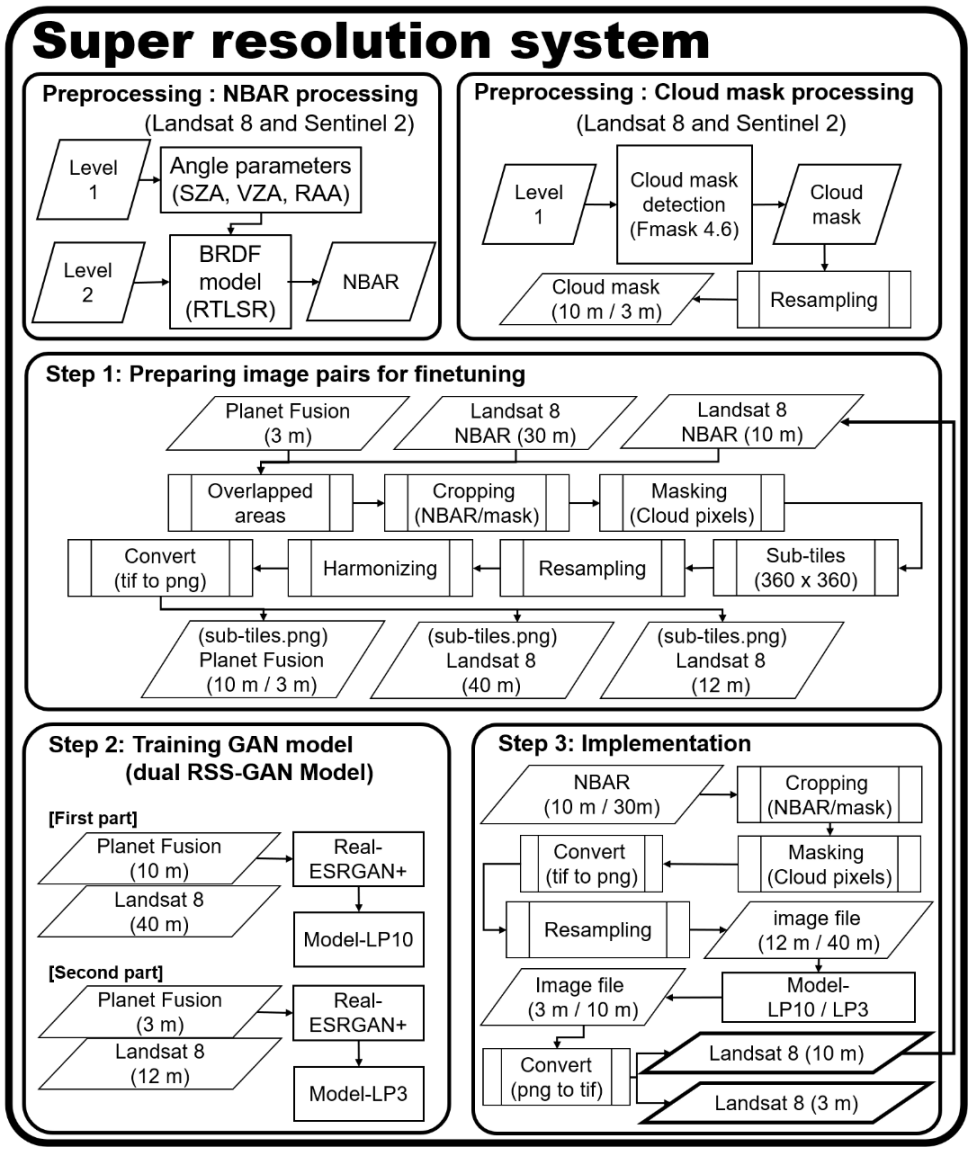

Figure 3.3 Flowchart of the dual Remote Sensing Super-resolution dual-GAN generative adversarial network (dual RSS-GAN) system, which comprises the LP10 and LP3 models.

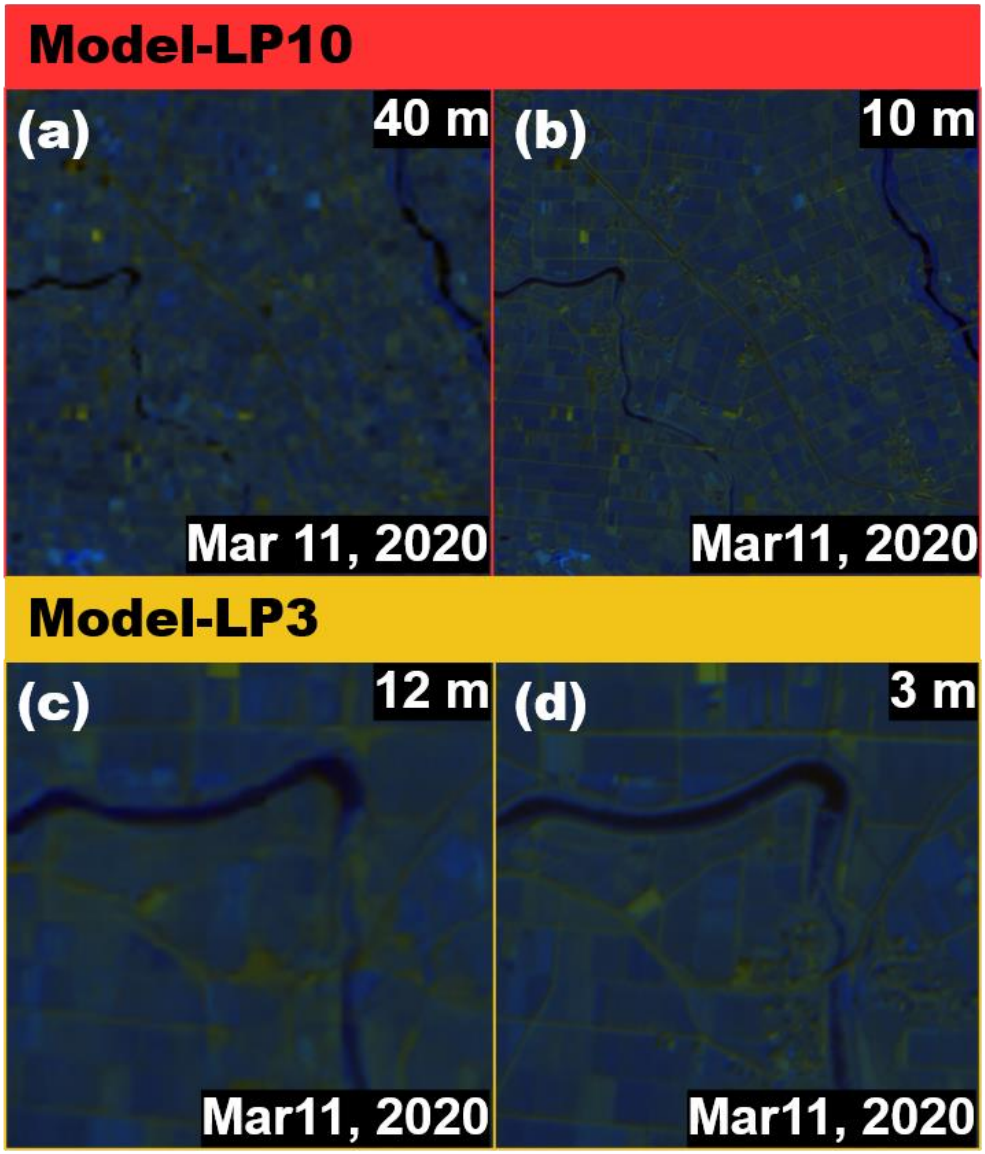

Figure 3.4 Example image pairs (spatial resolution; width × height × channel) including 3−channel false color data [red, NIR, and normalized difference vegetation index (NDVI)] used to train the dual RSS−GAN model, which comprises the LP10 and LP3 models. Image pairs for March 11, 2020, were applied to LP10: (a) resampled Landsat 8 image (40 m; 90 × 90 × 3) and (b) resampled Planet Fusion image (10 m; 360 × 360 × 3) and to LP3: (c) resampled Landsat 8 image (12 m; 90 × 90 × 3) derived from LP10 and (d) Planet Fusion image (3 m; 360 × 360 × 3).

2.8 Evaluation

To evaluate the performance of the dual RSS–GAN over time, I evaluated NDVI and NIRv vegetation maps based on satellite products and the dual RSS–GAN model results by comparison with tower–based *in situ* measurements during the training period (2020–2021) and before the training period (2013–2019). I extracted pixels from the Planet Fusion, Landsat 8 NBAR, and Sentinel 2 satellite products and the dual RSS–GAN model within the estimated footprints of tower–based *in situ* spectral measurements (Section 2.2). I aggregated the extracted pixels in accordance with the cosine law–based upscaling method, which considers the view angle between the sensor and the center of the pixel (Shuai et al., 2011; Shuai et al., 2014) (Figure A1). Typical metrics including the coefficient of determination (R^2) of the linear regression model, root mean square error (RMSE) [Eq. (7)], and relative bias (rbias) [Eq. (8)] were used to evaluate the performances of the satellite products and dual RSS–GAN over time.

$$\mathbf{RMSE} = \sqrt{\mathbf{E((A-B)^2)}} \quad \text{Eq. (7)}$$

$$\mathbf{rbias} = \frac{\mathbf{E(\|B-A\|)}}{\mathbf{E(B)}} \quad \text{Eq. (8)}$$

where A represents the satellite product or model outcomes, B represents *in situ* measurements, and E is the mean operator.

To evaluate the performance of the dual RSS–GAN in emulating detailed spatial representations, I compared NDVI and NIRv vegetation maps from the dual RSS–GAN model with RPAS–based NDVI and NIRv maps. I matched the spatial resolution of the RPAS–based maps (5 cm) to the spatial resolution of the dual RSS–GAN (3 m) using nearest–neighbor interpolation. I evaluated the distortion and perceptual quality of vegetation index maps from the dual RSS–

GAN using image quality assessment methods including the peak signal-to-noise ratio (PSNR), structural similarity index (SSIM) (Zhou et al., 2004), and blind/referenceless image spatial quality evaluator (BRISQUE) (Mittal et al., 2012). Two reference-based image assessment methods, PSNR and SSIM [Eqs. (9) and (10), respectively], were used to quantify information loss in terms of image quality and the degree of structural information distortion, respectively.

$$\mathbf{PSNR} = \mathbf{10}\log_{\mathbf{10}}\left(\mathbf{peakval}^{\mathbf{2}}/\mathbf{MSE}\right) \quad \text{Eq. (9)}$$

$$\left(\because \mathbf{MSE} = \frac{\mathbf{1}}{\mathbf{n}}\sum(\mathbf{A}-\mathbf{B})^{\mathbf{2}}\right)$$

$$\mathbf{SSIM} = \frac{(2\mu_A\mu_B+C_1)(2\sigma_{AB}+C_2)}{(\mu_A^2+\mu_B^2+C_1)(\sigma_A^2+\sigma_B^2+C_2)} \quad \text{Eq. (10)}$$

$$\left(\because \mathbf{C_1} = (\mathbf{k_1 L})^{\mathbf{2}}, \mathbf{C_2} = (\mathbf{k_1 L})^{\mathbf{2}}\right)$$

where A represents the satellite product or model outcomes; B represents *in situ* measurements; E is the mean operator; *peakval* is the peak value of the area; n is the number of observations; μ is the mean; σ is the standard deviation; and constants k_1 and k_2 are set to 0.01 and 0.03, respectively.

Because human vision is the best tool for assessing perceptual quality, we used BRISQUE score (brisque; MATLAB; The MathWorks, Inc., Natick, MA, USA) as a secondary indicator to quantify perceptual quality. A smaller BRISQUE score indicates better perceptual quality. BRISQUE uses support vector regression model that trained on images with distortion such as compression artifacts, blurring, and noise. Prior to human visual inspection, we performed mean subtraction and contrast normalization (MSCN) (Gaussian window size: 10 × 10) (Mittal et al., 2012), which accentuates statistical characteristics hidden in images by eliminating unnecessary repetitive parts of the data and retaining important parts.

Table 3.3 Overview of evaluation protocol of the dual Remote Sensing Super-resolution dual-GAN generative adversarial network (dual RSS-GAN).

Aspect in this study	Quality index	note
Temporal assessment	R^2	Coefficient of determination
	rRMSE	Relative root mean square error
	rbias	Relative bias
Spatial assessment	PSNR	Quantify information loss in terms of image quality
	SSIM	The degree of structural information distortion
	MSCN	Eliminating unnecessary repetitive parts of the data
	BRISQUE	Perceptual quality of image

3. Results

This section reports on 1) the evaluation results of vegetation index maps derived from Planet Fusion, and Sentinel 2 and Landsat 8 NBAR data with respect to tower-based *in situ* data during the dual RSS-GAN training period, and 2) the performance of vegetation index maps produced from the dual RSS-GAN model with respect to tower-based *in situ* data, RPAS-based maps, and maps produced from the original Landsat 8 NBAR data.

3.1 Comparison of NDVI and NIRv maps from Planet Fusion, Sentinel 2 NBAR, and Landsat 8 NBAR data with *in situ* NDVI and NIRv

Planet Fusion NDVI and NIRv showed strong linear relationships with tower-based *in situ* NDVI and NIRv during the training period for the dual RSS-GAN model (2020-2021) (Figure 3.5). The linear relationships based on Planet Fusion NDVI were stronger than the linear relationships based on Landsat 8 NDVI (Planet Fusion on dates with Landsat 8 availability: R^2 = 0.953; RMSE = 0.059; Landsat 8: R^2 = 0.88; RMSE = 0.085) and Sentinel 2 NDVI (Planet Fusion on dates with Sentinel 2 availability: R^2 = 0.966; RMSE = 0.047; Sentinel 2: R^2 = 0.943; RMSE = 0.057) (Figure 3.5). Similarly, Planet Fusion NIRv showed better agreement with tower-based *in situ* NIRv than did Landsat 8 NIRv (Planet Fusion on dates with Landsat availability: R^2 = 0.936, RMSE = 0.037, rbias = −9.2%; Landsat 8: R^2 = 0.908, RMSE = 0.033, rbias= −25.6%) or Sentinel 2 NIRv (Planet Fusion on dates with Sentinel 2 availability: R^2 = 0.787, RMSE = 0.058, rbias = −16.0%; Sentinel 2: R^2 = 0.795, RMSE = 0.049, rbias = −28.5%) (Figure 3.5). When comparing with all available in situ NIRv, Planet Fusion NIRv showed strong linear relationship (Planet Fusion with all available data: R^2 = 0.874, RMSE

= 0.059) (Figure A3.2). Although Landsat 8 and Sentinel 2 NDVI and NIRv tracked the seasonal variations recorded in the *in situ* data, it showed negative bias against *in situ* NDVI or NIRv (Landsat 8 NDVI rbias = −1.1%, Sentinel 2 NDVI rbias = −2.9%, Landsat 8 NIRv rbias = −25.6%, Sentinel 2 NDVI rbias = −28.5%), especially during peak growing season (Figure 3.5).

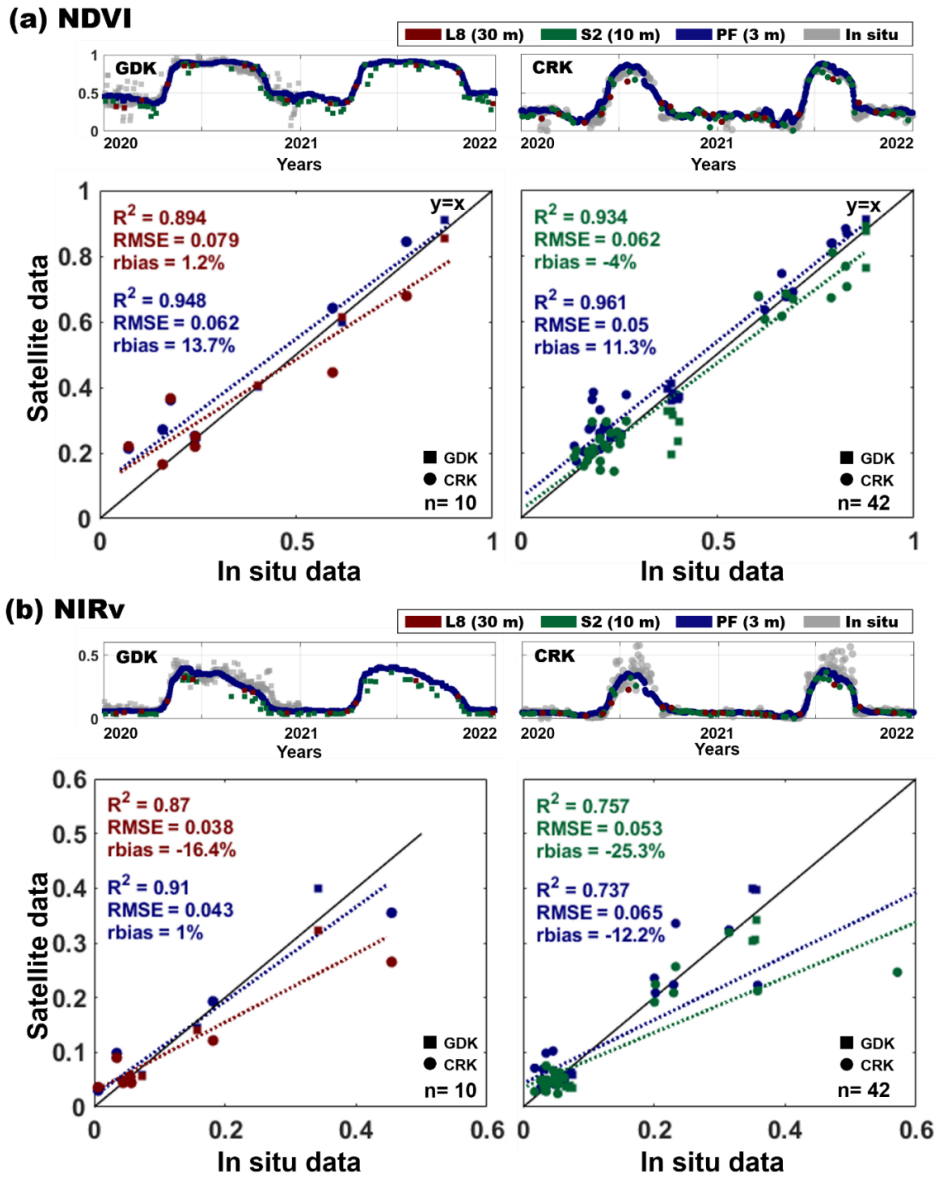

Figure 3.5 Evaluation of Planet Fusion (PF; dark blue), Sentinel 2 (S2; dark green), and Landsat 8 (L8; dark red) (a) NDVI and (b) NIRv values with respect to in situ measurements in deciduous forest (GDK; square) and cropland (CRK; circle). The daily Planet Fusion data were only used on Landsat 8 and Sentinel 2 overpass dates for the calculation of the coefficient of determination (R2), root mean square error (RMSE), and relative bias (rbias). n is the number of samples used in the linear regression model. NDVI and NIRv are unitless. The results of supplemental analyses using all available datasets are shown in Figure A2.

3.2 Comparison of dual RSS-SRGAN model results with Landsat 8 NDVI and NIRv

Compared to Landsat 8 NDVI and NIRv (30-m resolution), LP10 (10 m) and LP3 (3 m) produced NDVI and NIRv data with enhanced spatial detail, as expected (Figures 3.6 and 3.7). For example, the native resolution of Landsat 8 is too coarse (30 m) for distinguishing individual crop fields over a spatially heterogeneous rice paddy area, whereas rice paddy boundaries were more effectively resolved in vegetation maps derived from LP10 and especially LP3 (Figure 3.7). As expected, pixelized streams, roads, and ridges between rice paddies in Landsat 8 imagery are better resolved in the vegetation maps derived from LP10 and LP3 while maintaining consistent histograms (Figures 3.6 and 3.7).

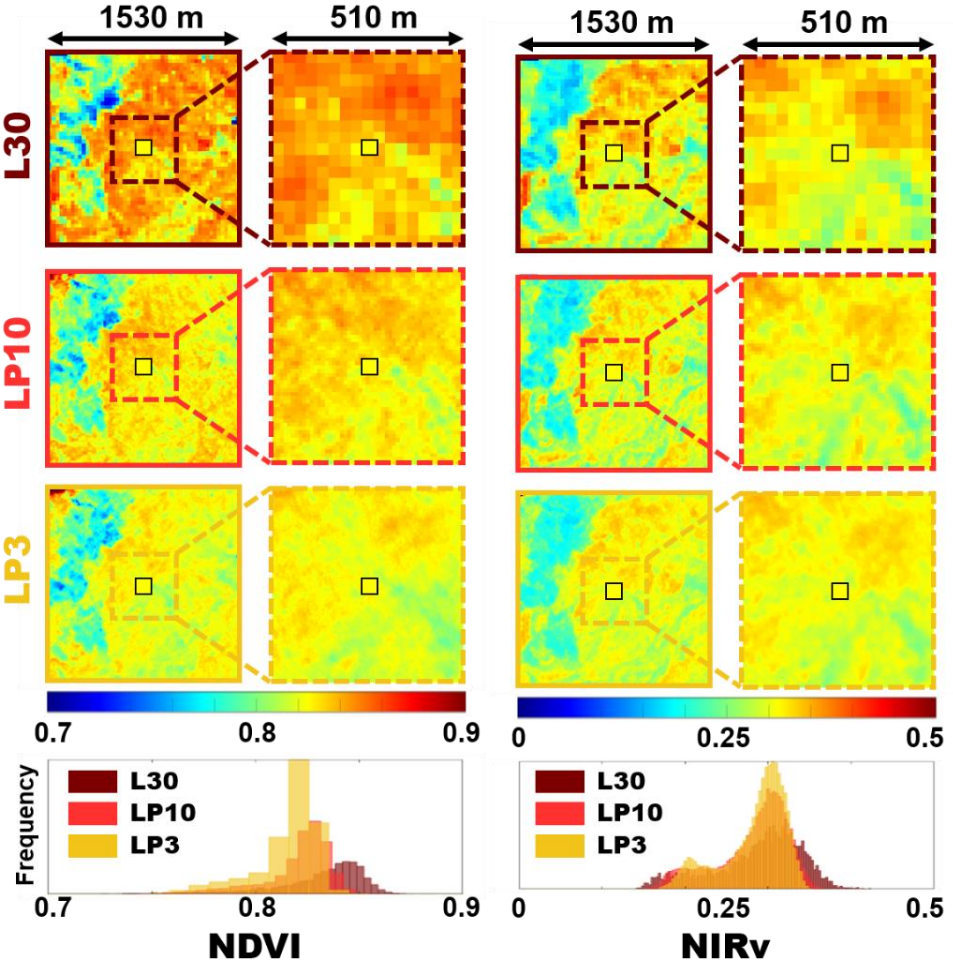

Figure 3.6 Example NDVI and NIRv images produced by the dual RSS−GAN models (LP10 and LP3) and Landsat 8 (L30) at the GDK site (yellow square) on May 9, 2018. Overall landscape (1530 m × 1530 m) and flux tower area subsetted (510 m × 510 m) images are shown. The bottom panel shows the corresponding NDVI and NIRv histograms for L30, LP10, and LP3. NDVI and NIRv are unitless. The same figure in gray scale is shown in Figure S3.2.

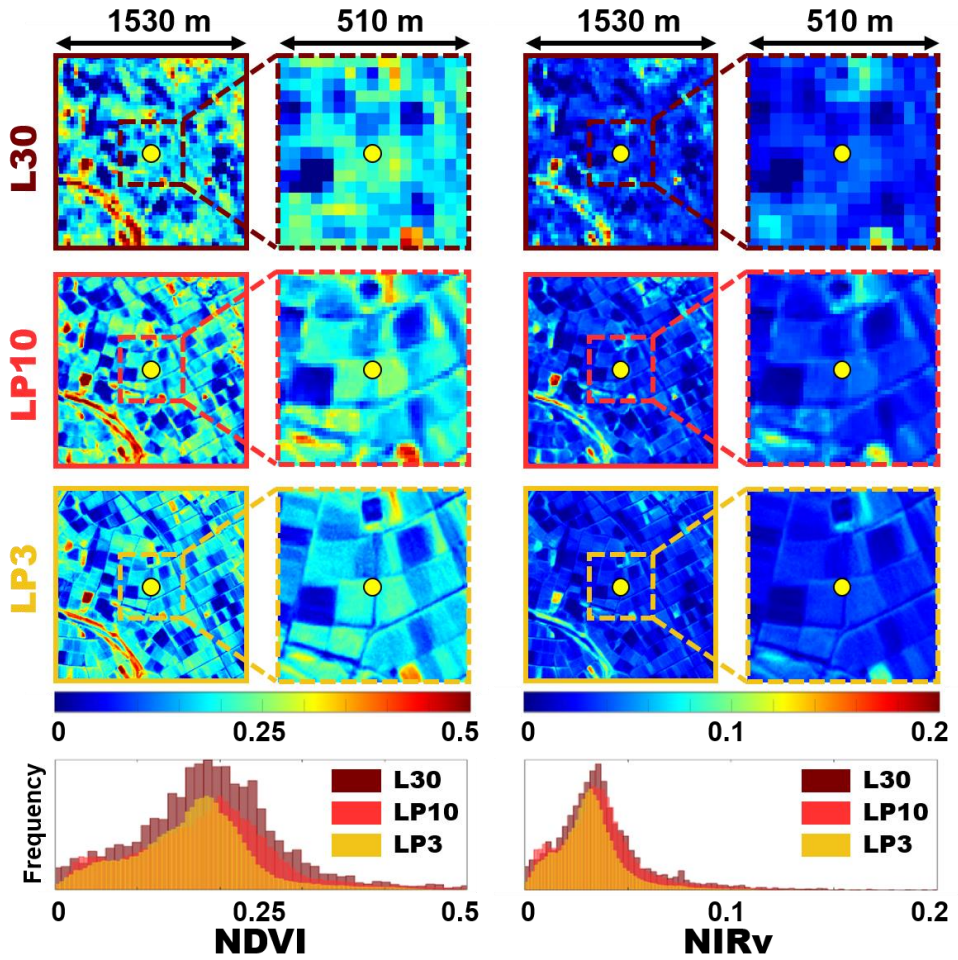

Figure 3.7 Example NDVI and NIRv images produced by the dual RSS-GAN model (LP10 and LP3) and Landsat 8 (L30) images over the CRK site (yellow circle) on May 9, 2018. Overall landscape (1530 m × 1530 m) and flux tower area subsetted (510 m × 510 m) images are shown. The bottom panel shows the corresponding NDVI and NIRv histograms for L30, LP10, and LP3. NDVI and NIRv are unitless. The same figure in gray scale is shown in Figure S3.2.

3.3 Comparison of dual RSS-GAN model results with respect to *in situ* time-series NDVI and NIRv

The dual RSS-GAN model followed the seasonal variation of *in situ* NDVI and NIRv, compared with Landsat 8 (Figure 3.8). However, compared with the dual RSS-GAN model, the Landsat 8 NBAR-derived NDVI and NIRv underestimated the *in situ* NDVI and NIRv during the peak growing season (Figure 3.9).

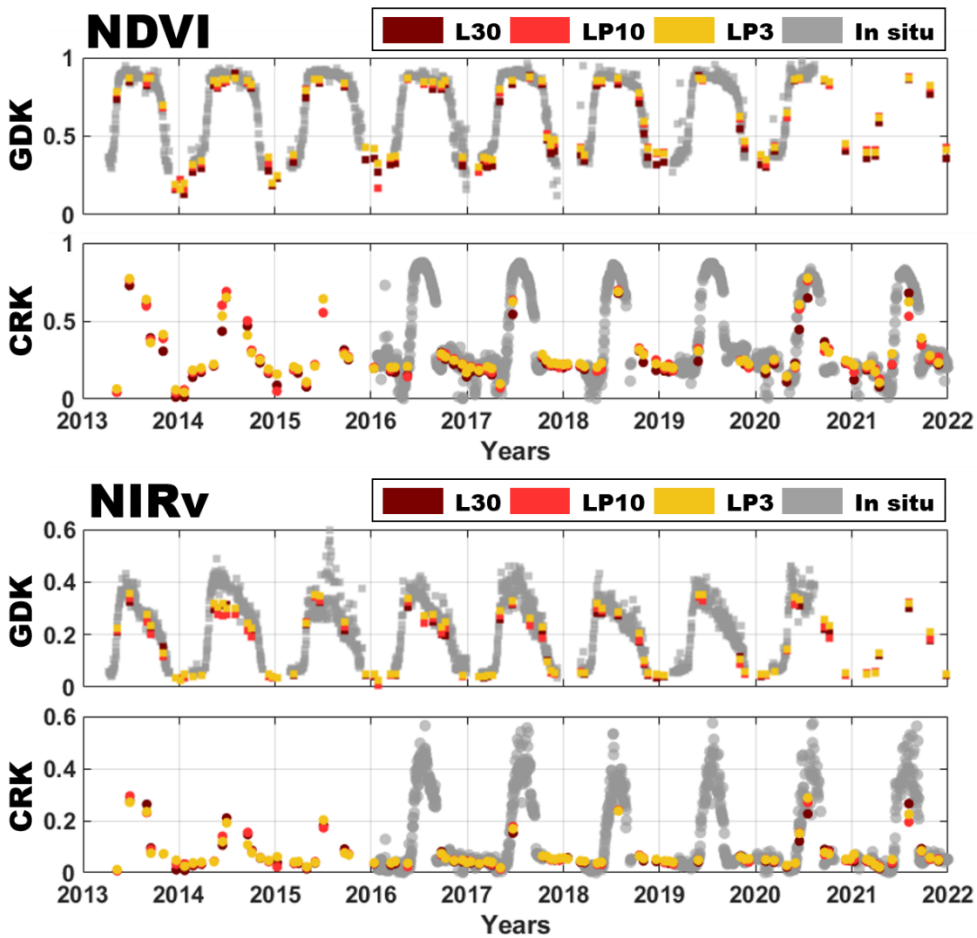

Figure 3.8 Seasonal variations of NDVI and NIRv derived from satellite bidirectional reflectance distribution function (BRDF)-adjusted reflectance (NBAR) (Landsat 8, L30), the dual RSS-GAN model (comprising the LP10 and LP3 models), and *in situ* measurements at each site. GDK, deciduous forest (squares); CRK, cropland (circles). NDVI and NIRv are unitless.

Statistically, the LP10 and LP3 models performed better than Landsat 8 in terms of tracking changes in the in situ NDVI and NIRv from 2013 to 2019 (Figures 3.9 and 3.10). The linear relationships between the in situ NDVI from all sites and model or satellite-based NDVI were ranked as follows, in order of decreasing R2: LP10 > LP3 > Landsat 8 NBAR, with R2 (RMSE) values of 0.955 (0.057), 0.950 (0.060), and 0.946 (0.064), respectively. Similarly, for NIRv the linear relationships were ranked as follows, in order of decreasing R2: Landsat 8 NBAR > LP3 > LP10, with R2 (RMSE) values) of 0.916 (0.032), 0.915 (0.035), and 0.903 (0.035), respectively. Landsat 8 NDVI and NIRv data were more negatively biased with respect to the *in situ* data from all sites (NDVI rbias = −4.9%, NIRv rbias = −16.3%) compared to LP10 (NDVI rbias = −0.7%, NIRv rbias = −15.8%) and LP3 (NDVI rbias = 0.6%, NIRv rbias = −10.0%). Similarly, at each site, Landsat 8 NBAR vegetation indices (i.e., NDVI and NIRv) were also negatively biased against in situ data (NDVI rbias = −3.7%, NIRv rbias = −16.1% at deciduous forest site; NDVI rbias = −12.4%, NIRv rbias = −17.5% at cropland site) compared with LP10 (NDVI rbias = −0.1%, NIRv rbias = −16.2% at deciduous forest site; NDVI rbias = −4.7%, NIRv rbias = −12.7% at cropland site) and LP3 (NDVI rbias = 1.2%, NIRv rbias = −9.7% at deciduous forest site; NDVI rbias = −3.2%, NIRv rbias = −11.5% at cropland site) (Figure 3.9). The dual RSS-GAN based NDVI outperformed Landsat 8 NDVI for estimating in situ NDVI (Figure 3.10). A similar tendency was reported for NIRv with the dual RSS-GAN demonstrating comparable or stronger linear relationships less biased with respect to in situ NIRv relative to the Landsat 8 based retrievals (Figure 3.10). In general, the LP10 and LP3 models were characterized by reduced biases with respect to the in situ NDVI and NIRv data relative to Landsat 8 at CRK.

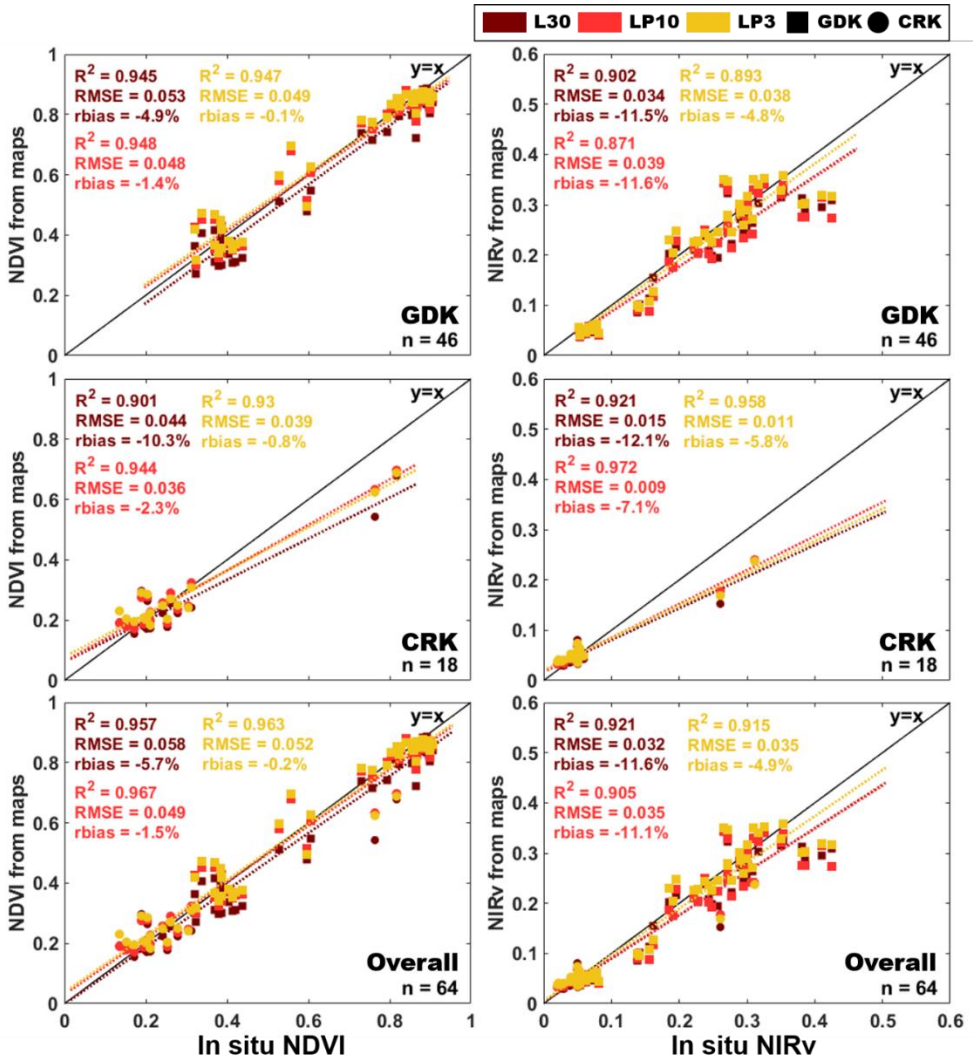

Figure 3.9 Comparison of NDVI and NIRv derived from Landsat 8 NBAR (L30), the dual RSS-GAN model (LP10 and LP3) with in situ measurements for the GDK (squares) and CRK (circles) sites. R2, coefficient of determination; RMSE, root mean square error; rbias, relative bias. NDVI and NIRv are unitless. Detailed site data are provided in Table A3.3.

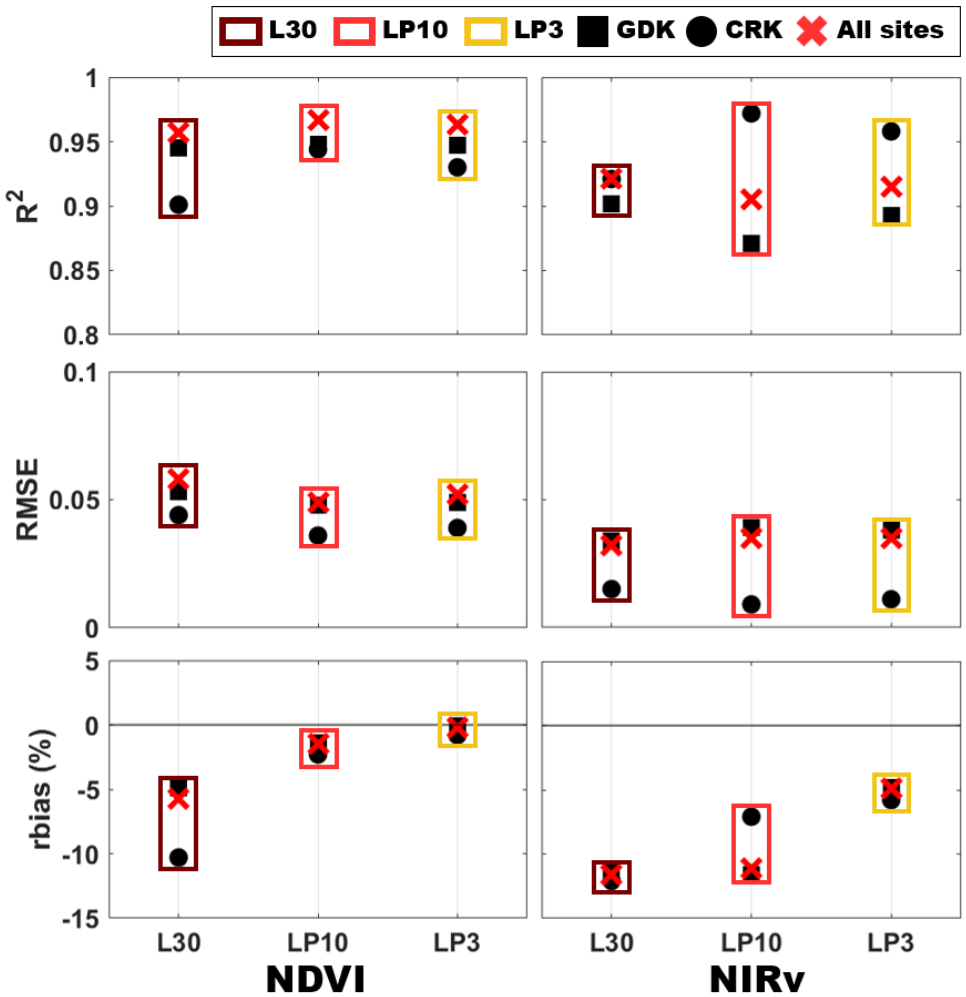

Figure 3.10 Statistical comparisons of Landsat 8 (L30) and dual RSS-GAN model (LP10 and LP3) based NDVI and NIRv against in situ measurements at the CRK (circles) and GDK (squares) sites. R2, coefficient of determination; RMSE, root mean square error; rbias, relative bias. Detailed site data are provided in Table A3.2.

3.4 Comparison of the dual RSS-GAN model with NDVI and NIRv maps derived from RPAS

The dual RSS-GAN model (LP10 and LP3) results captured more of the spatial variations in NDVI and NIRv evident from high resolution (5 cm) RPAS-based resulting in improved field delineation (Figure 3.11). The rice paddy edges are better resolved in the dual RSS-

GAN model results compared to the Landsat nearest-neighbor and bilinear interpolation results (Figure 3.11). The nearest-neighbor and bilinear interpolation results overemphasized noise and blurring of details compared with the dual RSS-GAN model results (Figure 3.11). At the cropland (CRK) and deciduous forest (GDK) sites, the comparative analysis results for NDVI and NIRv maps with respect to the RPAS-based map showed that the 3 m resampled (i.e., bilinear, nearest-neighbor) Landsat 8 data scored high values in distortion assessment index (i.e., PSNR and SSIM). At the same time, the dual RSS-GAN model results scored better than 3 m resampled Landsat 8 data in perceptual quality index (i.e., BRISQUE) (Table 3.4).

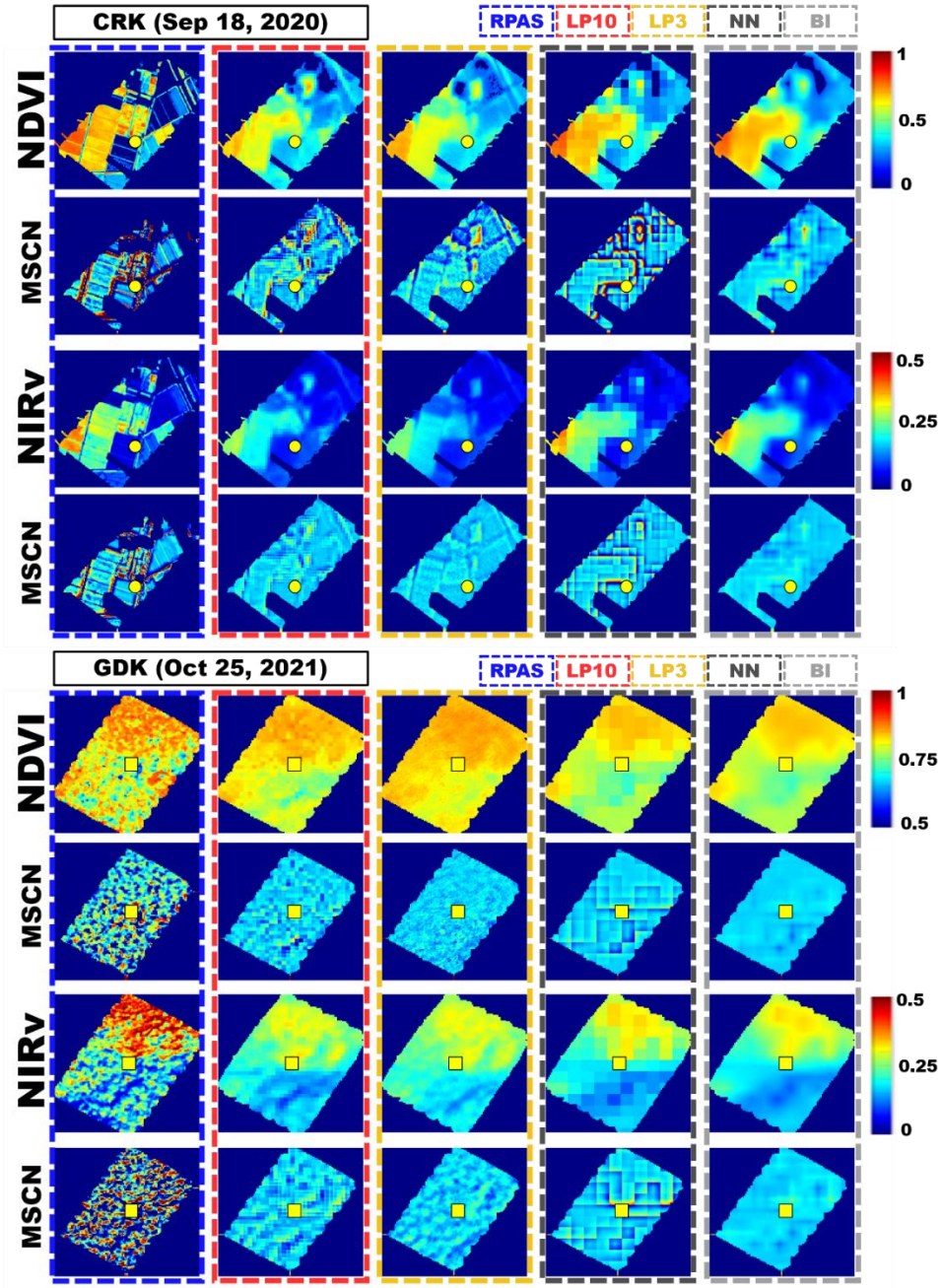

Figure 3.11 NDVI and NIRv maps derived from the remotely piloted aerial system (RPAS), the dual RSS-GAN model (LP10 and LP3), and nearest-neighbor or bilinear interpolation at the cropland (yellow circles) site on September 18, 2020, and the deciduous forest (yellow squares) site on October 25, 2021. Redundant information in the NDVI and NIRv maps was eliminated through mean subtraction and contrast normalization (MSCN) (color map: jet, range: −0.05 to 0.1). NDVI and NIRv are unitless.

Table 3.4 Evaluation of image quality in NDVI and NIRv vegetation index maps derived from the dual RSS-GAN model (LP10 and LP3) or via resampling (i.e., nearest-neighbor or bilinear interpolation) relative to the RPAS-based maps at the cropland (CRK, September 18, 2020) the deciduous forest (GDK, October 25, 2021) sites. BRISQUE, blind/referenceless image spatial quality evaluator; PSNR, peak signal-to-noise ratio; SSIM, structural similarity index. Highest values are indicated in bold font for SSIM and PSNR. Lowest values are indicated in bold font for BRISQUE.

Site	Vegetation index	Quality Assessment	LP10	LP3	NN	BI
CRK	NDVI	PSNR	16.27	16.05	16.83	**16.90**
		SSIM	0.6252	0.6275	0.6322	**0.6441**
		BRISQUE	39.9110	**45.7055**	54.7800	51.0786
	NIRv	PSNR	20.45	20.19	**23.22**	23.17
		SSIM	0.7123	0.7146	0.7557	**0.7590**
		BRISQUE	45.0739	**44.0738**	46.8685	45.8685
GDK	NDVI	PSNR	26.36	26.36	26.58	**26.76**
		SSIM	0.7223	0.7282	0.7267	**0.7328**
		BRISQUE	**36.2711**	36.5865	50.3063	49.7062
	NIRv	PSNR	18.49	18.52	**19.00**	**19.00**
		SSIM	0.4557	0.4639	**0.4744**	0.4701
		BRISQUE	**48.9077**	50.0886	55.8437	51.2454

4. Discussion

4.1 Monitoring changes in terrestrial vegetation using the dual RSS-GAN model

The dual RSS-GAN model demonstrated the strengths of GAN-based image restoration methods in vegetation monitoring. Despite the coarse resolution (30 m) of the input dataset, the dual RSS-GAN model was able to simulate high-resolution vegetation maps with significantly improved delineation of individual crop fields (Figure 3.7). Compared with the nearest-neighbor and bilinear methods (Belov and Denisova, 2019), the dual RSS-GAN model exhibited less noise and reduced blurring of details over heterogeneous landscapes (Figure 3.11). This perceptual quality of the dual RSS-GAN model was confirmed by visual inspection. It follows that the dual RSS-GAN was able to emulate Landsat 8-like maps with 10- and 3-m resolutions without significant degradation in terms of spectral representations (Figures 3.6 and 3.7).

The dual RSS-GAN model reduced the uncertainty associated with Landsat 8 images when capturing the seasonal variation of vegetation indices. While the Landsat 8 NDVI and NIRv maps captured the overall seasonal variations of the *in situ* data (Figure 3.8), *in situ* NDVI and NIRv were being underestimated during the growing seasons (Figures 3.5 and 3.8). Because the dual RSS-GAN model used Landsat 8 as an input dataset, it inherited the Landsat 8 based underestimation of vegetation index values relative to the in-situ data (Figure 3.8) albeit significantly reduced (Figures 3.9 and 3.10). The improved accuracy of the vegetation index data generated by the dual RSS-GAN during the growing season may be attributed to the enhanced spatial resolution, which allowed pixels within the footprint

of the *in situ* data (approximately 15–17 m in diameter) to be better resolved (Kong et al., 2022). The dual RSS–GAN was trained using Planet Fusion data, which did not underestimate vegetation indices with respect to *in situ* data during the growing season (Figure 3.5); thus, Planet Fusion data also played a role in reducing vegetation index underestimation in super resolved Landsat 8 data. Unbiased vegetation index estimates during the peak growing season are critically important for greening/browning trend analyses (Hwang et al., 2022) and for accurately detecting land cover changes (Pielke Sr, 2005; Turner et al., 2007).

The dual RSS–GAN model enhanced the perceptual quality of Landsat 8 without the additional distortion. Compared to the dual RSS–GAN model, the interpolation methods exhibited lower distortion with respect to RPAS–based maps (Table 4). However, the interpolation methods produced oversmoothed maps and pixelization patterns (Figure 3.11). Because super–resolution relies on a trade–off between perceptual and distortion quality (Blau and Michaeli, 2018), improvements to the spatial details tend to come at the expense of increased distortion. However, compared to the performance of the dual RSS–GAN model in spatial enhancement, the expense of distortion was not significant (Table 3.4). Coincidentally, distortion is related to the signal bit rate, or the amount of information per unit of time, based on the rate–distortion theory (Cover, 1999; Shannon, 1959). As a consequence of the triple trade–off among perception, distortion, and rate (Blau and Michaeli, 2019), the dual RSS–GAN file conversion process, which converts red, NIR, and NDVI values (range: 0 to 1, interval of 0.0001, which fit in 14–bit values) to 16–bit values (Section 2.7), may serve to reduce additional distortion.

The structure of the dual RSS-GAN facilitated 10-fold spatial enhancement to Landsat 8 data. The large spatial resolution ratio (10) between Landsat 8 (30 m) and Planet Fusion (3 m) makes it difficult to super-resolve fine spatial details. Since super-resolution in one step (i.e., from 30 m to 3 m) does not satisfy the recommended upscaling factor in super-resolution (over 4), an incremental multi-resolution approach for learning the detailed spatial image representations have been suggested (Denton et al., 2015; Karnewar and Wang, 2020; Lai et al., 2017) based on scale-space theory that is basis of a tool for analyzing structures at different scales (Lindeberg, 1994). In the ensemble meta-algorithm in machine learning, boosting is the sequential learning process that weights the next algorithm to correct the prediction of the previous algorithm. Because the dual RSS-GAN was designed to take advantage of multi-scale learning and boosting, it can be considered as a multi-resolution sequential GAN towards enhancing the spatial resolution of Landsat data. Thus, the dual RSS-GAN restored the spatial representation in Landsat data into both 10 m and 3 m resolution (Figure 3.6 and 3.7) although some smoothed results appeared (Figure 3.11).

4.2 CubeSat data in the dual RSS-GAN model

In this study, we confirmed that the Planet Fusion surface reflectance product enabled by CubeSat constellation imagery is suitable for training the dual RSS-GAN model to enhance the spatial resolution of Landsat 8 vegetation indices for detailed (i.e., 3 - 10 m) vegetation monitoring. The 3 m resolution Planet Fusion data helped to effectively train the dual RSS-GAN to super-resolve Landsat 8 based vegetation index maps (Figure 3.6 and 3.7). Because

the downscaling process preserves the original image quality, unlike the upscaling process (Bierkens et al., 2000), the Planet Fusion 3 m product could be used for both LP10 and LP3 training purposes. Indeed, the dual RSS-GAN model exhibited robust performance in terms of generating both 10- and 3-m resolution products (Figures 3.6, 3.7, 3.10, and 3.11). Seasonal changes in vegetation indices derived from Planet Fusion data also impacted the changes in vegetation indices produced by the dual RSS-GAN model since the dual RSS-GAN model was trained with respect to Planet Fusion products (Figure 3.4), so vegetation maps from the dual RSS-GAN model tracked *in situ* data with unbiased vegetation index estimates (Figures 3.9 and 3.10). The Planet Fusion harmonization process ensures radiometric consistency with Landsat 8 over time. Although the band-specific histogram-matching method preserves image pairs in the dual RSS-GAN, the Planet Fusion harmonization solves cross-sensor inconsistency issues in multi-generation CubeSat constellation data over time (Houborg and McCabe, 2018a; Planet Fusion Team, 2022). Thus, Planet Fusion-derived vegetation indices were similar to Landsat 8-derived vegetation indices, without outliers (Figure 3.5) (Houborg and McCabe, 2018a; Planet Fusion Team, 2022); the high level of interoperability eliminated the need for additional calibration of the dual RSS-GAN model over time. Finally, the Planet Fusion product, being a daily product leveraging the global near-daily coverage of the PlanetScope constellation (Roy et al., 2021), produced sufficient image pairs with Landsat 8 to train the dual RSS-GAN model.

4.3 Perspectives and limitations

The dual RSS-GAN model could be used to generate high

resolution (~3 m) canopy photosynthesis maps over the historical Landsat archive. Numerous studies have demonstrated methods for harmonizing multi-satellite data, including Landsat 5, Landsat 7, Landsat 8, and Sentinel 2 products (Cao et al., 2022; Claverie et al., 2018; Frantz, 2019b; Helder et al., 2018; Roy et al., 2016a). Thus, the outlined approach could be applied to harmonized Landsat archive data for detailed monitoring of decades-long variations in vegetation over spatially heterogeneous areas, including gross primary productivity (GPP) (Baldocchi et al., 2020; Dechant et al., 2022; Kong et al., 2022), which can be estimated from multiplying NIRv and photosynthetically active radiation (e.g., (Ryu et al., 2018)). Finally, the outlined approach could be added as a module after image fusion methods (Moreno-Martínez et al., 2020; Zhu et al., 2018) that can use Landsat archived dataset to generate long-term daily GPP maps with high spatial resolution. The matching of such maps to the footprint of *in situ* GPP measurements (Kong et al., 2022) would facilitate the validation of remote-sensing-based GPP products over spatially heterogeneous landscapes from past to present. For example, gap-free satellite images around *in situ* GPP measurement area (Walther et al., 2022) with the outlined approach can avoid the biased GPP result that from coarse spatial resolution (Chen et al., 2011a; Ran et al., 2016). Moreover, mapping of GPP at 3 m resolution for multiple fields over a heterogeneous landscape would be useful for precision agriculture applications (Duveiller and Defourny, 2010; Gebbers and Adamchuk, 2010; Sishodia et al., 2020).

Gap-filling is required to fill missing values in the dual RSS-GAN model and reconstruct a long-term continuous record. The high spatial resolution maps derived from the dual RSS-GAN encountered extended data gaps (Figure 3.8), since cloud-induced gaps are

common in the original Landsat archive datasets (Ju and Roy, 2008). Although the spatiotemporal image fusion methods (Moreno-Martínez et al., 2020; Zhu et al., 2018) could supplement land surface observations during the MODIS era (since 2000), the gap-filling process is inevitable for the Landsat long-term record. For example, some methods fill missing values in partially contaminated Landsat images using pixel values from spectrally similar land cover classes (Chen et al., 2011b; Luo et al., 2018; Yan and Roy, 2018; Yan and Roy, 2020) while other methods fit models to time series data to predict nonlinear land surface changes during cloud cover and missing acquisition data (Adeluyi et al., 2021; Chen et al., 2021; Yin et al., 2019). When the spatial resolution of maps is high, more pixels and spatial details disappear compared to low-medium resolution maps, even if there is a data gap in the same space, especially in heterogeneous areas. Thus, we would encourage future studies to develop high fidelity gap-filling methods for high resolution Landsat maps, like object-based gap-filling methods for PlanetScope dataset (Wang et al., 2022).

The dual RSS-GAN model is associated with a number of potential uncertainties. First, the results generated by the RSS-GAN model are non-deterministic, which means that it cannot reproduce exactly the same results even with identical input data. This type of model uncertainty originates from the stochastic basis of the GAN generator and discriminator. Nevertheless, the dual RSS-GAN model produced vegetation maps that exhibited robust performances with respect to *in situ* measurements (Figures 3.9 and 3.10). Second, the number of epochs used in this study (Section 2.7) does not represent a universally generic value for the dual RSS-GAN; each researcher should optimize it based on a localized training dataset. The lack of

reproducibility may lead to small variations in the performance of the dual RSS-GAN model. This variation could be reduced through a very long training process but the long training process results in an overfitted model that fails to predict observations because of training dataset memorization (Yang and E, 2022). To avoid model overfitting, you would need to reduce either variance or bias (not both) (Geman et al., 1992). Moreover, a stable performance during the training process does not necessarily ensure a stable performance in practice. To achieve stable performance without overfitting, the number of epochs should be optimized according to the practical situation (e.g., sample number and model structure) (Yazici et al., 2020). Third, the performance of the dual RSS-GAN used in this study may degrade in areas beyond Planet Fusion tiles. Even though drastic changes in land-use and land cover occurs in 30 m scale (i.e., the size of Landsat 8 pixel), the dual RSS-GAN can convey that into results, land surface changes in few meters scale could not be captured. Although the Planet Fusion tiles used in the present study included various land cover types (e.g., urban, mountain, forest, and cropland; Figure 3.1), the GAN model is likely to converge the stochastic distribution of the discriminator toward the stochastic distribution of the training dataset (Yang and E, 2021; Yang and E, 2022). Ideally, the number of Planet Fusion training tiles should match the scope of the research area when training the dual RSS-GAN model to achieve optimal performances.

Our results highlight the potential of the dual RSS-GAN model to enhance the spatial resolution of past satellite datasets using high resolution CubeSat-based imagery. By projecting past information from present data, we generated a high spatial resolution 8-year record of vegetation index maps using 2 years of Planet Fusion data

for model training purposes. Previous studies have used high spatial resolution maps from CubeSat datasets to monitor vegetation phenology and leaf area index (Houborg and McCabe, 2018b; Johansen et al., 2022; Kimm et al., 2020; Wang et al., 2020a), suggesting potential applications of our dual RSS−GAN model results in those fields during past Landsat periods. While the dual RSS−GAN model demonstrated encouraging performance over cropland and deciduous forest study regions additional evaluation is required across a wider range of ecosystems including tropical forests and arctic regions, where land cover has substantially changed in recent decades (Achard et al., 2004; Houghton and Nassikas, 2017; Stow et al., 2004; Wang et al., 2020b).

5. Conclusion

Spatial resolution enhancement of historic satellite datasets is essential for monitoring and resolving long-term changes in vegetation within fine-grained/heterogeneous landscapes. In this study, we proposed a dual RSS-GAN super-resolution model trained using day-coincident Planet Fusion and Landsat 8 products for generating long-term spatially enhanced satellite data. The results demonstrated a robust performance of the dual RSS-GAN model against in situ measurements over cropland and deciduous forest sites from 2013 to 2021. The dual RSS-GAN model retained the strengths of GAN-based methods in terms of rescaling and reducing the underestimation of vegetation indices evident in the original Landsat 8 data. The proposed approach offers promise for the adoption of dual RSS-GAN models in monitoring long-term vegetation dynamics with high spatial resolution (i.e., 3 m). We anticipate future efforts to further explore the use of GAN-based methods for vegetation monitoring across a variety of ecosystems that have experienced substantial changes in land cover in recent decades.

Appendices

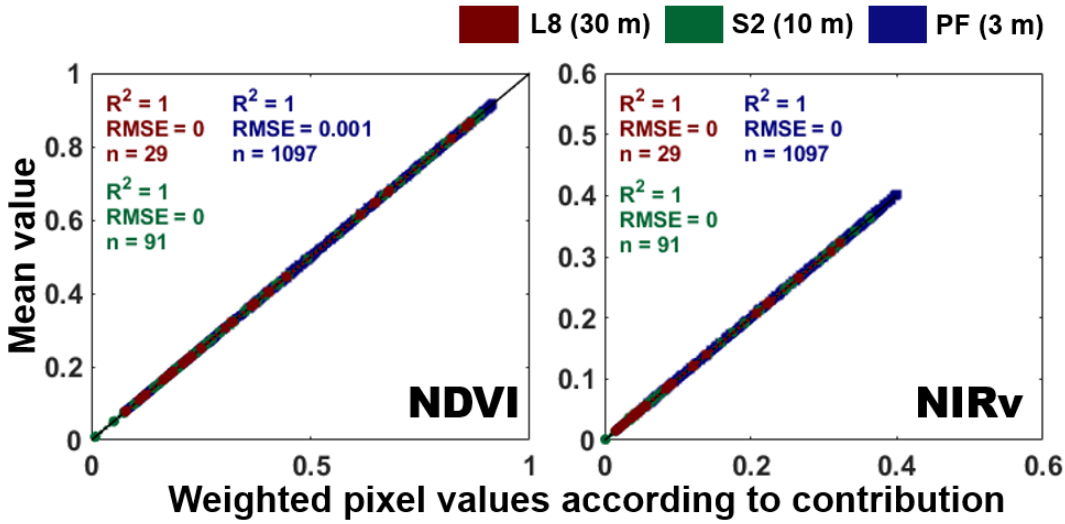

Figure A3.1 Differences in NDVI and NIRv according to aggregation method in satellite product pixels within *in situ* measurement footprint. The x-axis indicates the pixel value weight (Shuai et al., 2014); the y-axis indicates the mean pixel values within the footprint.

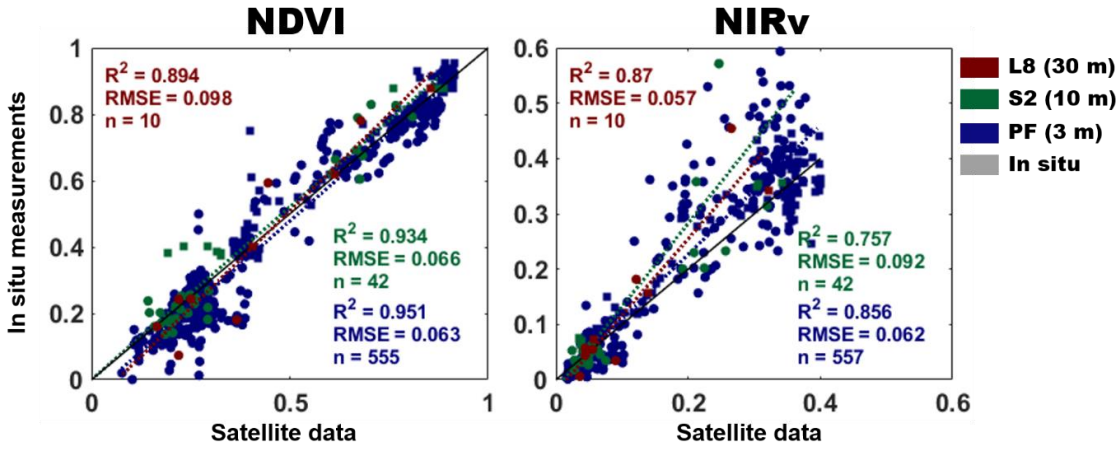

Figure A3.2 Evaluation of Planet Fusion (PF; dark blue), Sentinel 2 (S2; dark green), and Landsat 8 (L8; dark red) NDVI and NIRv against all available *in situ* measurements in deciduous forest (GDK; square), cropland (CRK; circle).

Table A3.3 Evaluation of NDVI and NIRv results derived from Landsat 8 NBAR (L8), LP10, and LP3 data, Landsat 8 NBAR data interpolated using the nearest-neighbor method, and Landsat 8 NBAR data interpolated using the bilinear method. Model-derived NDVI and NIRv results were compared with *in situ* measurements. R^2, coefficient of determination; RMSE, root mean square error; rbias, relative bias; n, number of samples.

NDVI					
Site	Data	R^2	RMSE	rbias (%)	n
Overall	L8	0.957	0.058	−5.7	64
	LP10	0.967	0.049	−1.5	64
	LP3	0.963	0.052	−0.2	64
GDK	L8	0.945	0.053	−4.9	46
	LP10	0.948	0.048	−1.4	46
	LP3	0.947	0.049	−0.1	46
CRK	L8	0.901	0.044	−10.3	18
	LP10	0.944	0.036	−2.3	18
	LP3	0.930	0.039	−0.8	18
NIRv					
Site	Data	R^2	RMSE	rbias (%)	n
Overall	L8	0.921	0.032	−11.6	64
	LP10	0.905	0.035	−11.1	64
	LP3	0.915	0.035	−4.9	64
GDK	L8	0.902	0.034	−11.5	46
	LP10	0.891	0.039	−11.6	46
	LP3	0.893	0.038	−4.8	46
CRK	L8	0.921	0.015	−12.1	18
	LP10	0.972	0.009	−7.1	18
	LP3	0.958	0.011	−5.8	18

Supplementary material

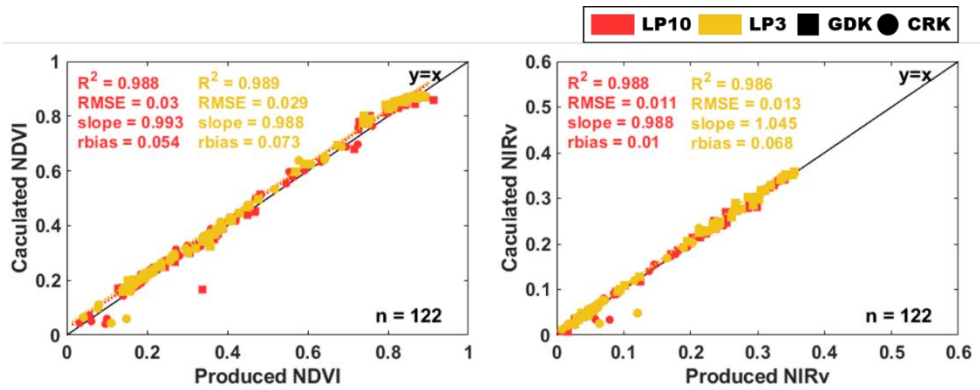

Figure S3.1 Comparison of calculated and produced vegetation indices (NDVI and NIRv) of in the dual RSS-GAN model (LP10 and LP3) in deciduous forest (GDK; square), cropland (CRK; circle). 'Calculated' is designated vegetation index that calculated from emulated red and NIR band; 'Produced' is designated vegetation index that calculated from the model-produced NDVI band and NIR band.

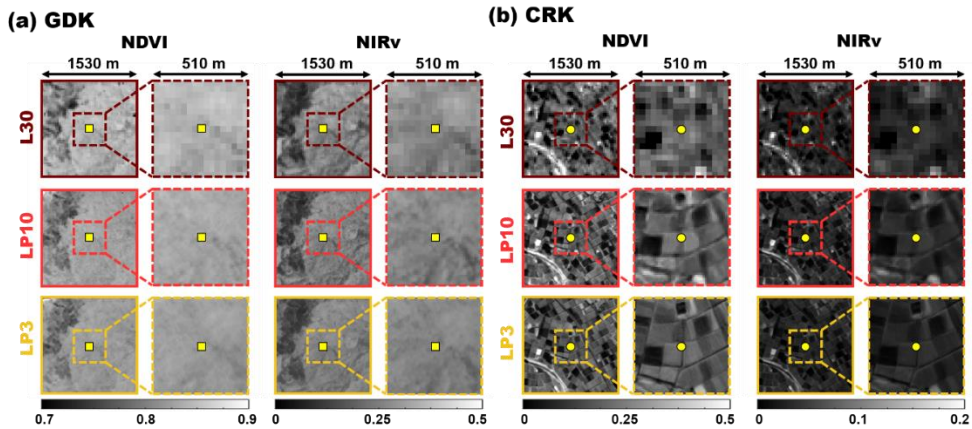

Figure S3.2 Example NDVI and NIRv images produced by the dual RSS–GAN model (LP10 and LP3) and Landsat 8 (L30) images in gray scale over (b) the GDK site (yellow square) and (b) the CRK site (yellow circle) on May 9, 2018. Overall landscape (1530 m × 1530 m) and flux tower area subsetted (510 m × 510 m) images are shown. The bottom panel shows the corresponding NDVI and NIRv histograms for L30, LP10, and LP3. NDVI and NIRv are unitless.

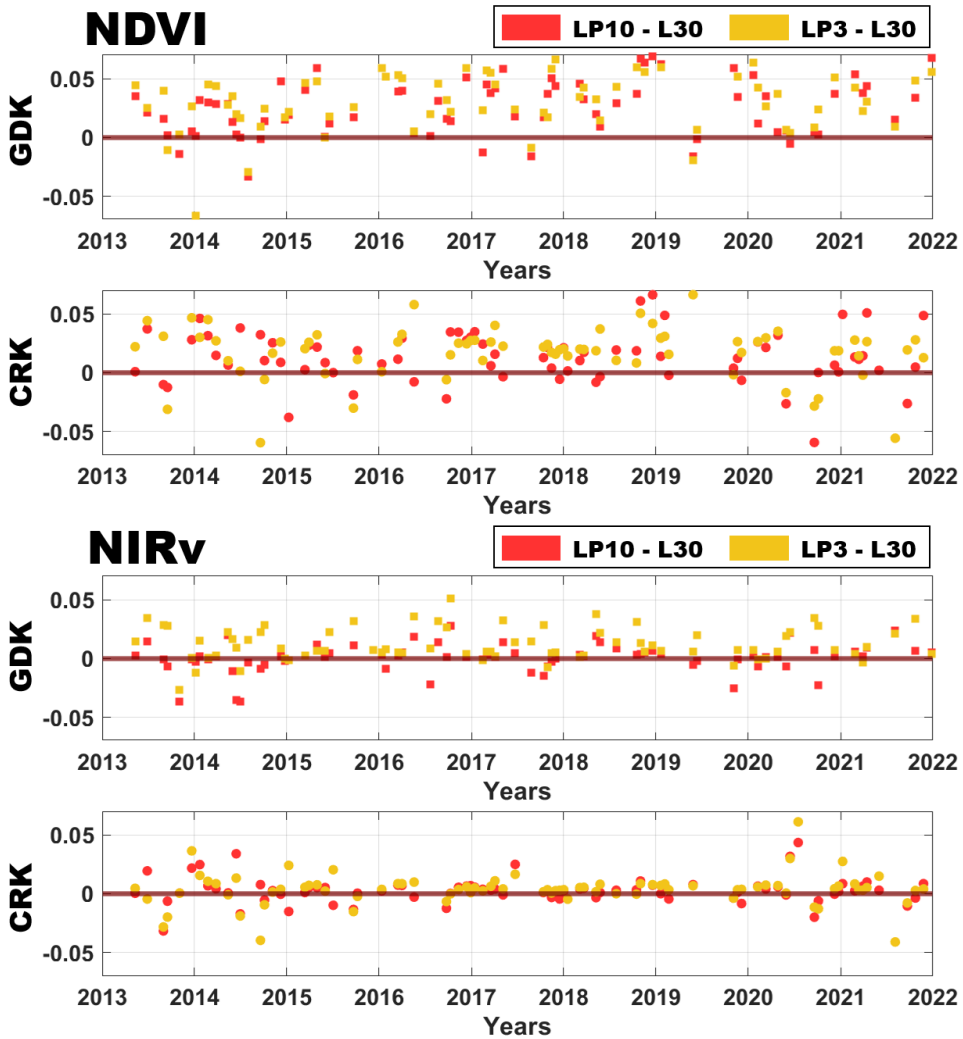

Figure S3.3 Seasonal variation of difference between vegetation indices (that is, NDVI and NIRv) derived from the dual RSS–GAN model (Model–LP10, LP10; Model–LP3, LP3) and the satellite NBAR (Landsat 8, L30) at each site (GDK, deciduous forest, square; CRK, cropland, circle). NDVI and NIRv are unitless.

Chapter 4. Matching high resolution satellite data and flux tower footprints improves their agreement in photosynthesis estimates

1. Introduction

High spatio-temporal resolution of satellite imagery is not only important to monitor vegetation, it is also crucial for the validation of remote sensing-based GPP products with flux tower measurements (Chen et al., 2011a; Ran et al., 2016). While the footprint of eddy covariance flux towers covers a relatively large area (more than 1 km^2 for 80 % cumulative contribution of fluxes) (Chen et al., 2009; Chen et al., 2012), its location, size and shape change continuously, driven by surface roughness and meteorological factors such as wind direction and speed (Kljun et al., 2015; Prabha et al., 2008; Schmid, 1997). Although footprint variations can affect the feasibility to match flux tower GPP with satellite products in any type of ecosystem due to spatial heterogeneity within the flux tower footprint (Giannico et al., 2018), it is a key factor in heterogeneous landscapes as contributions to the tower GPP can come from different land cover types (Ran et al., 2016). Due to the limitations in the spatial resolution of available satellite imagery, this aspect of flux tower footprint shape, size and dynamics has mostly been circumvented by selecting only flux tower sites within large patches of relatively homogeneous ecosystems (Liang et al., 2019; Zhang et al., 2020). Even in such cases of consistent land cover within the flux tower footprint, however, the assumption of spatial homogeneity of GPP within the flux tower footprint might not be justified. An important aspect related to this is that even for tower-based, near-surface sensing techniques, covering the entire flux tower footprint

with tower-based optical sensors is virtually impossible even when a bi-hemispheric viewing geometry is used (Gamon, 2015; Liu et al., 2017a; Marcolla and Cescatti, 2018).

Remotely monitoring GPP at both high spatial and temporal resolution has been challenging due to the trade-off between spatial and temporal resolutions in observations from sun-synchronous satellites. Most publicly available satellite-derived surface reflectance products, therefore, have either coarse spatial resolution (e.g., 250 m - 1 km) with high revisit frequency (e.g., one day for Moderate Resolution Imaging Spectrometer; MODIS) (Justice et al., 1998) or fine spatial resolution (e.g., 10 m -30 m) with revisit frequency (e.g., up to 16 days for Sentinel 2 and Landsat 8) (Claverie et al., 2018; Drusch et al., 2012b; Roy et al., 2014a), which can effectively result in much lower temporal resolution in many areas due to frequent cloud cover. While many image fusion techniques have been developed (Zhu et al., 2018) and rather successfully applied to partly overcome the trade-off between spatial and temporal resolutions, these approaches still have important limitations. For example, forcing data with a coarse spatial resolution can result in bias against ground measurements, especially in heterogeneous landscapes (Kong et al., 2021).

A recent solution to spatiotemporal trade-offs in satellite observations have been satellite constellations, which consist of a high number of, typically small satellites (i.e., CubeSat; (https://www.cubesat.org/)). CubseSat consists of multiple cubic units (1 unit = 10 cm × 10 cm × 10 cm) but weights, less than 1.33kg unit^{-1}. On the other hand, it introduces another challenge of cross-calibration between a large number of sensors. The Cubesat-enabled Spatio-Temporal Enhancement Method (CESTEM)

overcomes the challenges of low radiometric quality and cross-sensor inconsistency among CubeSat images by radiometric normalization using satellite images from rigorously calibrated sensors (Helder et al., 2020; Houborg and McCabe, 2018a). Indeed, CESTEM outperformed other image fusion products in capturing spatial and temporal variation in an *in situ* NDVI dataset for a heterogeneous rice paddy landscape (Kong et al., 2021) and has shown great potential for agricultural applications (Aragon et al., 2018; Aragon et al., 2021; Houborg and McCabe, 2018b). Moreover, Planet Fusion, which is based on CESTEM algorithm, conducts both inter-sensor radiometric harmonization and gap-filling process to deliver daily cloud-free 4-band (blue, green, red, and near infrared; NIR) surface reflectance data with 3 m resolution (PlanetFusionTeam, 2021).

Recently, NIR radiation reflected from vegetation has shown promising results in terms of estimating GPP at the field scale of a diverse range of vegetation types (Baldocchi et al., 2020; Dechant et al., 2022; Dechant et al., 2020). NIR reflectance from vegetation is approximated using the NIRv index as the product of the normalized difference vegetation index (NDVI) and NIR reflectance (Badgley et al., 2017). It accurately estimates monthly and annual GPP variations over globally distributed flux tower sites (Badgley et al., 2019). However, reflectance does not include information regarding the amount of incoming photosynthetically active radiation (PAR), which is a dominant factor driving daily GPP variation. Therefore, NIR radiation reflected from vegetation (NIRvP), which is the product of NIRv and PAR, has been proposed as a structural proxy for GPP estimation (Dechant et al., 2022; Dechant et al., 2020; Wu et al., 2020) and has been widely applied at hourly to daily timescales for

site-level and larger scale of GPP estimation since then (Baldocchi et al., 2020; Dechant et al., 2022; Dechant et al., 2020; Jiang et al., 2021; Liu et al., 2020).

Baldocchi et al. (2020) found that NIRvP from *in situ* spectral sensors tracked diurnal to seasonal variations of tower-based GPP well for individual sites, but that the slopes in the NIRvP-GPP regressions varied considerably across sites and years. As the study of Baldocchi et al. (2020) included spatially heterogeneous sites such as wetlands with considerable variation in water extent and cropland with frequent mowing, the variation in regression slopes could at least partly be due to the footprint mismatch between spectral sensors and eddy covariance systems on the flux towers. This aspect is explored in detail in our study by generating daily, 3 m GPP maps from CubeSat NIRvP and considering different scenarios to link the satellite-based GPP to the tower observations. In particular, I attempted to answer the following scientific questions:

(i) Does matching daily flux tower footprints with high resolution (3 m) NIRvP improve correlation to GPP compared to a larger fixed area around the tower and *in situ* spectral measurements?

(ii) How do the spatial and temporal resolution of satellite data impact the relationship between NIRvP and GPP when matching the flux tower footprint?

2. Methods

2.1 Study sites

To evaluate Planet Fusion-based GPP estimates, I selected study wetland and crop sites that had in situ measure measurements of NIRvP in the Sacramento-San Joaquin River delta in California, USA (Figure 4.1), which are registered in AmeriFlux and FLUXNET (Baldocchi et al., 2001; Pastorello et al., 2020). The five study sites included three restored wetlands (US-Tw4, US-Myb, and US-Snf) and two crop fields (US-Bi1 and US-Bi2 which are alfalfa and corn, respectively), located on Sherman, Bouldin, and Twitchell Islands (Table 4.1). Ideal conditions for eddy covariance measurements include a homogenous and flat landscape and few disturbances, which is physically impossible in the real world (Chu et al., 2021). For example, the wetland sites had a complex mosaic of water and vegetation. The alfalfa site underwent repeated cuttings and regrowth over an annual course. The corn site had a short growing season, and was plowed and flooded for a period during the year Moreover, the summer growing season is mostly cloud free, hence a suitable venue for evaluating satellite products.US-Bi1 (Rey-Sanchez et al., 2021b) (Alfalfa) is an alfalfa field (*Medicago sativa* L., a C3 plant), which is harvested five to seven times per year and periodically grazed with sheep (Rey-Sanchez et al., 2021c); US-Bi2 (Rey-Sanchez et al., 2021a) (Corn) is a corn field (*Zea mays* L., a C4 plant), which is harvested once per year and flooded in the winter. Two of the wetlands were restored from other land uses over the past decade. US-Myb (Matthes et al., 2021) (Palustrine wetland) was restored from a livestock pasture in 2010 and US-Tw4 (Eichelmann et al., 2021) (Freshwater wetland) was restored from a

cornfield in 2013; both sites have heterogeneous bathymetry (Chamberlain et al., 2018). The dominant vegetation in US-Myb and US-Tw4 is a mixture of tules (*Schoenoplectus acutus*, a C3 plant) and cattails (*Typha spp*, a C3 plant) in shallow water (water table depth < 40 cm) (Eichelmann et al., 2018; Valach et al., 2021). US-Snf (Kusak et al., 2020) (Pasture) is a wetland, more specifically peatland (Kasak et al., 2021) and is also used as a pasture to graze cattle throughout the seasons. The peak growing season over pasture site was around December to June. All study sites are registered with the AmeriFlux Network with publicly available data (Hemes et al., 2019).

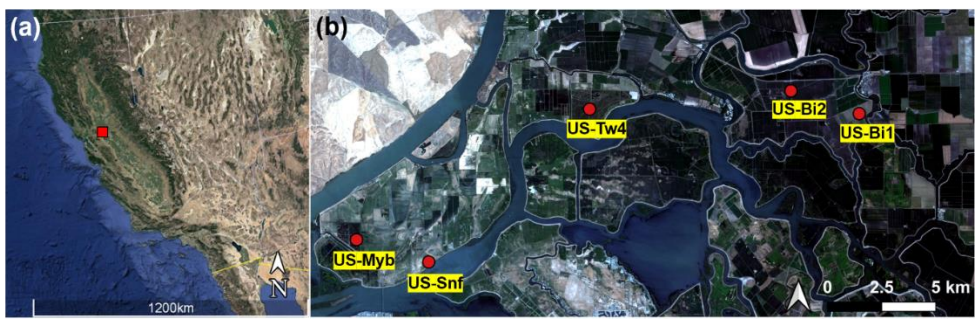

Figure 4.1 Maps of the study sites. (a) A map of California. (Image source: Google Earth) with the location of Sacramento–San Joaquin River delta area indicated by the red square. (b) The Sacramento–San Joaquin River delta area with red points that indicate study sites. Image source: red–green–blue (RGB) Planet Fusion surface reflectance product for July 1, 2018 (resolution, 3 m; projection, WGS84/UTM zone 10N; area, 30.6 km × 14.2 km = 433 km^2).

Table 4.1 List of study sites. Latitude and longitude of the flux tower (projection, WGS84) were adjusted from sub-meter spatial resolution satellite images from Google Earth and confirmed by field visits (Figure S1). The normalized difference vegetation index (NDVI) sensor position indicates distances (m) from the flux tower to the east and north, as well as height.

Site name (Site ID) DOI for citation	Type	Typical vegetation	Study period	Latitude, Longitude NDVI sensor position
Bouldin Alfalfa (US-Bi1) https://doi.org/10.17190/AMF/1480317	Crop (Alfalfa)	Medicago sativa L. (Hemes et al., 2019)	2018-01-01 to 2018-12-31	38.099161, -121.499336 2.89, -2.78, 2.7
Bouldin Corn (US-Bi2) https://doi.org/10.17190/AMF/1419513	Crop (Corn)	Zea mays (Knox et al., 2015)	2018-01-01 to 2018-12-31	38.109078, -121.535122 -2.03, -1.94, 4.42
Twitchell Wetland East End (US-Tw4) https://doi.org/10.17190/AMF/1246151	Wetland	Schoenoplectus acutus & Typha spp. (Hemes et al., 2020)	2018-01-01 to 2018-12-31	38.102747, -121.641325 -2.17, -1.73, 4.73
Mayberry (US-Myb) https://doi.org/10.17190/AMF/1246139	Wetland	Schoenoplectus acutus & Typha spp (Eichelmann et al., 2018)	2019-01-01 to 2019-12-31	38.049864, -121.765006 3.10, 2.3, 4
Sherman Barn (US-Snf) https://doi.org/10.17190/AMF/1579718	Wetland (Pasture)	* Unreported (Kasak et al., 2021)	2019-07-19 to 2019-12-31	38.040208, -121.727161 -1.49, -2.49, 2.75

2.2 *In situ* measurements

To evaluate GPP estimates derived from CubeSat NIRvP maps, I compared them with *in situ* carbon flux measurements from eddy covariance systems, surface reflectance measurements from NDVI sensors, and quantum sensor PAR measurements.

The eddy covariance systems included open-path infrared gas analyzers (LI-7500A for CO_2 and H_2O, LI-7700 for CH_4; LiCOR Inc., Lincoln, NE, USA), and three-dimensional sonic anemometers (WindMaster Pro 1590, Gill Instruments Ltd, Lymington, Hampshire, UK) that measure sonic temperature and three-dimensional wind speeds at 20 Hz. High-frequency raw data processing and flux computations were performed in accordance with the methods of Pastorello et al. (2020). Briefly, standard processing procedures included spike removal for 20-Hz raw data, coordinate rotations within each 30-min block for anemometer tilt correction, block averaging for 30-min fluxes of net ecosystem CO_2 exchange (NEE), air density corrections and site-specific friction velocity filtering. Furthermore, I applied a neural network procedure (Moffat et al., 2007) to fill the gaps in 30-min NEE time series and then partitioned NEE into ecosystem assimilation and ecosystem respiration flux densities using the nighttime approach (Reichstein et al., 2005). A detailed description about flux data processing, gap-filling and partitioning can be found in Eichelmann et al. (2018) and Knox et al. (2015). The proportion of gap-filled GPP at each site during the study period was 36.8 % (US-Bi1; Alfalfa), 27.6 % (US-Bi2; Corn), 25.2 % (US-Tw4; Freshwater wetland), 27.0 % (US-Myb; Palustrine wetland), and 25.3 % (US-Snf; Pasture).

In situ NIRv data were derived from NDVI sensors (Decagon SRS-Ni, Pullman, WA, USA) that measured incident and reflected radiation

in the red (630 nm; full−width, half−maximum, 50 nm) and NIR (800 nm; full−width, half−maximum, 40 nm) spectral bands. NDVI sensors were mounted on booms extended from the flux tower (Table 1). I measured bi−hemispheric reflectance by using hemispherical view for both upward and downward looking sensors to increase the area of the footprint viewed by the NDVI sensors (Baldocchi et al., 2020). Although the field of view of the NDVI sensors with bi−hemispheric view include the tower structure, this is expected to be a small, and temporally constant bias. In particular, the NDVI of the tower structure elements is expected to be very low, effectively decreasing the contribution to NIRv. Planet Fusion (Section 2.3) provides a bidirectional reflectance factor that differs from bi−hemispheric reflectance; therefore, I tested the impacts of the different reflectance quantities on NIRv over two study sites using satellite−derived bidirectional reflectance distribution function (BRDF) parameters and the result demonstrated a negligible difference (Figure A1). Moreover, radiometric calibration had been done for each NDVI sensor before and after the growing season but slow drift year after year in NDVI sensor over the site (US−Tw4)was not a scope of uncertainty in this study as I only used single year data. At each tower, *in situ* incoming PAR data (μmol m^{-2} s^{-1}) were measured by quantum sensors (PAR-Lite or PQS1, Kipp & Zonen, Delft, Netherlands).

To align the time between continuous *in situ* measurements and Planet Fusion data that rely on morning to around noon overpass time of satellites such as Sentinel 2 (around 1015hh – 1030hh) and Landsat 8 (around 1015hh – 1030hh), and MODIS nadir BRDF−adjusted reflectance (local solar noon), I averaged *in situ* measurements (i.e., GPP, PAR, and NIRv, hereafter $\mathbf{NIRv}^{\mathbf{in\ situ}}$)

between 1030hh. and 1230hh to align it to Planet Fusion data. For daily GPP and *in situ* daily NIRvP (**daily NIRvP$^{in\ situ}$**), I summed half-hourly GPP and half-hourly *in situ* NIRvP over the whole day (0000hh – 2400hh) to obtain daily sum values, respectively.

2.3 Planet Fusion NIRvP

NIRvP was calculated on the basis of Planet Fusion (PF) surface reflectance data (PlanetFusionTeam, 2021). Planet Fusion constitutes a comprehensive harmonization and fusion methodology based on the CESTEM algorithm (Houborg and McCabe, 2018a; Houborg and McCabe, 2018b). Planet Fusion performs multi-sensor inter-calibration, harmonization, enhancement, and fusion leveraging rigorously calibrated and freely available datasets from Sentinel-2, Landsat 8, Moderate Resolution Imaging Spectroradiometer (MODIS), and Visible Infrared Imaging Radiometer Suite (VIIRS) in concert with the higher spatial and temporal resolution CubeSat images from the PlanetScope Constellations. Planet Fusion uses the Framework for Operational Radiometric Correction for Environmental Monitoring (FORCE) (Frantz, 2019a) to generate a 30 m harmonized Sentinel-2 and Landsat 8 BRDF adjusted surface reflectance product to be used as the calibration target during the CESTEM-based radiometric harmonization step. In that harmonization step, a cubist rule-based regression technique was used for constructing band-specific prediction models, which were trained by the FORCE-based Sentinel-2 and Landsat 8 surface reflectance product (30 m) and aggregated-PlanetScope data (30 m). Further details on the original CESTEM methodology are in Houborg and McCabe (2018a). Additional Planet Fusion features include 1) sub-pixel fine geometric alignment of source imagery, 2) rigorous, temporally driven, cloud

and cloud shadow detection to remove the cloud-related pixels, 3) fusion of Sentinel-2 and Landsat 8 data to help fill gaps in PlanetScope coverage, and 4) advanced gap-filling (PlanetFusionTeam, 2021). Planet Fusion delivers daily, gap-filled, 4-band (0.45 – 0.51 μm, blue; 0.53 – 0.59 μm, green; 0.64 – 0.67 μm, red; 0.85 – 0.88 μm, NIR) sensor agnostic surface reflectance data characterized by enhanced radiometric stability and consistency across space and time to support advanced analytics. Planet Fusion product is generated with a 3 m pixel size as regularly gridded raster tiles (24 by 24 km) in UTM projection. In this study, Planet Fusion data were provided for the years 2018 and 2019 by utilizing Harmonized Landsat and Sentinel (referred to as HLS from hereon) (Claverie et al., 2018) as the calibration target, which is different from the currently available Planet Fusion product that uses FORCE-based Sentinel-2 and Landsat surface reflectance product.

To calculate instantaneous Planet Fusion -based NIRvP, I used NIRv maps from Planet Fusion data and PAR from tower-based quantum sensors located at the sites. First, I calculated NDVI maps using Planet Fusion red and NIR reflectance maps, according to Eq. (1). Then, I multiplied them by NIR reflectance to generate NIRv maps, according to Eq. (2). Finally, I applied Eq. (3) to estimate NIRvP for each site using averaged PAR data collected by *in situ* PAR sensors around satellite overpass time. Although Planet Fusion inherits overpass time of Sentinel 2 and Landsat 8 (around 1015hh – 1030hh) in theory, I assumed the time window between 1030hh and 1230hh when aligning it to *in situ* data. MODIS affects the daily variation of Planet Fusion more than Sentinel 2 and Landsat. Specifically, MCD43A4 products (Schaaf et al., 2002), which are forcing data for Planet Fusion, use the data from both MODIS terra

(overpass at 1030hh) and MODIS aqua (overpass at 1330hh).

$$\mathbf{NDVI} = \frac{\boldsymbol{\rho}\mathbf{NIR} - \boldsymbol{\rho}\mathbf{Red}}{\boldsymbol{\rho}\mathbf{NIR} + \boldsymbol{\rho}\mathbf{Red}} \quad \text{Eq. (1)}$$

$$\mathbf{NIRv} = \boldsymbol{\rho}\mathbf{NIR} \times \mathbf{NDVI} \quad \text{Eq. (2)}$$

$$\mathbf{NIRvP} = \mathbf{NIRv} \times \mathbf{PAR} \quad \text{Eq. (3)}$$

where ρNIR and ρRed are reflectance in the NIR and red regions, respectively.

To generate daily Planet Fusion NIRvP maps, I used both satellite-derived daily summed PAR data and *in situ* PAR data. As Planet Fusion products are snapshots of daytime conditions around satellite overpass time, rather than daily accumulated values, I temporally upscaled Planet Fusion NIRvP around the satellite overpass time to generate daily Planet Fusion NIRvP ($\mathbf{daily\ NIRvP}^{\mathbf{PF}}_{\mathbf{ECfootprint}}$). This temporal upscaling process successfully upscaled GPP (Ryu et al., 2012), using a simple cosine function computed from the solar zenith angle, latitude, and longitude. For the application of Planet Fusion NIRvP where *in situ* PAR were not available, I multiplied Planet Fusion NIRv with daily summed PAR data (BESS daily PAR, 5 km; $\mathbf{daily\ PAR}^{\mathbf{BESS}}$) (Ryu et al., 2018), which were retrieved from the satellite-based Breathing Earth System Simulator (BESS) PAR product (Ryu et al., 2011) (Figure 4.2). The BESS PAR product uses MODIS Terra and Aqua data to upscale available instantaneous PAR estimates into daily summed values by combining an atmospheric radiative transfer model (i.e., Forest Light Environmental Simulator, FLiES; Kobayashi and Iwabuchi (2008)) with an artificial neural network. The $\mathbf{daily\ PAR}^{\mathbf{BESS}}$ data showed a strong linear relationship to daily $\mathbf{PAR}^{\boldsymbol{in\ situ}}$ data with little bias (R^2 = 0.97, relative bias = −0.8%) (Figure A4.2).

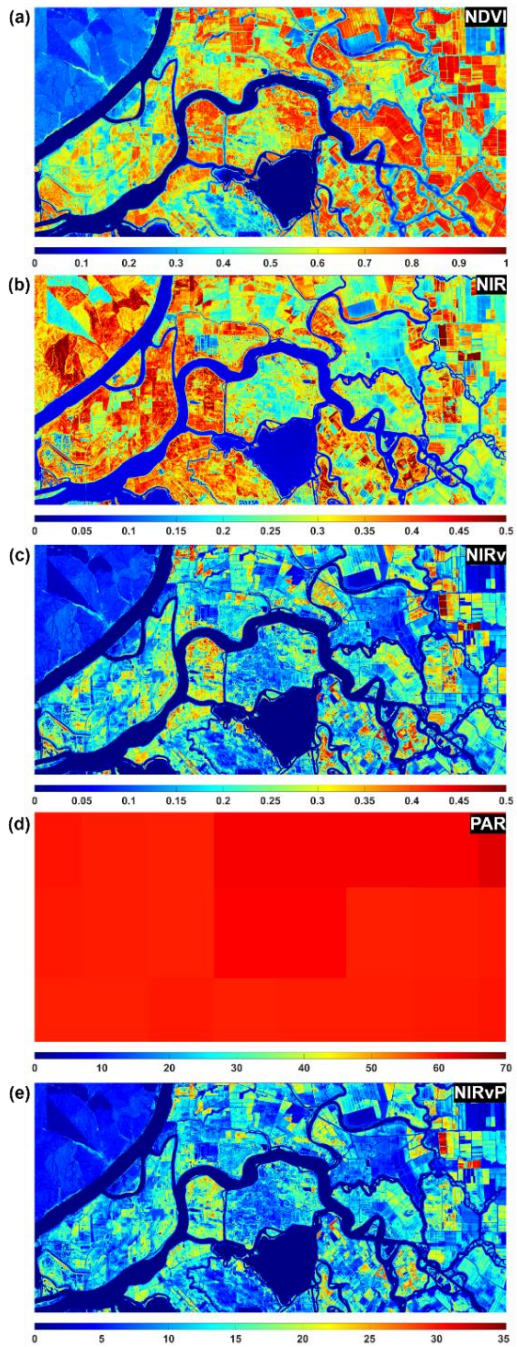

Figure 4.2 Maps of (a) NDVI, (b) NIR, (c) NIRv, and (d) BESS daily PAR (e) NIRvP derived from the combined Planet Fusion surface reflectance product (3 m resolution) and BESS daily PAR product (5 km resolution) on July 1, 2018 (projection, WGS84/UTM zone 10N; area, 30.6 km × 14.2 km = 433 km^2). NDVI, NIR, and NIRv are given in unitless; PAR and NIRvP are given in unit of mol m^{-2} d^{-1}. NIRvP maps of different times during the year is (Figure S4.2).

2.4 Flux footprint model

Flux footprints for each of the sites were calculated with the model from Kormann and Meixner (2001). This model outperformed other commonly-used flux footprint models according to a CO_2 gas release experiment (Kumari et al., 2020; Rey-Sanchez et al., in prep). Flux footprints were calculated for those half hours between 1030hh – 1230hh, and later aggregated at the daily level to produce 50, 60, 70, and 80% footprint contours. An 80% footprint contour indicates that 80% of the sources/sinks contributing to the signal detected by the eddy-covariance tower are located within the indicated area. Multiple contours were calculated to obtain a visual inspection of the exponential decay of the footprint past the 50 % contour line. The 80 % threshold selection is supported by Chu et al. (2021), who found that footprint area beyond the 80% contour had a minimal influence on the final calculations of footprint representativeness in a study of monthly footprint-weight maps. To obtain highly accurate footprint contours I calculated aerodynamic canopy height using the algorithm of Pennypacker and Baldocchi (2016), which has been shown to track detailed trends in the growth of wetland canopies at our study site (Kasak et al., 2020) and in other sites (Chu et al., 2018). Roughness length and displacement height were calculated as 0.1, and 0.66 of canopy height, respectively.

2.5 Evaluation

I evaluated the performance of the Planet Fusion -derived NIRvP product for GPP estimation by comparing it with *in situ* measurements from both NDVI sensor and eddy covariance system data (Chu et al., 2021). For that, I compared satellite-derived NIRv (and NIRvP) data with *in situ* measurements using several metrics.

The coefficient of determination (R^2) of the linear regression between NIRv(P) and GPP, which equals the square of the Pearson correlation coefficient, was used as the main metric to characterize the strength of the linear relationship and thus the GPP estimation performance of NIRv(P). The linear regression slope indicates the variation in the relationship of $\mathbf{NIRv^{PF}}$ (or $\mathbf{NIRvP^{PF}}$) to GPP for different ecosystem types. Root mean square error (RMSE), bias, and relative bias were calculated as follows:

$$\mathbf{RMSE} = \sqrt{\mathbf{E}((\mathbf{A}-\mathbf{B})^2)} \quad \text{Eq. (4)}$$

$$\mathbf{Bias} = \mathbf{E}(||\mathbf{B}-\mathbf{A}||) \quad \text{Eq. (5)}$$

$$\mathbf{rbias} = \frac{\mathbf{E}(||\mathbf{B}-\mathbf{A}||)}{\mathbf{E}(\mathbf{A})} \quad \text{Eq. (6)}$$

where A is the satellite product (i.e., MODIS, HLS, or Planet Fusion), B is *in situ* NIRv, and E is the mean operator.

First, I directly evaluated Planet Fusion NIRv against NIRv calculated from *in situ* sensors, which can be considered a direct ground validation. I estimated the footprints of *in situ* NDVI sensors based on their heights and locations (Table 4.1). Because NDVI sensors measure hemispherical irradiance, I approximate the 80% footprint of *in situ* NIRv from the area of 80% of upwelling irradiance, which can be estimated by considering the sensor height above the ground (Table 4.1) (Liu et al., 2017a). The estimated diameters of the NDVI sensor footprints ($NDVI_{sensor}$) were approximately 12 m (US-Bi1; Alflafa), 19 m (US-Bi2; Corn), 20 m (US-Tw4; Freshwater wetland), 12 m (US-Snf; Pasture), and 13 m (US-Myb; Palustrine wetland). I designated Harmonized Landsat/Sentinel (HLS) pixels that included $NDVI_{sensor}$ as a footprint type to be considered in the comparison of different approaches, inHLS. Thus, each inHLS

footprint contained one (US-Myb; Palustrine wetland) or two HLS pixels (US-Bi1, Alflafa; US-Bi2, Corn; US-Tw4, Freshwater wetland; or US-Snf, Pasture) (Figure 4.3 and A4.3). I compared the Planet Fusion NIRv product within the estimated footprint of the NDVI sensors ($\mathbf{NIRv^{PF}_{NDVIsensor}}$) and *in situ* NIRv measurements. I extracted HLS pixels covering NDVI sensor footprints (Figure 4.3 and A4.3) and extracted Planet Fusion NIRv data within the inHLS footprint ($\mathbf{NIRv^{HLS}_{inHSL}}$) to quantify spatial variation in NIRv.

Second, I evaluated Planet Fusion NIRv (and NIRvP) for GPP estimation by comparing it to GPP from the eddy covariance systems. The flux footprint indicates the source area of trace gases detected by an EC system and therefore can be used for pixel selection during CubeSat GPP evaluation. In this study, I used cumulative eddy covariance footprints up to 80% at satellite overpass time for each day (1030hh - 1230hh) ($EC_{footprint}$). When extracting Planet Fusion pixels within the $EC_{footprint}$, I weighted the pixel values based on footprint contribution. I used an 80% accumulated footprint area for the weighting. I split the weighting factors from 0-50%, 50-60%, 60-70% and 70-80% (Eq. (7)).

$$\mathbf{NIRv(P)_{ECfootprint}} = \sum_{k=1}^{N}\left(\frac{\mathbf{NIRv_k\ within\ CL_{50\,\%}}}{\mathbf{N\ within\ CL_{50\,\%}}} \times \frac{50}{80}\right) + \sum_{k=1}^{N}\left(\frac{\mathbf{NIRv_k\ between\ CL_{60\,\%}\ and\ CL_{50\,\%}}}{\mathbf{N\ between\ CL_{60\,\%}\ and\ CL_{50\,\%}}} \times \frac{60-50}{80}\right) + \sum_{k=1}^{N}\left(\frac{\mathbf{NIRv_k\ between\ CL_{70\,\%}\ and\ CL_{60\,\%}}}{\mathbf{N\ between\ CL_{70\,\%}\ and\ CL_{60\,\%}}} \times \frac{70-60}{80}\right) + \sum_{k=1}^{N}\left(\frac{\mathbf{NIRv_k\ between\ CL_{80\,\%}\ and\ CL_{70\,\%}}}{\mathbf{N\ between\ CL_{80\,\%}\ and\ CL_{70\,\%}}} \times \frac{80-70}{80}\right) \quad \text{Eq. (7)}$$

Where k is each pixel number in the total number(N) of pixels within the footprint area, $CL_{D\,\%}$ is D % footprint contour line.

I also chose a fixed 100 m by 100 m area centered on the flux

towers (Figure 3; Table 2), which is greater than the footprint of *in situ* NDVI sensor and partly covers the flux tower footprint, . Such fixed footprints have been applied in previous studies because of the use of coarse spatial resolution satellite products (Heinsch et al., 2006; Kim et al., 2006; Verma et al., 2015). I extracted Planet Fusion pixels from the fixed-area footprint (100 m x 100 m) centered on the towers ($\mathbf{NIRv}^{\mathbf{PF}}_{\mathbf{100m}}$) and the estimated footprint area at satellite overpass time for each day ($\mathbf{NIRv}^{\mathbf{PF}}_{\mathbf{ECfootprint}}$). Then, I compared $\mathbf{NIRv}^{\mathbf{PF}}_{\mathbf{NDVIsensor}}$, $\mathbf{NIRv}^{\mathbf{PF}}_{\mathbf{100m}}$, and $\mathbf{NIRv}^{\mathbf{PF}}_{\mathbf{ECfootprint}}$ (and corresponding NIRvP) with GPP estimates around satellite passing time to evaluate the GPP estimation performance of each footprint type.

Additionally, I used annual accumulated footprint over Alfalfa (Bi1), Corn (Bi2), and Freshwater wetland (Tw4) (Figure A4.3) to evaluate the impact of temporal resolution of Planet Fusion NIRvP on GPP estimation. The comparison of Planet Fusion pixels within annual accumulated footprints to GPP is in (Figure A4.9). I also resampled Planet Fusion data to a 30 m resolution using the nearest-neighbor interpolation method without antialiasing, which produced the results closest to *in situ* measurements when resampling Planet Fusion-like data from 3 to 30 m resolution (Kong et al., 2021). Next, I extracted pixels within $EC_{footprint}$ to test the effect of spatial resolution on GPP estimation performance by comparison with the original 3 m resolution (Li et al., 2008). Finally, I compared $\mathbf{daily\ NIRvP}^{\mathbf{PF}}_{\mathbf{ECfootprint}}$ and $\mathbf{NIRv}^{\mathbf{PF}}_{\mathbf{ECfootprint}}$ multiplied by $\mathbf{daily\ PAR}^{\mathbf{BESS}}$ against daily GPP. For each footprint type, I extracted pixels only when their centers were within the footprint (poly2mask; MATLAB; The MathWorks, Inc., Natick, MA, USA).

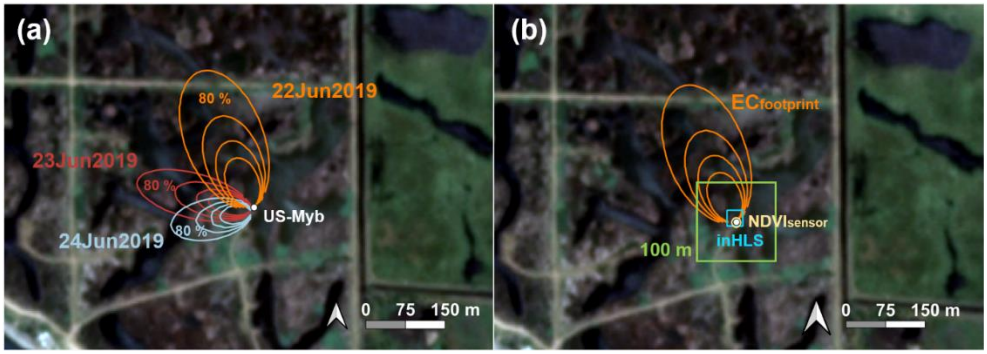

Figure 4.3 Examples of footprints for the US−Myb (Palustrine wetland) flux tower (white dot) between 1030hh to 1230hh (a) Daily eddy covariance (EC) footprints from June 22, 2019, to June 24, 2019. (b) eddy covariance footprint on June 22, 2018 (orange), a fixed 100 m × 100 m footprint (green) around the eddy covariance tower, and Harmonized Landsat/Sentinel (inHLS) pixels (cyan) including the normalized difference vegetation index (NDVI) sensor footprint (yellow) (Table 2). Contour lines denote footprints within which 50 – 80% (10% interval) of the cumulative flux originated. Image source: Planet Fusion RGB surface reflectance product for June 22, 2019 (projection, WGS84/UTM zone 10N). Footprints for *in situ* measurements at other sites are shown in (Figure A4.3 and A4.4).

Table 4. 2 Footprint types used in this study (Figure 4.3) and Abbreviations used to indicate data source, footprint type (i.e., $NDVI_{sensor}$, inHLS, 100m, $EC_{footprint}$) (Figure 4.2), and temporal scale (i.e., satellite overpassing time and daily) for NIRv, NIRvP, and PAR in this study. PF refers to Planet Fusion (Section 2.3); MODIS refers to nadir bidirectional reflectance distribution function adjusted reflectance product using MODIS data; HLS refers to Harmonized Landsat and Sentinel (Section 2.3), BESS refers to the satellite-based Breathing Earth System Simulator which is a platform to compute fluxes in carbon, water, and energy.

Footprint type	Description
$NDVI_{sensor}$	Footprint of the normalized difference vegetation index (NDVI) sensor. Diameter: 12 – 20 m
inHLS	Harmonized Landsat/Sentinel (HLS) pixel coverage that includes $NDVI_{sensor}$ Pixel size: 30 m × 30 m
100 m	A fixed 100 m × 100 m area centered on the flux tower
$EC_{footprint}$	Daily eddy covariance (EC) measurement footprint
Relevant aspect	**Abbreviation examples**
Temporal scale	NIRv (satellite overpassing time), daily NIRv (daily time scale)
Data source	$NIRv^{in\ situ}$, $NIRv^{PF}$, $NIRv^{MODIS}$, $NIRv^{HLS}$, PAR^{BESS}, $PAR^{in\ situ}$
Footprint type	$NIRv_{NDVIsensor}$, $NIRv_{inHLS}$, $NIRv_{100m}$, $NIRv_{ECfootprint}$
All combined	$NIRv^{PF}_{ECfootprint}$, $NIRv^{PF}_{100m}$, daily $NIRvP^{PF}_{ECfootprint}$, daily PAR^{BESS}

To evaluate the time series of NIRvP data against tower GPP data, I used nonparametric singular spectrum analysis, which decomposes and reconstructs time-series data to detect trends, remove long-term trends, and emphasize short-term variation (Ghil et al., 2002; Mahecha et al., 2007). A time series can be regarded as a collection

of additive components (e.g., trends, regular oscillations, and noise (Ghil et al., 2002)); therefore, I evaluated both trends (with low-frequency, smooth components) and oscillations (with high-frequency coherence). Singular spectrum analysis in this study consisted of two stages: decomposition and reconstruction. During the decomposition stage, I formed a time window with length L, which is half of the study period (L = N/2, where N is the length of a flux measurement with a unit of days), for each site and slid it along the time series to construct the L × K (K = N–L + 1) Hankel matrix $\mathbf{X}$. Then, I applied singular value decomposition to $\mathbf{X}$ to extract the eigenvalues and eigenvectors of $\mathbf{X}\mathbf{X}^{T}$. The leading singular value decomposition component (indicated by the largest eigenvalue) typically corresponds to the time-series trend (Alexandrov, 2009); therefore, I reconstructed the trend by inverting the projection from the leading component to a time series with length N. Subsequently, high-frequency (detrended) components were computed as the difference between the original time series and the trend. I conducted singular spectrum analysis using the R package *Rssa* v1.0.2 (Golyandina et al., 2018).

3. Results

This section reports the performance of Planet Fusion derived NIRv and NIRvP across different footprint types against *in situ* NIRv, NIRvP, and GPP.

3.1 Comparison of Planet Fusion NIRv and NIRvP with *in situ* NIRv and NIRvP

Planet Fusion NIRv in the footprint of *in situ* NDVI sensor ($\mathbf{NIRv}^{\mathbf{PF}}_{\mathbf{NDVIsensor}}$) showed better agreement with *in situ* NIRv ($\mathbf{NIRv}^{in\ situ}$) (R^2 = 0.74) compared to MODIS-derived NIRv ($\mathbf{NIRv}^{\mathbf{MODIS}}$) ($R^2$ = 0.44) or HLS-derived NIRv ($\mathbf{NIRv}^{\mathbf{HLS}}$) ($R^2$ = 0.69) (Figure 4). Even for daily gap-filled Planet Fusion data, linear relationships with $\mathbf{NIRv}^{in\ situ}$ were strong (R^2 > 0.82), with small RMSE values (< 0.1) at sites US-Bi2 (Corn), US-Snf (Pasture), US-Tw4 (Freshwater wetland), and US-Myb (Palustrine wetland) (Table A5). At US-Bi1 (Alfalfa), the relationship between $\mathbf{NIRv}^{\mathbf{PF}}_{\mathbf{NDVIsensor}}$ and $\mathbf{NIRv}^{in\ situ}$ had the highest RMSE (0.12). At all sites except US-Bi1(Alfalfa), the performance of $\mathbf{NIRv}^{\mathbf{PF}}_{\mathbf{NDVIsensor}}$ derived from gap-filled process in comparison with $\mathbf{NIRv}^{in\ situ}$ was similar to the performance of $\mathbf{NIRv}^{\mathbf{PF}}_{\mathbf{NDVIsensor}}$ derived from direct observation (Figure 4.5; Table A4.5). For NIRvP, regression analysis of $\mathbf{NIRvP}^{\mathbf{PF}}_{\mathbf{NDVIsensor}}$ and $\mathbf{NIRvP}^{in\ situ}$ at all sites showed strong linear relationships (R^2 = 0.83) with positive bias. Regression analysis of $\mathbf{NIRvP}^{\mathbf{MODIS}}$and $\mathbf{NIRvP}^{in\ situ}$ showed strong linear relationships at all sites, but with varying slopes (Figure 4.5). Thus, the overall performance of $\mathbf{NIRvP}^{\mathbf{MODIS}}$ in comparison with $\mathbf{NIRvP}^{in\ situ}$ (R^2 = 0.51) was worse than the overall performance of $\mathbf{NIRvP}^{\mathbf{PF}}_{\mathbf{NDVIsensor}}$ (R^2 = 0.79) and $\mathbf{NIRvP}^{\mathbf{HLS}}$ (R^2 = 0.73) against $NIRvP^{in\ situ}$, which had more consistent slopes (Figure 4.5, Table A4.5). Unlike the impacts of gap-filling on NIRv, gap-filled

$\mathbf{NIRvP}^{\mathbf{PF}}_{\mathbf{NDVIsensor}}$ showed a stronger linear relationship with $\mathbf{NIRvP}^{in\ situ}$ (R^2 = 0.90 – 0.98) than did $\mathbf{NIRvP}^{\mathbf{HLS}}$($R^2$ = 0.64 – 0.96). Meanwhile, gap–filled $\mathbf{NIRvP}^{\mathbf{PF}}_{\mathbf{NDVIsensor}}$ showed a stronger linear relationship with $\mathbf{NIRvP}^{in\ situ}$measurements at all sites (R^2 = 0.90 – 0.98) compared to observed $\mathbf{NIRvP}^{\mathbf{PF}}_{\mathbf{NDVIsensor}}$ (R^2 = 0.88 – 0.98) (Figure 5; Table A5). In each site and all sites pooled data, the proportion of observed Planet Fusion out of gap–filled Planet Fusion was 49 – 56% when the proportion of HLS out of that was 22 – 28% (Figure 4.4; Table A4.5).

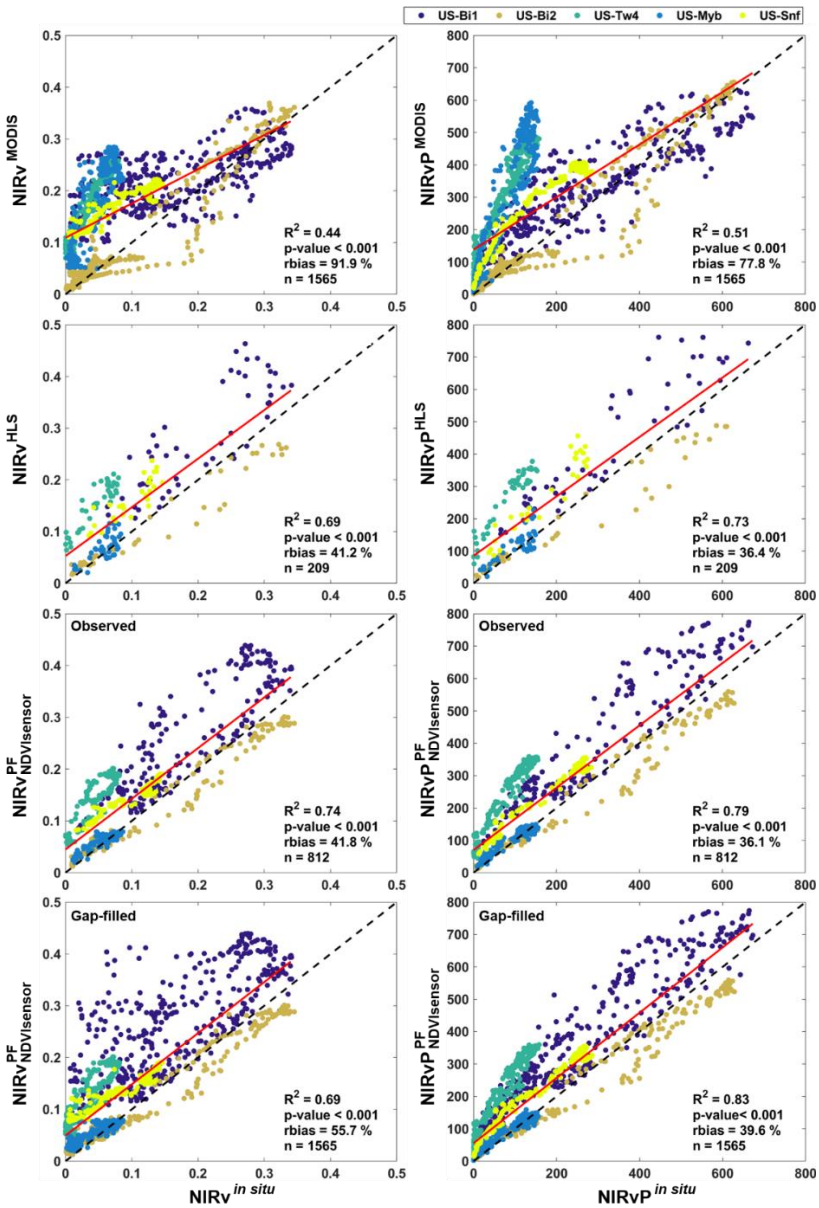

Figure 4.4 Comparison of measured *in situ* near−infrared radiation reflected from vegetation (NIRv) and the product of NIRv and photosynthetically active radiation (PAR) (NIRvP) around the satellite passing time with MODIS, HLS, observation−derived and gap−filled Planet Fusion (PF) data. Dashed black lines are 1:1 line (y = x). Red lines indicate linear regression model slopes for all sites. R^2 is the coefficient of determination, p−value indicates the significance of the linear regression, rbias is relative bias, and n is the number of samples used in the linear regression model. NIRv is unitless and NIRvP is in unit of μmol m^{-2} s^{-1}. Detailed analyses for each site are shown in (Table A4.5).

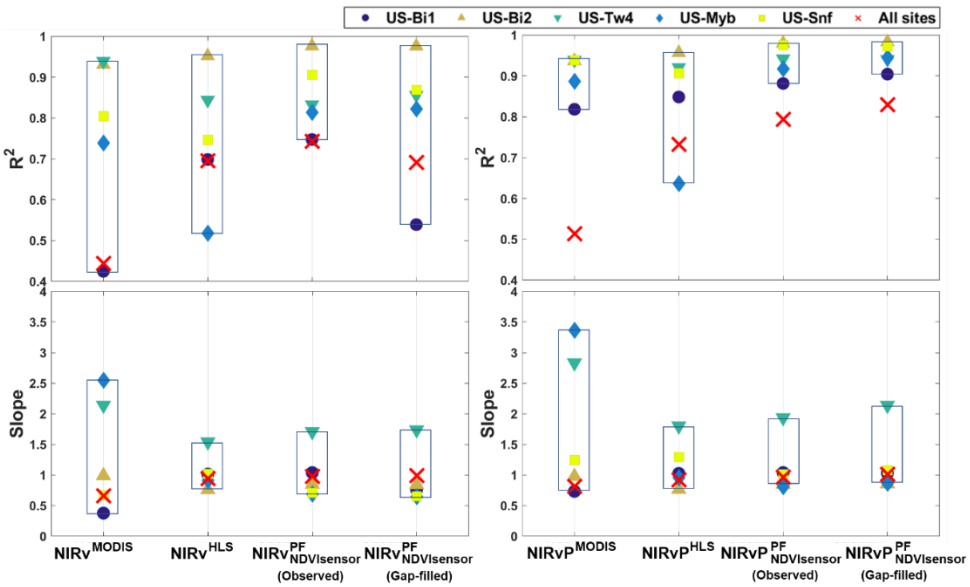

Figure 4.5 Comparison of measured *in situ* NIRv and NIRvP around the satellite passing time at each site and all sites pooled (colored symbols) with MODIS, HLS, and observation-derived and gap-filled Planet Fusion (PF) data. R^2 and the linear regression slope are indicated for each site. Detailed site data are provided in (Table A4.5).

3.2 Comparison of instantaneous Planet Fusion NIRv and NIRvP with against tower GPP estimates

$NIRvP^{PF}$ ($R^2 \leq 0.78$) performed better than $NIRvP^{in\ situ}$ ($R^2 = 0.61$) in estimating GPP when combining the data from all sites (Figure 4.6). The linear relationships between NIRvP and GPP for all site data combined showed the following ranking (in order of decreasing R^2): Planet Fusion NIRvP in daily flux tower footprints ($NIRvP^{PF}_{ECfootprint}$) > Planet Fusion NIRvP in a a fixed area footprint area around flux tower (100 m × 100 m) ($NIRvP^{PF}_{100m}$) > Planet Fusion NIRvP in the footprint of *in situ* NDVI sensor ($NIRvP^{PF}_{NDVIsensor}$) > *in situ* NIRvP ($NIRvP^{in\ situ}$), with R^2 values of 0.78, 0.65, 0.61, and 0.61, respectively. On the other hand, the linear relationships between

NIRv and GPP were moderate (in order of decreasing R^2): $\mathbf{NIRv^{PF}_{ECfootprint}}$ > $\mathbf{NIRv^{in\ situ}}$ > $\mathbf{NIRv^{PF}_{100m}}$ > $\mathbf{NIRv^{PF}_{NDVIsensor}}$, with R^2 values of 0.62, 0.58, 0.46, and 0.43, respectively. Overall, the linear relationships were stronger between $\mathbf{NIRvP^{PF}}$and GPP than between $\mathbf{NIRv^{PF}}$ and GPP (Figures 4.6 and 4.7).

The performance of $\mathbf{NIRvP^{PF}}$ in estimating GPP at each site individually was only clearly improved for one (US-Myb, Palustrine wetland) out of the five sites when the satellite footprint was matched to the $EC_{footprint}$ (Figure 4.7, Table A4.6). For other sites the performance of the $\mathbf{NIRvP^{PF}_{ECfootprint}}$ was slightly better (US-Bi1, Alfalfa; and US-Snf, Pasture) or comparable (US-Bi2, Corn; and US-Tw4, Freshwater wetland) than other footprint types. $\mathbf{NIRvP^{PF}_{ECfootprint}}$ showed a strong linear relationship with *in situ* GPP at the wetland sites, especially US-Myb (Palustrine wetland). For all footprint types, $\mathbf{NIRvP^{PF}}$ generally showed slightly stronger linear relationships with GPP than with $\mathbf{NIRvP^{in\ situ}}$ except for US-Bi2 (Corn). I observed the largest improvement of $\mathbf{NIRvP^{PF}}$ compared to $\mathbf{NIRvP^{in\ situ}}$ for site US-Bi1 (Alfalfa), where the linear regression between $\mathbf{NIRvP^{in\ situ}}$ and GPP had an R^2 value of 0.72, whereas the linear regression of $\mathbf{NIRvP^{PF}}$was > 0.78 for all footprint types (Table A4.6). $\mathbf{NIRv^{PF}_{ECfootprint}}$ also had higher R^2 values compared to $\mathbf{NIRv^{PF}_{100m}}$ (Figure 4.7; Table A4.6).

The slopes of linear regressions between $\mathbf{NIRv^{PF}}$ and $\mathbf{NIRvP^{PF}}$ and GPP showed large differences for the $NDVI_{sensor}$ and 100 m footprints but converged when Planet Fusion data was matched with the footprint type of $EC_{footprint}$ (Figure 4.6). More specifically, the variability in linear regression slopes of both NIRv and NIRvP with GPP showed the following ranking (in order of decreasing variability):

Planet Fusion NIRv (NIRvP) with different footprint types ($EC_{footprint}$ > 100m > $NDVI_{sensor}$) > $\mathbf{NIRv}^{in\ situ}$ ($\mathbf{NIRvP}^{in\ situ}$) (Figure 4.7). In the cropland sites, the linear regression slopes of $\mathbf{NIRv}^{in\ situ}$ and $\mathbf{NIRvP}^{in\ situ}$ with GPP were larger at US-Bi2 (Corn, a C4 plant) than at US-Bi1 (Alfalfa, a C3 plant). These trends were also observed in both $\mathbf{NIRv}^{PF}$ and $\mathbf{NIRvP}^{PF}$ for all footprint types (Figure 4.6; Table A4.6). The linear regression slopes of $\mathbf{NIRv}^{in\ situ}$ and $\mathbf{NIRvP}^{in\ situ}$ with GPP were generally larger in wetland sites than in cropland sites.

While overall NIRvP showed better GPP estimation performance than NIRv, there were notable differences between Planet Fusion and *in situ* – based results as well as individual sites vs. pooled data (Figures 4.6, 4.7, S4.3; Table A4.6). For the pooled data from all sites, the difference in R^2 values between NIRvP and NIRv-based GPP estimation showed a ranking in the following order: Planet Fusion NIRv (NIRvP) with different footprint types ($NDVI_{sensor}$-> 100m > $EC_{footprint}$) > $\mathbf{NIRv}^{in\ situ}$ ($\mathbf{NIRvP}^{in\ situ}$) with R^2 differences of 0.18, 0.19, 0.16, and 0.02, respectively (Table A4.6). For individual sites, *in situ* only showed clear improvement of NIRvP over NIRv for US-Myb (Palustrine wetland), while for other sites the performances were comparable (US-Snf; Pasture) or even slightly worse (US-Bi1, Alfalfa; US-Bi2, Corn; US-Tw4, Freshwater wetland) for NIRvP (Table A4.6). For Planet Fusion-based results, larger improvements of NIRvP over NIRv were observed, especially for sites US-Bi1 (Alfalfa) and US-Myb (Palustrine wetland) (Figure 4.7). However, for some sites, and especially for the 100 m fixed footprint type, NIRvP performed slightly worse than NIRv.

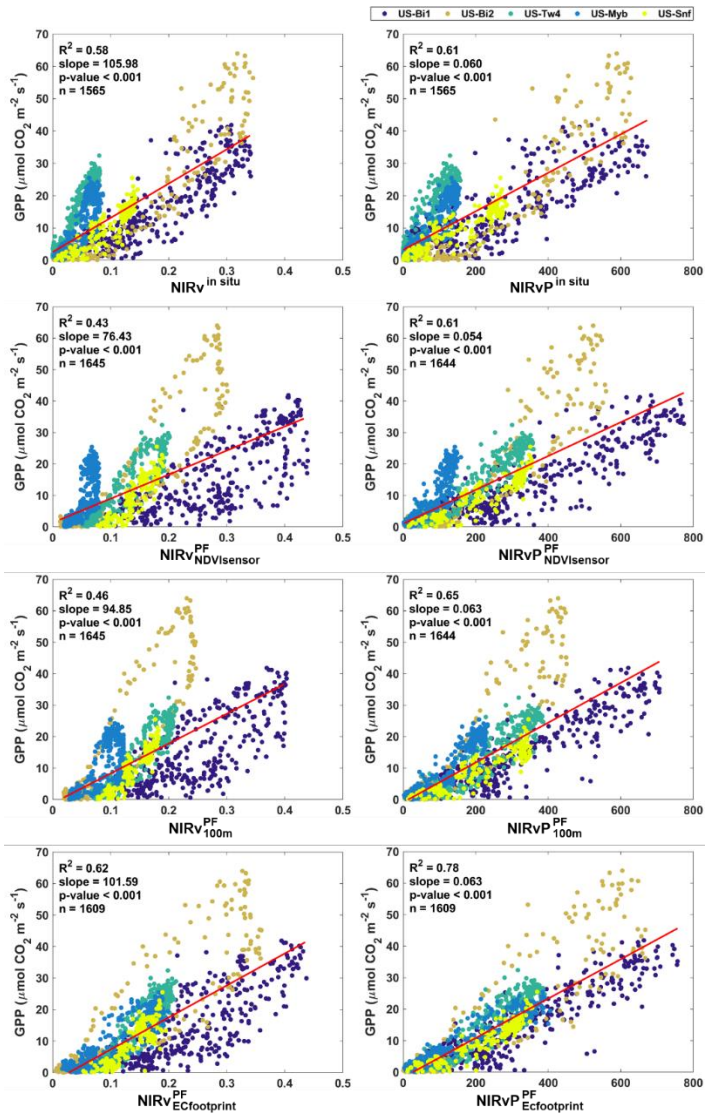

Figure 4.6 Comparison of NIRv and NIRvP measured *in situ* and derived from gap-filled Planet Fusion (PF) in different footprint types with GPP measured in all study sites (colored circles) around satellite overpassing time. $\mathbf{NIRv(NIRvP)^{PF}_{NDVIsensor}}$, $\mathbf{NIRv(NIRvP)^{PF}_{100m}}$, $\mathbf{NIRv(NIRvP)^{PF}_{ECfootprint}}$ denotes Planet Fusion -derived NIRv (NIRvP) around the local satellite overpassing time for footprint domains (i.e., $NDVI_{sensor}$, 100m, and $EC_{footprint}$). Red lines indicate linear regression model slopes for all sites. R^2 is the coefficient of determination, p-value indicates the significance of the linear regression, and n is the number of samples used in the linear regression model. NIRv is unitless and NIRvP is unit of $\mu mol\ m^{-2}\ s^{-1}$. Detailed site data are provided in (Table A4.6).

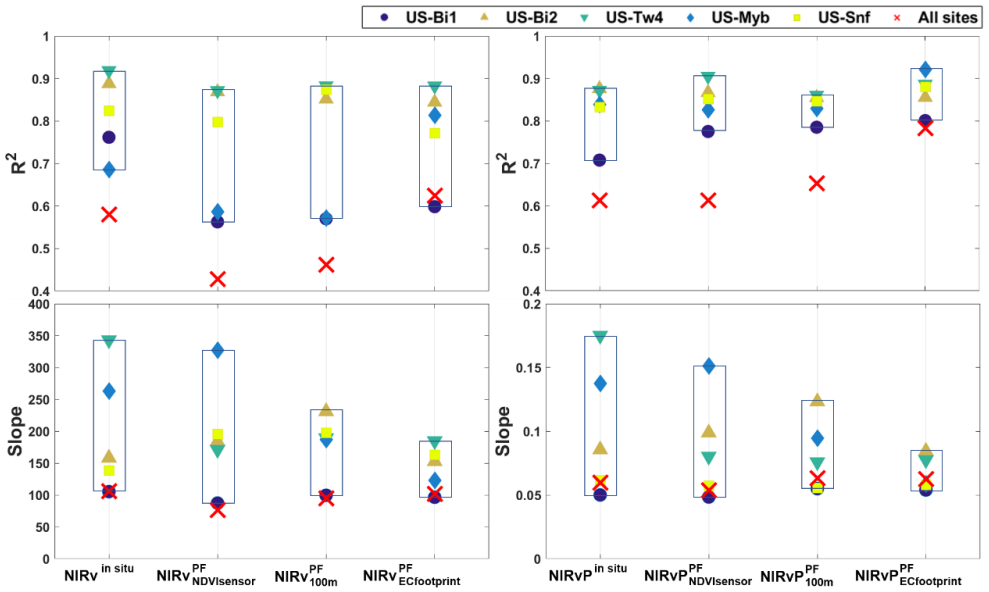

Figure 4.7 Comparison of NIRv and NIRvP measured *in situ* and derived from gap-filled Planet Fusion (PF) with GPP measured at each site and all sites pooled (colored symbols) around satellite passing time for all footprint types. $\mathbf{NIRv(NIRvP)^{PF}_{NDVIsensor}}$, $\mathbf{NIRv(NIRvP)^{PF}_{100m}}$, $\mathbf{NIRv(NIRvP)^{PF}_{ECfootprint,satellite}}$ denotes Planet Fusion-derived NIRv (NIRvP) around the local satellite overpassing time for footprint domains (i.e., $NDVI_{sensor}$, 100m, and $EC_{footprint}$). R^2 and linear regression slopes are shown for each site. Detailed site data are provided in (Table A4.6).

Trends in $\mathbf{NIRvP^{PF}_{ECfootprint}}$ and GPP over time were similar (Figure 4.8). Among Planet Fusion NIRvP data derived from different footprint types, $\mathbf{NIRvP^{PF}_{ECfootprint}}$ showed generally good performance in tracking the detrended GPP, especially over wetlands. For example, at site US-Myb (Palustrine wetland), $\mathbf{NIRvP^{PF}_{ECfootprint}}$ captured the sharp drops in GPP around day of the year 160, 260 and 280, whereas $\mathbf{NIRvP^{PF}_{NDVIsensor}}$ and $\mathbf{NIRvP^{PF}_{100m}}$ did not (Figure S4.3). $\mathbf{NIRvP^{PF}_{ECfootprint}}$ showed stronger linear relationships with GPP, compared with $\mathbf{NIRvP}^{in\ situ}$. Notably, the R^2 values of the relationship between detrended $\mathbf{NIRvP^{PF}_{ECfootprint}}$ and detrended GPP were greater than the R^2 values for $\mathbf{NIRvP}^{in\ situ}$, except for US-Bi2 (Corn).

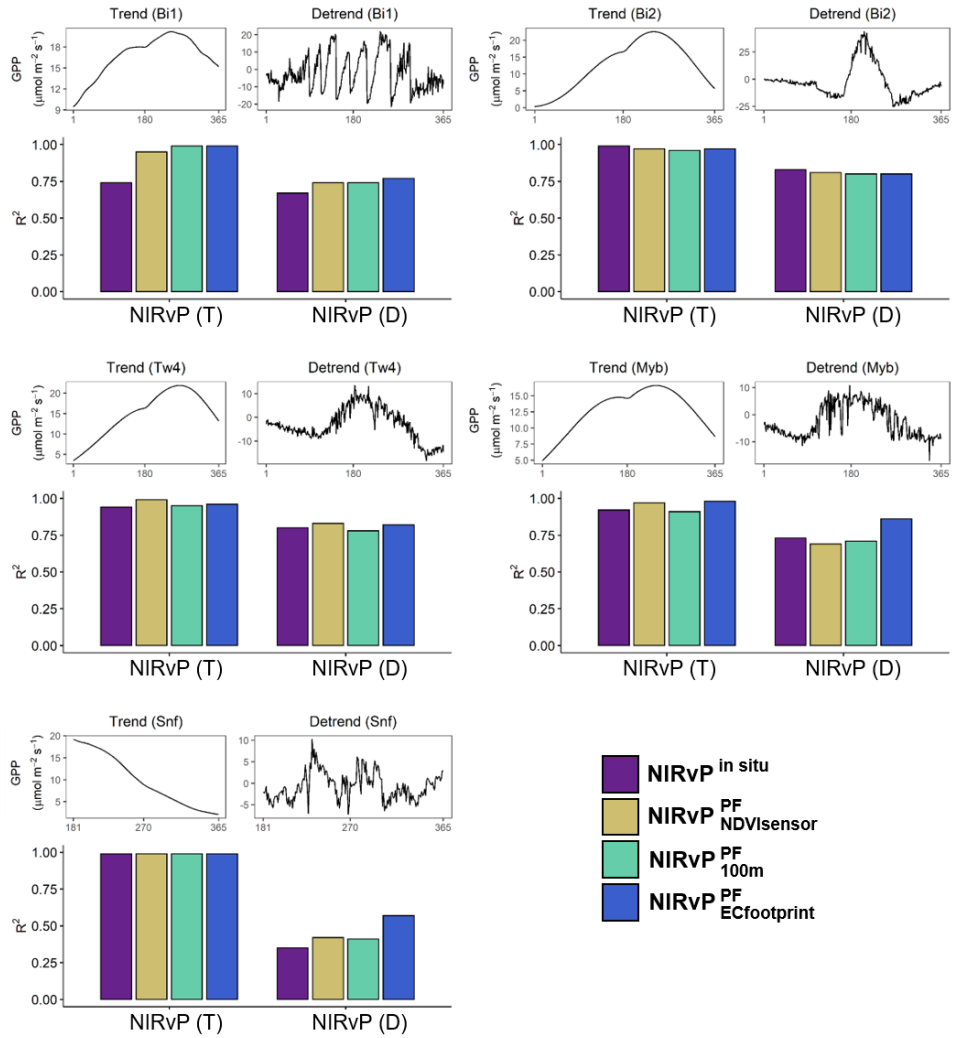

Figure 4.8 The GPP trend (T) and detrended (D) GPP at each site. Linear relationships of gap-filled Planet Fusion (PF) NIRvP and *in situ* NIRvP with T and D around the satellite passing time are also shown. $\mathbf{NIRvP^{PF}_{NDVIsensor}}$, $\mathbf{NIRvP^{PF}_{100m}}$, $\mathbf{NIRvP^{PF}_{ECfootprint}}$ denotes Planet Fusion -derived NIRvP around the local satellite overpassing time in different footprint type (i.e., $NDVI_{sensor}$, 100m, and $EC_{footprint}$). Detailed site data for the entire study period are shown in (Figure S4.3).

$NIRvP^{PF}_{ECfoorprint}$ more accurately estimated GPP around satellite overpassing time at the original spatial resolution (3 m), compared with footprint matching at the aggregated 30 m resolution (Figure 4.9). The performances of $\mathbf{NIRvP^{PF}_{ECfootprint}}$ in estimating GPP at different spatial resolutions were similar for croplands but differed

for wetland sites. For example, in the wetland sites (i.e., US−Tw4, Freshwater wetland; US−Myb, Palustrine wetland; and US−Snf, Pasture), $NIRvP^{PF}_{ECfootprint}$ (3 m) showed a slightly stronger linear relationship (R^2 = 0.89, 0.92, and 0.88, respectively) with GPP than did 30 m resampled $NIRvP^{PF}_{ECfootprint}$ (R^2 = 0.83, 0.90, and 0.85, respectively).

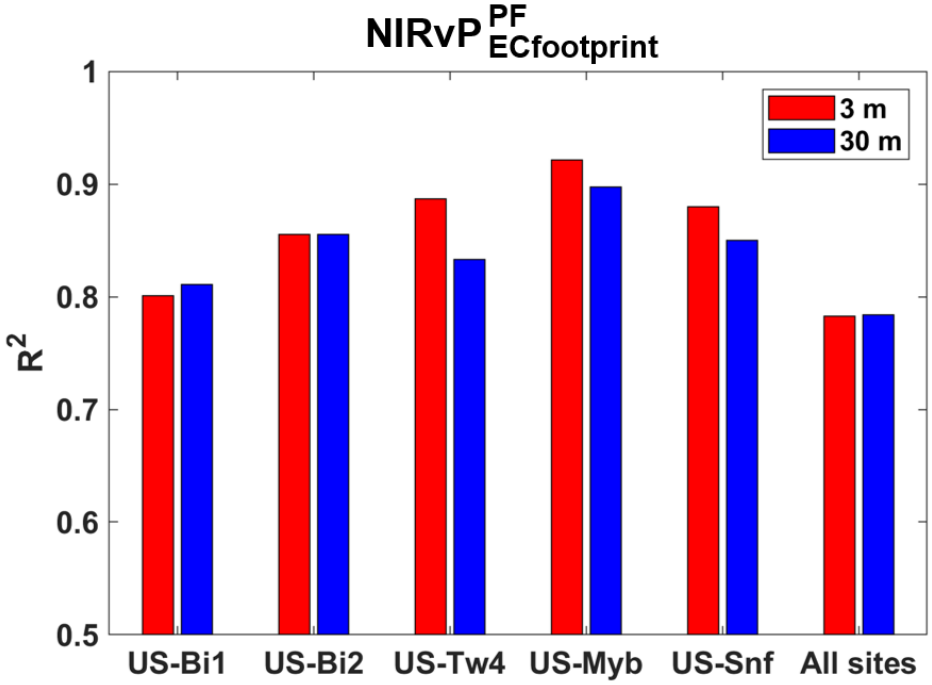

Figure 4.9 Evaluation of Planet Fusion (PF) derived NIRvP within eddy covariance (EC) footprint in different spatial resolution against GPP around satellite passing time. $NIRvP^{PF}_{ECfootprint}$ denotes Planet Fusion −derived NIRvP in daily eddy covariance footprints around the local satellite overpassing time. The linear relationships against GPP are shown. The detailed numbers are in (Table A4.6).

3.3 Daily GPP estimation from Planet Fusion −derived NIRvP

The overall performance of daily $NIRvP^{PF}_{ECfootprint}$ (R^2 = 0.80; RMSE = 2.08) in estimating daily GPP was considerably better than the overall performance of daily $NIRvP^{in\ situ}$ (R^2 = 0.67; RMSE = 2.68)

(Figure 4.10). The $\mathrm{NIRv}^{\mathrm{PF}}_{\mathrm{ECfootprint}} \times \mathrm{daily\ PAR}^{\mathrm{BESS}}$ product showed a stronger linear relationship and smaller RMSE (R^2 = 0.79; RMSE = 2.15) with daily GPP than the $\mathrm{NIRv}^{in\ situ} \times \mathrm{daily\ PAR}^{\mathrm{BESS}}$ product (R^2 = 0.62; RMSE = 2.88). Compared with $\mathrm{daily\ NIRvP}^{\mathrm{PF}}_{\mathrm{ECfootprint}}$, $\mathrm{NIRv}^{\mathrm{PF}}_{\mathrm{ECfootprint}} \times \mathrm{daily\ PAR}^{\mathrm{BESS}}$ showed similarly good performance for daily GPP estimation. The slopes (in parentheses) estimated by linear regression between NIRvP and daily GPP were: $\mathrm{daily\ NIRvP}^{\mathrm{PF}}_{\mathrm{ECfootprint}}$ (0.67–0.98) > $\mathrm{NIRv}^{\mathrm{PF}}_{\mathrm{ECfootprint}} \times \mathrm{daily\ PAR}^{\mathrm{BESS}}$ (0.69 – 1.01) > $\mathrm{daily\ NIRvP}^{in\ situ}$ (0.80 – 2.32) > $\mathrm{NIRv}^{in\ situ} \times \mathrm{daily\ PAR}^{\mathrm{BESS}}$ (0.68 – 2.35) (Table A7). Additionally, $\mathrm{NIRv}^{\mathrm{PF}}_{\mathrm{ECfootprint}} \times \mathrm{daily\ PAR}^{\mathrm{BESS}}$ followed well the changes of GPP with time (Figure 4.11).

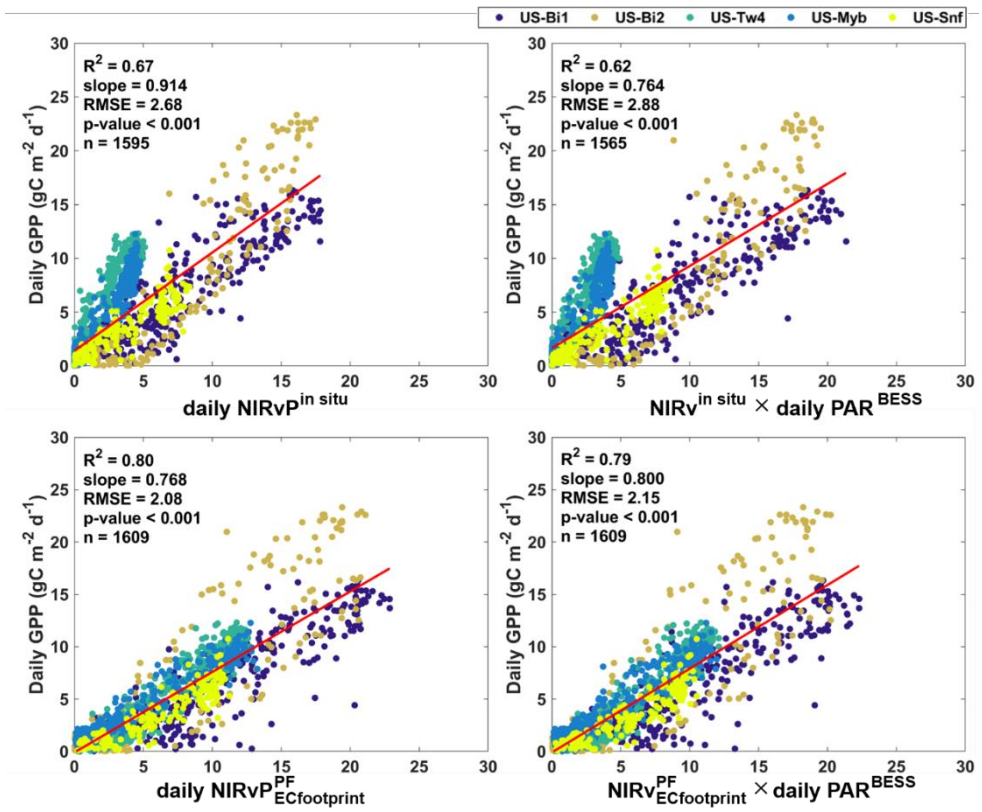

Figure 4.10 Linear relationships between *in situ*–measured and Planet Fusion (PF)–derived daily NIRvP and daily GPP at all sites (colored circles). **daily NIRvP$^{\text{in situ}}$** denotes the aggregated half–hourly *in situ* NIRvP; **NIRvP$^{\text{in situ}}$** denotes averaged *in situ* NIRvP around the local satellite overpassing time; **daily PAR$^{\text{BESS}}$** means daily summed PAR data retrieved from the satellite–based Breathing Earth System Simulator (BESS); **daily NIRvP$^{\text{PF}}_{\text{ECfootprint}}$** indicates temporally upscaled **NIRv$^{\text{PF}}_{\text{ECfootprint}}$**. Red line indicates the linear regression model slope of overall sites. R^2 is the coefficient of determination, p–value indicates the significance of the linear regression, and n is the number of samples used in the linear regression model. NIRvP is given in unit of mol m^{-2} d^{-1}. Detailed site data are provided in (Table A4.7).

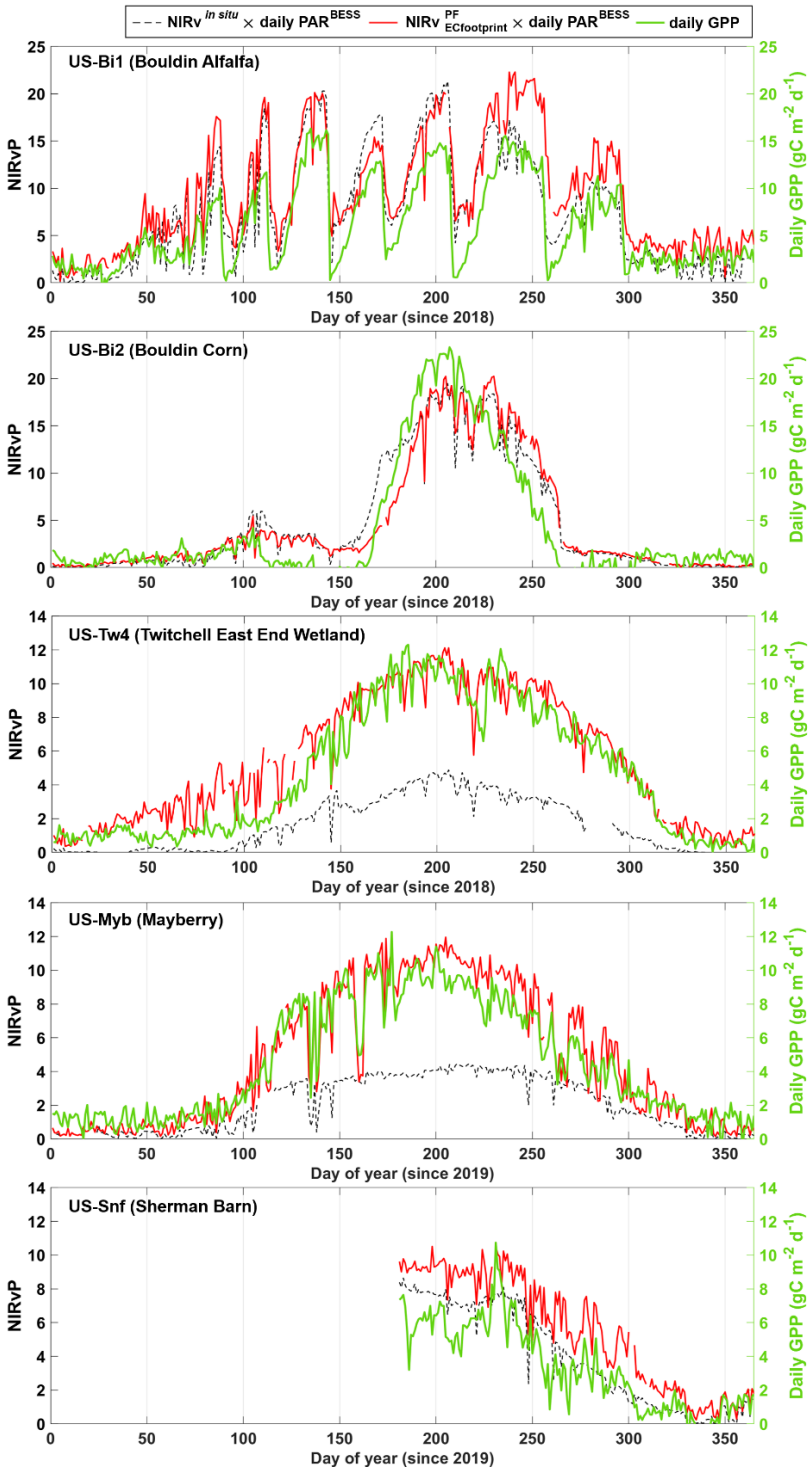

Figure 4.11 Seasonal variation of the product of NIRv from *in situ* and Planet Fusion (PF) in different footprint types and BESS daily PAR (left axis) and that of daily GPP (right axis). NIRvP is given in unit of mol m^{-2} d^{-1}.

4. Discussion

Overall, I found that matching Planet Fusion NIRvP to the flux tower footprint considerably improved the agreement with flux tower–based GPP across sites compared to using a fixed footprint (100 m, a hectare area around tower; $NDVI_{sensor}$, the footprint of *in situ* NDVI sensor) even when compared to the *in situ* NIRvP observations (Figure 4.6 and 4.7). The effects of matching the flux tower footprint on the regression slope between NIRvP and GPP was largest for the two wetland sites and a corn site (Figure 4.7). For daily GPP estimation from Planet Fusion data, the different approaches showed comparable performances (Figure 4.10). NIRvP considerably outperformed NIRv for GPP estimation around satellite overpass time, especially when pooling the data from all sites and using Planet Fusion NIRvP. A more detailed discussion on the different aspects is presented in the subsections below.

4.1 Flux tower footprint matching and effects of spatial and temporal resolution on GPP estimation

The high spatial resolution of Planet Fusion NIRvP ($\mathbf{NIRvP^{PF}}$) (3 m) allowed us to match the footprints of *in situ* NDVI sensors and eddy covariance systems with Planet Fusion pixels, which led to considerable improvement in the agreement between $\mathbf{NIRvP^{PF}}$ and flux tower GPP compared to either a fixed footprint (100 m by 100m) or the relatively small area covered by *in situ* NDVI sensors (NDVIsensor footprint)(Figure 4.3, 4.6, and 4.7). In fact, the performance of Planet Fusion NIRvP in daily flux tower footprints ($\mathbf{NIRvP^{PF}_{ECfootprint}}$) was even better than that of *in situ* sensors with bi-hemispheric view, which did not fully cover the EC footprint (Figure 4.3). This is a remarkable finding as it implies that the uncertainties

associated with satellite observations of NIRvP are smaller than the impacts of the footprint mismatch between *in situ* optical sensors and the flux tower footprint.

An important aspect of our study was to characterize how the footprint mismatch affected the NIRvP–GPP relationships and to identify the factors explaining such patterns. I found that the effects of footprint mismatch had relatively small impacts on the NIRvP–GPP correlation for individual sites but large impacts on the data combined from all sites (Figure 4.6 and 4.7). This was due to inconsistent NIRvP–GPP regression slopes when the flux tower footprint was not matched (Figure 4.7). These results indicate that while the temporal GPP dynamics are relatively consistent in different parts of the ecosystems, the canopy structure factors such as leaf area index, leaf angles and clumping to which NIRvP is sensitive (Dechant et al., 2022; Dechant et al., 2020) can vary considerably within the flux tower footprints. Freshwater wetland (US–Tw4) and Palustrine wetland (US–Myb) showed the highest sensitivity of regression slopes to the choice of footprint schemes (Figure 4.6 and 4.10). Although one might first suspect the impact of the water fraction or the spatial patterns of the water (Matthes et al., 2014) rather than vegetation canopy structure in the footprint of optical sensors to explain the different slopes in wetland ecosystems, NIRvP is largely insensitive to water background as both the NDVI factor and NIR reflectance have low values for water (Chen et al., 2018; Weiss and Crabtree, 2011). Therefore, the most likely explanation for the large sensitivity of wetland sites to the footprint type is the spatial heterogeneity in canopy structure. Apart from insufficient spatial coverage (Gamon, 2015), observations from *in situ* spectral sensors can also be particularly biased as they typically include the tower

structure and its surroundings which are not representative of the flux tower footprint as vegetation near the tower is cleared for the safety of the tower structure. The high consistency between NIRvP and GPP patterns at each site during the study period (Figure 4.11 and S4.3) is likely due to the strong impact of environmental drivers such as PAR, temperature and humidity.

I found that the NIRvP–GPP relationships indeed improved by footprint matching rather than other factors that could affect the relationship. As NIRvP is only a proxy for GPP but not a direct observation, the comparison of satellite NIRvP with ground GPP is not a direct ground validation and might be affected by other limitations of NIRvP to estimate GPP, in addition to other uncertainties related to satellite vs. ground observations. Therefore, I used two different ways to exclude such uncertainties as alternative factors explaining our findings of improved NIRvP–GPP relationships when matching Planet Fusion with flux tower footprints. First, I compared entirely *in situ*–based NIRvP–GPP relationships with relationships where the Planet Fusion area matched the footprint of the *in situ* NDVI sensor. As these results showed rather similar patterns in slope differences between sites (Figure 6 and 7), the main factor for different slopes indeed seems to be the footprint size and site location. Second, I also conducted a direct ground–validation analysis for NIRv and NIRvP and found strong agreement between Planet Fusion and *in situ* NIRv and NIRvP (Figure 4 and 5). This further confirms that the Planet Fusion –based satellite products are reliable and that the patterns in the results of NIRvP–GPP relationships for different footprints are indeed due to the area covered rather than other sources of uncertainty. Although I found the footprint mismatch to be the dominant factor explaining NIRvP–

GPP slope differences between sites, the photosynthetic pathway of the vegetation also needs to be taken into account. Among the cropland sites, the slope of Planet Fusion NIRvP against GPP in C4 plants (corn in US-Bi2) was generally higher than that in C3 plants (alfalfa in US-Bi1) (Figure 4.6). This higher slopes of C4 compared to C3 plants is consistent with previous studies although I found a smaller difference (Badgley et al., 2019; Baldocchi et al., 2020; Dechant et al., 2022). I found that the gap-filling of Planet Fusion data had the effect of increasing the spread in NIRvP-GPP regression slopes (Figure 4.5). This effect, however, was small and mostly due to a single site (US-Myb; Palustrine wetland) and also cannot explain the differences between different footprint types as the gap-filled data was used for all of them.

The high spatial resolution of Planet Fusion improved the performance of NIRvP-based GPP estimation more compared to the high temporal resolution. To quantify the effects of spatial and temporal resolution of satellite imagery on the NIRvP-based GPP estimation results, I conducted further analyses. First, I evaluated if the footprint matching could still be effective at the coarser spatial resolution of 30 m instead of 3 m. Although the performance of 30 m data was still relatively robust, better performance (R^2 increase ~ 0.06) was found for 3 m at some of the sites, especially at the wetland and corn sites (Figure 4.9; Table A4.6), where the water surface extent can change at scales below 30 m (Halabisky et al., 2016). In the direct ground validation for NIRv and NIRvP, I found that the coarse 500 m MODIS pixels had poor performance with large slope differences between the sites (Figure 4 and 5) due to low proportion of footprint area within a pixel (McCombs et al., 2019), while the finer 30 m HLS and 3 m Planet Fusion pixels showed robust

performance. Nevertheless, I found substantial land surface heterogeneity even within the 30 m satellite pixels (Figure A4.8) indicating the advantage of the Planet Fusion high-resolution imagery which cannot be replaced by fusion products based on MODIS-HLS without compromising the performance (Kong et al., 2021). Second, I evaluated the impact of temporal resolution by comparing the results for daily matching of the EC footprint with that of matching the annual footprint (Figure A4.9). I found similar performance in the two cases. Although there is daily variation in the footprints at each site, the annual footprints are good representatives of the area measured by the flux tower because of a strongly dominant wind direction related to the typical meteorological conditions in this area on an annual time scale (Figure A4.3; Figure S4.8). These findings are, therefore, specific to the sites I used and bigger differences between annual and daily footprint matching are expected for other sites with more variable wind directions (Kim et al., 2006).

The near-daily revisit frequency of CubeSats (Roy et al., 2021) allowed us to track canopy dynamics in detail. For the study period in each site, overall, CubeSats provided 49 – 56% of daily data when gap-filled data is removed, which is a higher daily retrieval rate compared to HLS (22 – 28%) (Figure 4.4; Table A4.5). The near-daily Planet Fusion acquisition frequency enabled the detection of surface changes like mowing events (Figure S4.3 and S4.4) (Kong et al., 2021). Nonetheless, cloud-induced data gaps can still present a significant obstacle for uninterrupted land surface monitoring. Over the study sites, the Planet Fusion -based gap-filling process enabled daily tracking of photosynthesis (Figure 4.5; Table A4.5). Even though the data-gaps were not negligible throughout the study period

(Figure A4.8), Planet Fusion data were in general successfully gap-filled (Figure 4.4) in part due to relatively short temporal gaps (Kong et al., 2021; Luo et al., 2018). While the gap-filling had considerable impacts on NIRv, the performance of Planet Fusion NIRvP compared to *in situ* NIRvP was robust even for gap-filled data (Figure 4.4 and 4.5). Daily gap-filled $\mathbf{NIRvP}^{\mathbf{PF}}_{\mathbf{ECfootprint}}$ responded to GPP drops caused by drastic surface changes (e.g., mowing) (Figure 4.8; Figure S4.3) which agrees with previous findings that Planet Fusion -based evapotranspiration maps are able to capture evaporation fluxes on a day-to-day basis (Aragon et al., 2021). Further improvements in the capacity to track diurnal canopy dynamics may involve spatio-temporal image fusion between CubeSat and geostationary satellites that scan the same area in every 5-15 minutes (Khan et al., 2021) or integration of ECOSTRESS data that measure thermal infrared with 70 m resolution every 1-5 days (Fisher et al., 2020; Li et al., 2021).

4.2 Roles of radiation component in GPP mapping

At the time of satellite overpass, I found $\mathbf{NIRvP}^{\mathbf{PF}}$ estimated GPP better than $\mathbf{NIRv}^{\mathbf{PF}}$ when pooling data from all sites and also for most sites individually (Figure 4.6, 4.7 and 4.8). When NIRv was first proposed, it successfully explained the variation of GPP at the monthly time scale (Badgley et al., 2017). As the variations of daily NIRv and, above all, PAR values are mostly averaged out at monthly time scales, NIRv alone can estimate monthly GPP with reasonable performance. However, NIRv alone raises an issue for GPP estimation at the time of satellite overpass and daily scales as PAR plays an important role (Dechant et al., 2022; Dechant et al., 2020). Although PAR variations are most important for estimating diurnal

variations of GPP and NIRvP, PAR still plays an important role at the time of satellite overpass due to considerable seasonal PAR variations (Figure A4.2 and S4.3). In fact, when examining our results closely, a stronger tendency towards non-linear relationships to GPP can be observed for NIRv compared to NIRvP when considering sites individually (Figure 4.7). Somewhat similar non-linear effects have also been reported before for statistical GPP estimation from reflectance measured by the hyperspectral sensor without including PAR information (Dechant et al., 2019). However, another potential explanation for the non-linear effects at rather low values could be the non-zero NIRv values for senescent or dead vegetation outside of the main growing season when GPP is essentially zero (Figure S4.3). As PAR is low during those times, NIRvP has a somewhat dampened non-linearity compared to NIRv. Assuming that background effects are indeed partly causing the non-linearities, using soil-adjusted NIRv may further improve the results (Jiang et al., 2021). Overall, the better performance of $\mathbf{NIRvP}_{\mathbf{ECfootprint}}^{\mathbf{PF}}$ for estimating GPP (Figure 4.6; Table A4.6) is consistent with both a mechanistic understanding of GPP drivers and the previous literature on the matter.

While some aspects of the differences in performance of NIRv compared to NIRvP for GPP estimation (Figure 4.6 and 4.7) might appear counter-intuitive at first sight, a closer examination of the results can explain those patterns. In particular, the difference between NIRv and NIRvP for GPP estimation was considerably smaller for *in situ* data than for Planet Fusion data and for the latter it was considerably larger for pooled data from all sites than for individual sites. Furthermore, the slope consistency and R^2 values between sites showed similar relative sensitivities to footprints for

$\mathbf{NIRv^{PF}}$ and for $\mathbf{NIRvP^{PF}}$ although the R^2 values differed considerably in absolute values. All these results can be understood by taking into account the effects of gap−filling on $\mathbf{NIRv^{PF}}$, as the gap−filling led to decrease in agreement with *in situ* NIRv ($\mathbf{NIRv^{in\ situ}}$) (Figure A4.8) but this larger disagreement essentially disappeared for NIRvP (Figure 4.4 and 4.5). This compensatory effect of PAR may also suggest a critical control of PAR on regulating seasonal GPP variations at the time of satellite overpass. It should be noted that the effect of gap−filling on the performance of $\mathbf{NIRv^{PF}}$ was mostly reflected in the correlation to GPP at individual sites rather than in the slope consistency between sites (Figure 4.4 and 4.5).

Daily PAR maps enable $\mathbf{NIRv^{PF}}$ maps to conduct spatial upscaling of daily GPP estimation from point eddy covariance sites to landscape scale. Currently, estimates of GPP at eddy covariance sites cover only a small area of the terrestrial surface, with limited numbers of sites that are strongly biased geographically (Ciais et al., 2014; Schimel et al., 2015). I found that $\mathbf{daily\ NIRvP^{PF}_{ECfootprint}}$, which was temporally upscaled from satellite overpassing time, was strongly correlated to daily GPP (Figure 4.10) as GPP at a specific time of the day with a cosine correction generally shows a strong linear relationship with daily GPP (Ryu et al., 2012; Zhang et al., 2018). In other words, the relationship between $\mathbf{NIRvP^{PF}_{ECfootprint}}$ and GPP around the overpass time resulted in good performance of daily $\mathbf{NIRvP^{PF}_{ECfootprint}}$ in estimating daily GPP (Figure 4.10). Furthermore, NIRvP includes information regarding canopy structure and the amount of incoming radiation absorbed and scattered by vegetation (Baldocchi et al., 2020; Dechant et al., 2022; Dechant et al., 2020). Assuming that canopy structure changes are small within a day, the

multiplication of daily PAR by Planet Fusion–derived NIRv will robustly estimate daily GPP. Consequently, $\mathbf{NIRv}^{\mathbf{PF}}_{\mathbf{ECfootprint}} \times \mathbf{daily\ PAR}^{\mathbf{BESS}}$ performed similarly to $\mathbf{daily\ NIRvP}^{\mathbf{PF}}_{\mathbf{ECfootprint}}$ in estimating daily GPP (Figure 4.10 and 4.11). Accordingly, Planet Fusion –derived NIRv combined with daily PAR maps enables us to generate daily GPP maps with a high degree of fidelity (Figure 4.10), which is consistent with the finding of previous studies at different scales (Jiang et al., 2021).

4.3 Limitations and perspectives

Our findings indicate that further tests of the slopes of the relationships between NIRvP and GPP are required. The study period for each site varied from 6 months to 1 year (Table 4.1), which may be sufficient for testing seasonal variation; however, it is insufficient for testing whether these slopes are stable over long periods. Several studies have reported strong correlations between NIRvP and GPP (Baldocchi et al., 2020; Dechant et al., 2022; Dechant et al., 2020), but the consistencies of their slopes over multiple years, which could include severe stress such as drought, have not been evaluated. Our study sites (cropland and wetlands) are well–known for low water stress. While Baldocchi et al. (2020) reported a strong and rather consistent relationship between NIRvP and GPP at an annual grassland site when pooling data from twelve years, the stability of slopes was not investigated. Also, the longer–term robustness of the relationships between NIRvP and GPP could differ between ecosystems. The accumulation of Planet Fusion data over longer periods will allow us to capture interannual variation in canopy GPP and test if the promising findings of Baldocchi et al. (2020) and

Badgley et al. (2019) also hold at finer spatio-temporal scales across ecosystems.

Limitations are expected in the performance of NIRvP to capture shorter-term responses of GPP to vegetation stress as NIRvP is entirely based on canopy structure and radiation information and does not include physiological vegetation signals. In particular, NIRv closely approximates the product of the fraction of absorbed PAR (fPAR) times the fraction of photons that escape from the canopy (fesc) (Zeng et al., 2019). Therefore, NIRvP well captures APAR, the product of fPAR and PAR, which is a strong driver of GPP. Although there is convincing evidence that fesc can capture seasonal variations in light use efficiency (LUE) in crops in the absence of strong environmental stress (Dechant et al., 2020; Liu et al., 2020), fesc might not capture the faster physiological responses at the onset of droughts as fesc is driven by canopy structure variables such as leaf area index, clumping and leaf inclination (Badgley et al., 2017; Qiao et al., 2019; Zeng et al., 2019), which typically respond more slowly than leaf physiology. Therefore, remote sensing variables that carry physiological signals related to LUE such as the photochemical reflectance index (PRI) and physiological emission yield of sun-induced chlorophyll fluorescence (Φ_F) should be considered to refine NIRvP-based estimates of GPP in situations of strong environmental stress (Dechant et al., 2022; Kimm et al., 2021; Wang et al., 2020c). While SIF contains both the structural information of NIRvP and the physiological information of Φ_F, the variations of Φ_F tend to be so small that separating them from the structural component with the help of NIRvP might be necessary to use this information for improved GPP estimation (Dechant et al., 2022).

Uncertainties remain in the satellite products and *in situ*

measurements. Because the radiometric accuracy of Planet Fusion data is linked to that of HLS (in this study) (PlanetFusionTeam, 2021), the bias of HLS NIRv ($\mathbf{NIRv}^{\mathbf{HLS}}$) against $\mathbf{NIRv}^{in\ situ}$ might lead to the bias of Planet Fusion NIRv in the footprint of *in situ* NDVI sensor ($\mathbf{NIRv}^{\mathbf{PF}}_{\mathbf{NDVIsensor}}$) against $\mathbf{NIRv}^{in\ situ}$ as (Figure 4.4). In addition, the absolute geolocation accuracy of the PlanetScope CubeSat data is less than 10 m RMSE (PlanetFusionTeam, 2021). Therefore, the discrepancy between $\mathbf{NIRv}^{\mathbf{PF}}_{\mathbf{NDVIsensor}}$ and $\mathbf{NIRv}^{in\ situ}$ over US-Bi1 (Alfalfa), which was similar to the range of Planet Fusion NIRv in HLS pixel coverage that includes $NDVI_{sensor}$ ($\mathbf{NIRv}^{\mathbf{PF}}_{\mathbf{inHLS}}$) (Figure A4.8), could be partly explained by geolocation uncertainties. Apart from the geolocation accuracy of the satellite imagery, the location of *in situ* spectral sensors can also contribute to biases in our results (Figure S4.1). Regarding the temporal patterns, Planet Fusion data will be associated with larger uncertainties during more extended gap periods (Figure A4.8; Figure 4.4). In those periods, NIRvP tracked GPP better than NIRv did, which could be explained by the role of day-to-day variations of PAR in predicting GPP. Moreover, the study sites are mostly cloud-free during the growing season, which is an ideal case, other sites might have broken clouds with shadows. In that case, the spatial mismatch between satellite-derived PAR and NIRv might degrade the performance of NIRvP-based GPP estimation as PAR with coarse spatial resolution cannot provide the radiation information separately between cloudy and cloud-free areas. In future works on cloudy areas, PAR derived from geostationary satellites with a high spatial resolution (Zhang et al., 2021) could be an option although the spatial resolution is still much coarser than the Planet Fusion imagery. Regarding *in situ* measurements, continuous eddy covariance

measurements can be relatively free from outliers compared to snapshot satellite imagery but sampling errors can also lead to outliers (Figure 4.6, Figure S4.4) even after integrating samples at 20 Hz to 30−min data (Moffat et al., 2007; Richardson et al., 2006). At a daily time scale, uncertainty (one standard deviation) in tower−derived GPP is typically assumed to be 15–20% of the measurements (Falge et al., 2002; Hagen et al., 2006; Richardson et al., 2006). Moreover, the assumptions made during the partitioning of GPP from NEE could induce uncertainty (Reichstein et al., 2005). Theoretically, both PAR and GPP should be zero in nighttime but gap−filled GPP have both negative and positive values in the nighttime due to an unideal temperature function of nighttime NEE. Therefore, the daily (0000hh−2400hh) GPP values are larger than daytime (0800hh−1800hh) GPP (Figure S4.9). Since I targeted to estimate daily GPP, which is needed for annual accumulated GPP, NIRvP–daily GPP relationship will be biased when I force nighttime GPP to 0 or exclude nighttime GPP in daily GPP (Figure S4.9). In the case of US−Snf (Pasture), the peak growing season over US−Snf (Pasture) was around December to June but the data were used from June to December in this study (Table 4.1). Hence, when vegetations are less active, the presence of cattle in US−Snf (Pasture), which can affect carbon dioxide fluxes (Baldocchi et al., 2012; Detto et al., 2010), might influence the relationship between NIRvP and GPP. Regarding footprint matching between Planet Fusion NIRvP and GPP, I weighted Planet Fusion pixels within the flux footprints based on the contour lines rather than the spatially fully explicit footprint contributions per pixel. Therefore, I also encourage future studies to develop pixel−based footprint model for calculating the footprint contribution per pixel.

Matching the footprint between Planet Fusion–derived NIRvP and GPP measurements enables us to use the full potential of flux tower data for spatial upscaling. Previous studies have already pointed out the importance of the spatial heterogeneity within flux tower footprints as the primary source of uncertainty in spatial upscaling (Giannico et al., 2018; Ran et al., 2016) and the role of CubeSat data in a robust spatial upscaling (Ryu et al., 2019). As Planet Fusion NIRvP could be successfully matched to the flux tower footprint (Figure 4.2; Appendix 4.2) despite frequent mowing and water extent changes (Figure 4.7), it could, in principle, also be used as a new tool for characterizing the heterogeneity of the eddy covariance footprints of all FLUXNET sites. The important difference to previous approaches relying on NDVI or other greenness indicators (e.g. Chen et al. (2011a), Chen et al. (2012), Chu et al. (2021)) would be to use NIRv as proxy for GPP, assuming sufficiently constant PAR in the selected area. To characterize the spatial heterogeneity, one could use semi–variogram (Kim et al., 2006), which is a suitable geostatistical method for analyzing spatial patterns. Such an analysis could well lead to unexpected results as sites that were previously characterized as homogeneous landscapes (e.g., cropland) may show considerable spatial heterogeneities (Figure A4.8). Apart from the footprint characterization that might also be of general interest to the eddy covariance community, Planet Fusion NIRvP will allow us to also include sites with heterogeneous footprints and landcover for spatial upscaling, which have not previously been feasible as the traditional satellite products with coarser spatio– temporal resolution had to rely on a selection of homogeneous sites to avoid biased results (Chen et al., 2011a; Ran et al., 2016). Although the footprint matching also improved temporal correlation of NIRvP against GPP for each

site (Figure 4.8), it was not as much as the convergence of slopes across the sites (Figure 4.7). NIRvP-based GPP estimation varied within the sites depending on the vegetation types and canopy structures but the slope of NIRvP-based daily GPP against *in situ* GPP over the study period were similar (Figure 4.10) because climate factors were the dominant drivers. Nevertheless, variations of NIRvP-GPP regression slopes could appear in very dense forest, ecosystems with high species diversity, and vertically heterogeneous canopies (Ishii et al., 2004), which were not tested in this study. In particular, evergreen needleleaf trees stay green during winter although their photosynthesis is nearly nil, which can lead to seasonally changing slopes between NIRvP and GPP (Kim et al., 2021).

Our results highlight the potential of CubeSat-based imagery for daily canopy GPP estimation. Previous studies have applied CubeSat datasets to monitor phenology, leaf area index, NDVI, and evapotranspiration (Aragon et al., 2018; Aragon et al., 2021; Houborg and McCabe, 2018b; Hwang et al., 2020; Kimm et al., 2020). The results of our study suggest that CubeSat imagery can be used to obtain daily canopy photosynthesis data at fine spatial and temporal resolution, thus overcoming limitations inherent in using only observations from individual sun-synchronous satellites such as MODIS and Landsat. Moreover, potential improvements of Planet Fusion -derived NIRv for NIRvP mapping have already been suggested (Jiang et al., 2021). In particular, Jiang et al. (2021) and Zeng et al. (2019) suggested methods to account for the non-zero NIRv values for bare soil or dead vegetation, which could lead to improvements in GPP estimation especially outside the main growing season. However, these approaches need additional information at

each site and only can predict GPP after the current season unless assumptions are made based on previous years' data. Further studies should evaluate the performance of Planet Fusion NIRvP for an even broader range of ecosystem types in various geographical locations and physiological stress conditions including drought and flood. Incorporation of inexpensive spectral sensors into flux towers that can monitor NIRv (Garrity et al., 2010; Kim et al., 2019; Ryu et al., 2010) and using existing sensor networks to increase ground observation of NIRv across the globe (Carrer et al., 2021) will be a useful strategy for evaluating and improving CubeSat-based fine-resolution GPP mapping.

5. Conclusion

In this study, I evaluated the performance of satellite-derived NIRvP as a proxy for GPP by comparing it with *in situ* GPP from a flux tower network over a heterogeneous landscape consisting of mixed wetlands and croplands. I found that the best agreement between flux tower GPP and NIRvP calculated from the Planet Fusion-based product was achieved when matching the Planet Fusion imagery to the tower flux footprints. In fact, the agreement of Planet Fusion imagery matched to the flux tower footprint was even considerably better than the agreement between *in situ* NIRvP and tower GPP. The improvement for GPP estimation due to the flux tower footprint matching was evidenced by the higher across-site consistency in linear regression slopes between Planet Fusion NIRvP and GPP compared to either fixed footprint Planet Fusion NIRvP or *in situ* NIRvP. This indicates a large impact of the mismatch between flux tower footprint and the area covered by optical sensors due to spatial heterogeneity within the temporally varying flux tower footprint. I found the largest effects of such mismatches in wetland sites that have a temporally varying fraction of vegetation in a given area. The performance of Planet Fusion-based NIRvP was robust across sites and times in the growing season both for GPP estimation at the time of satellite overpass and for daily summed values. Accordingly, Planet Fusion NIRvP serves as a viable metric for creating daily, high spatial resolution GPP maps at the landscape scale which could prove very useful for precision agriculture or the monitoring of heterogeneous and dynamic natural ecosystems such as wetlands. I encourage future efforts to test the proposed approach in a wide variety of ecosystems during water-limited or light saturation periods. Overall, our results demonstrated significant

advantages of the high spatio-temporal resolution Planet Fusion products for daily canopy GPP estimation and for upscaling flux data for model validation and parameterization. More generally, our findings indicate the large potential of sensor data fusion for high fidelity vegetation monitoring at unprecedented spatial and temporal resolutions.

Appendix

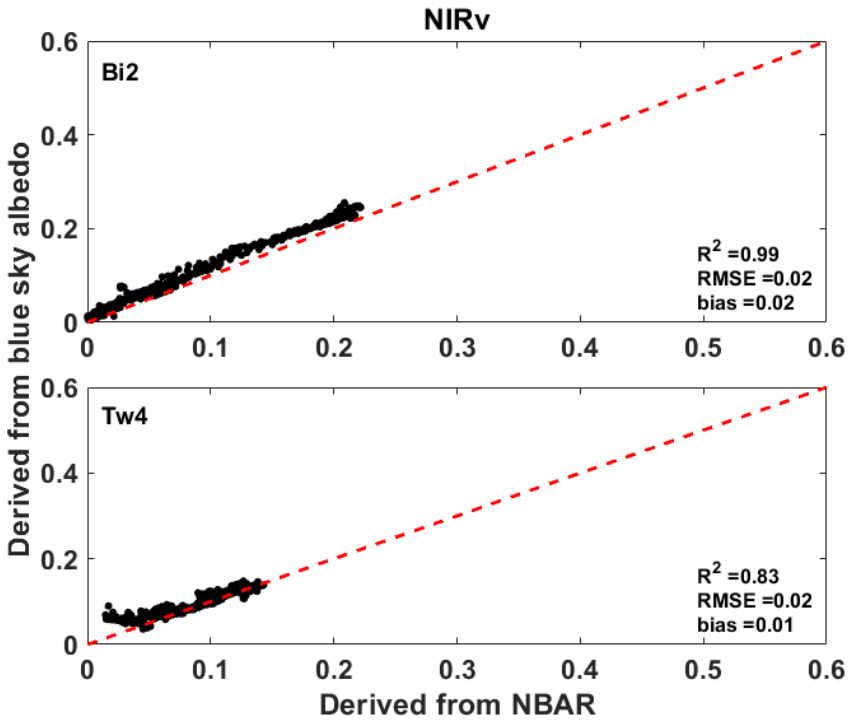

Figure A4.1 Evaluation of view geometry effects on *in situ* near−infrared radiation from vegetation (NIRv) from 2018 to 2019. Using MCD43A1 bidirectional reflectance distribution function parameters, I converted *in situ* bi−hemispheric reflectance into blue sky albedo at 1030hh (local time UTC−8) and compared it to a nadir bidirectional reflectance distribution function−adjusted reflectance (NBAR) product (MCD43A4).

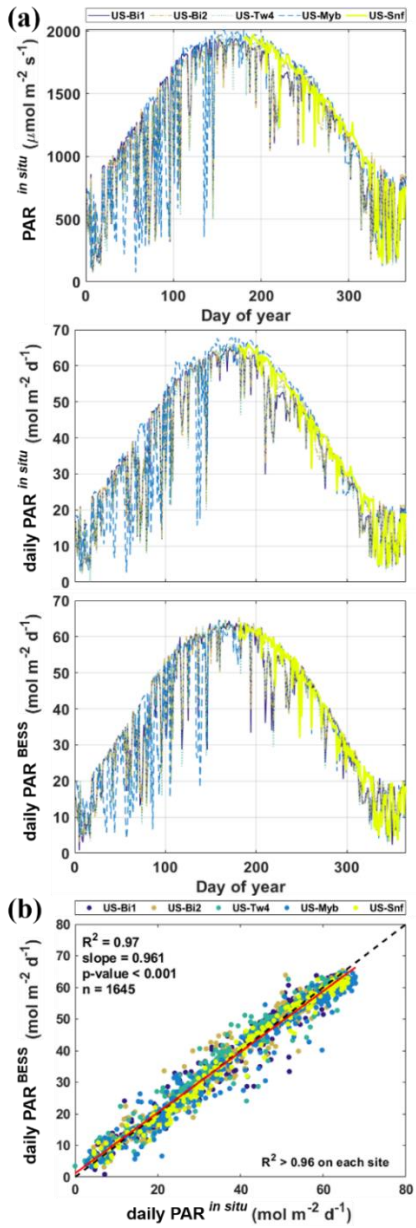

Figure A4.2 Evaluation of photosynthetically active radiation (PAR) data in this study. (a) Seasonal variation in PAR throughout 2018 at three sites (US−Bi1, Alfalfa; US−Bi2, Corn; and US−Tw4, Freshwater wetland) and 2019 in two sites (US−Myb, Palustrine wetland; and US−Snf, Pasture), including instantaneous *in situ* PAR at satellite passing time ($\mathbf{PAR}^{\mathbf{in\ situ}}_{\mathbf{satellite}}$), *in situ* daily PAR ($\mathbf{PAR}^{\mathbf{in\ situ}}_{\mathbf{daily}}$), and BESS daily PAR ($\mathbf{PAR}^{\mathbf{BESS}}_{\mathbf{daily}}$). (b) The relationship between BESS daily PAR and *in situ* daily PAR. Dashed black line is a 1:1 line (y = x). Red lines indicate the slopes of the linear regression models for each site. R^2 is the coefficient of determination, p−value indicates the significance of the linear regression, and n is the number of samples used in the linear regression model. For the US−Snf site, the daily PAR value was approximately 89% lower than the mean of the other sites throughout 2019; therefore, I applied a correction factor of 1.14 to all US−Snf PAR data.

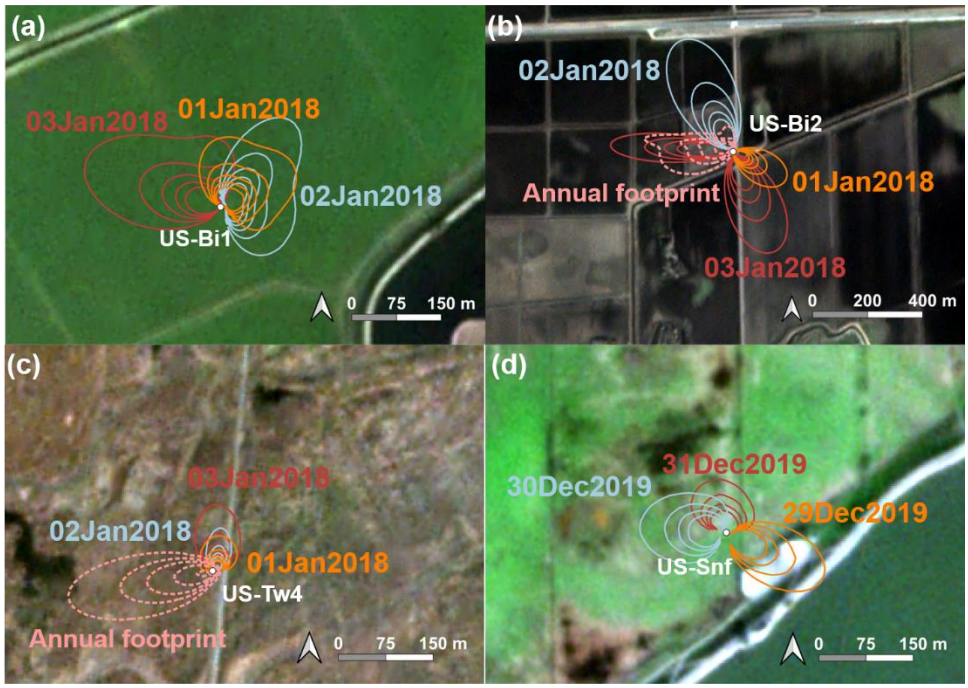

Figure A4.3 Examples of daily eddy covariance (EC) footprints at sites (a) US−Bi1 (Alfalfa), (b) US−Bi2 (Corn), (c) US−Tw4 (Freshwater wetland), and (d) US−Snf (Pasture) from (a–c) January 1–3, 2018 and from (d) December 29–31, 2019. Additionally, annual cumulative footprints were denoted over (a) US−Bi2 from 2017 and (c) US−Tw4 from 2016. Contour lines delineate footprints within which (a–c) 50–90% and (d) 50–80% of the cumulative flux originated. Image source: red–green–black (RGB) Planet Fusion product (projection, WGS84/UTM zone 10N) for (a–c) January 1, 2018, and (d) December 29, 2019.

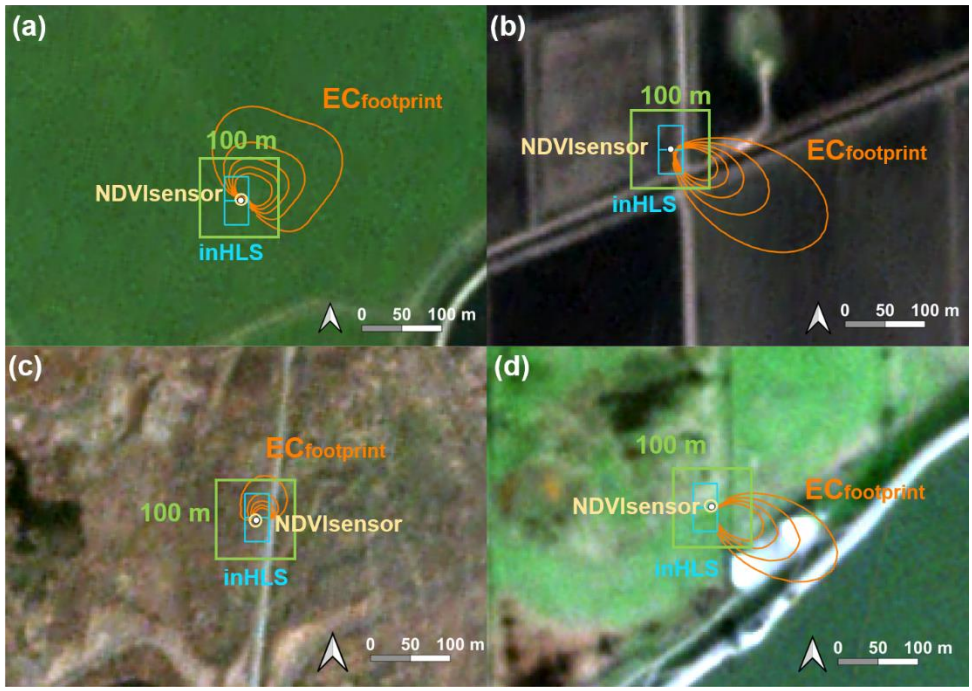

Figure A4.4 Examples of footprints for flux towers (white dots) at sites (a) US−Bi1 (Alfalfa), (b) US−Bi2 (Corn), (c) US−Tw4 (Freshwater wetland), and (d) US−Snf (Pasture) for different footprint types including eddy covariance footprint on January 1, 2018 (orange), a fixed 100 m × 100 m footprint (green) around the eddy covariance tower, and Harmonized Landsat/Sentinel (inHLS) pixels (cyan) including the normalized difference vegetation index (NDVI) sensor footprint (yellow). Contour lines denote the footprints within which 50–90% (a−c) and 50–80% (d) of the cumulative flux originated. Image source: RGB Planet Fusion surface reflectance product (projection, WGS84/UTM zone 10N) for (a–c) January 1, 2018, and (d) December 29, 2019.

Table A4.5 Comparison of NIRv and NIRvP derived from MODIS HSL, and observation-derived and gap-filled Planet Fusion (PF) data with *in situ* NIRv and NIRvP at each site. R^2, coefficient of determination; RMSE, root mean square error; rbias, relative bias; slope, slope of linear regression; n, number of samples.

Site ID	R^2	RMSE	Bias	rbias (%)	slope	R^2	RMSE	Bias	rbias (%)	slope	n
					MODIS						
			NIRv					NIRvP			
US-Bi1	0.42	0.09	0.05	33.0	0.38	0.82	95.80	46.26	17.7	0.73	365
US-Bi2	0.93	0.03	0.01	5.5	0.99	0.94	49.44	1.60	1.0	0.98	364
US-Tw4	0.94	0.14	0.13	368.6	2.14	0.94	221.49	196.64	322.6	2.83	313
US-Myb	0.74	0.15	0.13	294.3	2.55	0.89	259.70	216.15	280.7	3.37	338
US-Snf	0.80	0.09	0.09	104.7	0.67	0.94	124.67	118.38	82.4	1.24	185
Overall	0.44	0.11	0.08	91.9	0.66	0.51	170.07	111.17	77.8	0.81	1565
					HLS						
			NIR					NIRvP			
US-Bi1	0.70	0.09	0.08	37.6	1.01	0.85	131.41	107.88	32.1	1.02	50
US-Bi2	0.95	0.04	-0.02	-13.1	0.76	0.96	68.35	-34.32	-15.5	0.77	48
US-Tw4	0.84	0.11	0.11	229.6	1.54	0.92	182.68	176.36	216.4	1.80	41
US-Myb	0.52	0.02	0.01	18.5	0.91	0.64	35.22	16.50	16.1	0.95	42
US-Snf	0.75	0.07	0.06	63.1	1.02	0.91	111.82	102.89	59.0	1.30	28
Overall	0.69	0.07	0.05	41.2	0.94	0.73	116.94	69.62	36.4	0.92	209
					Observed Planet Fusion						
			NIRv					NIRvP			
US-Bi1	0.75	0.09	0.08	39.2	1.04	0.88	126.86	107.05	33.3	1.04	177
US-Bi2	0.98	0.02	-0.01	-6.1	0.85	0.98	44.29	-17.28	-8.2	0.85	184
US-Tw4	0.83	0.10	0.10	212.7	1.71	0.94	165.68	157.50	198.1	1.94	176
US-Myb	0.81	0.01	0.01	9.4	0.69	0.92	15.62	5.95	6.3	0.81	174
US-Snf	0.90	0.05	0.05	50.1	0.71	0.98	69.76	68.14	42.1	1.01	101
Overall	0.74	0.07	0.04	41.8	0.98	0.79	102.76	63.31	36.1	0.96	812
					Gap-filled Planet Fusion						
			NIRv					NIRvP			
US-Bi1	0.54	0.12	0.10	59.5%	0.76	0.90	121.87	103.40	39.7	1.03	365
US-Bi2	0.98	0.02	0.00	-0.5%	0.84	0.98	36.85	-9.12	-5.9	0.85	364
US-Tw4	0.86	0.09	0.09	246.4%	1.74	0.94	143.85	128.26	210.4	2.14	313
US-Myb	0.82	0.01	0.01	18.9%	0.65	0.94	15.21	6.79	8.8	0.86	338
US-Snf	0.87	0.05	0.05	59.9%	0.65	0.97	66.06	63.24	44.0	1.07	185
Overall	0.69	0.08	0.05	55.7%	0.99	0.83	92.11	56.59	39.6	1.01	1565

Table A4.6 Comparison of GPP *in situ* measurements at satellite passing time with NIRv (NIRvP) derived from *in situ* measurements and Planet Fusion for different footprint types. R^2, coefficient of determination; slope, slope of linear regression; n, number of samples.

Site ID		*In situ*	$NDVI_{sensor}$	100m	$EC_{footprint}$	$EC_{footprint}$ (30 m resolution)
			NIRv			
US-Bi1	R^2	0.76	0.56	0.57	0.60	0.61
	Slope	105.33	87.26	99.58	96.45	98.22
	n	365	365	365	359	298
US-Bi2	R^2	0.89	0.87	0.85	0.84	0.84
	Slope	158.20	183.93	231.13	152.68	152.55
	n	364	365	365	355	346
US-Tw4	R^2	0.92	0.87	0.88	0.88	0.93
	Slope	343.22	171.18	189.37	184.91	163.77
	n	313	365	365	354	66
US-Myb	R^2	0.69	0.59	0.57	0.81	0.77
	Slope	263.12	327.34	186.86	123.12	119.92
	n	338	365	365	360	274
US-Snf	R^2	0.82	0.80	0.87	0.77	0.63
	Slope	138.70	195.73	197.28	163.16	157.66
	n	185	185	185	181	132
Overall	R^2	0.58	0.43	0.46	0.62	0.64
	Slope	105.98	76.43	94.85	101.59	99.78
	n	1565	1645	1645	1609	1116
			NIRvP			
US-Bi1	R^2	0.71	0.78	0.79	0.80	0.81
	Slope	0.05	0.05	0.05	0.05	0.05
	n	365	365	365	359	298
US-Bi2	R^2	0.88	0.87	0.86	0.86	0.86
	Slope	0.09	0.10	0.12	0.08	0.08
	n	364	365	365	355	346
US-Tw4	R^2	0.87	0.91	0.86	0.89	0.83
	Slope	0.18	0.08	0.08	0.08	0.06
	n	313	364	364	354	66
US-Myb	R^2	0.84	0.83	0.83	0.92	0.90
	Slope	0.14	0.15	0.09	0.06	0.06
	n	338	365	365	360	274
US-Snf	R^2	0.83	0.85	0.85	0.88	0.85
	Slope	0.06	0.06	0.06	0.06	0.06
	n	185	185	185	181	132
Overall	R^2	0.61	0.61	0.65	0.78	0.78
	Slope	0.06	0.05	0.06	0.06	0.06
	n	1565	1644	1644	1609	1116

Table A4.7 Comparison of *in situ* daily GPP measurements with daily NIRvP and NIRv × $\mathbf{PAR}_{\mathbf{daily}}^{\mathbf{BESS}}$ for all sites.

Site ID		Daily NIRvP		NIRv x $\mathbf{PAR}_{\mathbf{daily}}^{\mathbf{BESS}}$	
		$\mathbf{NIRvP}^{in\ situ}$	$\mathbf{NIRvP}_{\mathbf{ECfootprint}}^{\mathbf{PF}}$	*In situ*	Planet Fusion
US-Bi1	R^2	0.80	0.82	0.79	0.80
	Slope	0.80	0.67	0.68	0.69
	RMSE	2.33	4.51	3.21	4.24
	n	365	359	365	359
US-Bi2	R^2	0.86	0.83	0.85	0.82
	Slope	1.17	0.98	1.02	1.01
	RMSE	2.62	2.80	2.63	2.83
	n	365	355	364	355
US-Tw4	R^2	0.90	0.91	0.90	0.89
	Slope	2.32	0.94	2.35	1.00
	RMSE	4.03	1.51	4.15	1.48
	n	341	354	313	354
US-Myb	R^2	0.90	0.92	0.85	0.92
	Slope	1.87	0.74	1.96	0.81
	RMSE	3.13	1.56	3.29	1.24
	n	339	360	338	360
US-Snf	R^2	0.83	0.85	0.83	0.84
	Slope	0.86	0.67	0.78	0.70
	RMSE	1.13	2.85	1.37	2.56
	n	185	181	185	181
Overall	R^2	0.67	0.80	0.62	0.79
	Slope	0.91	0.77	0.76	0.80
	RMSE	2.68	2.08	2.88	2.15
	n	1595	1609	1565	1609

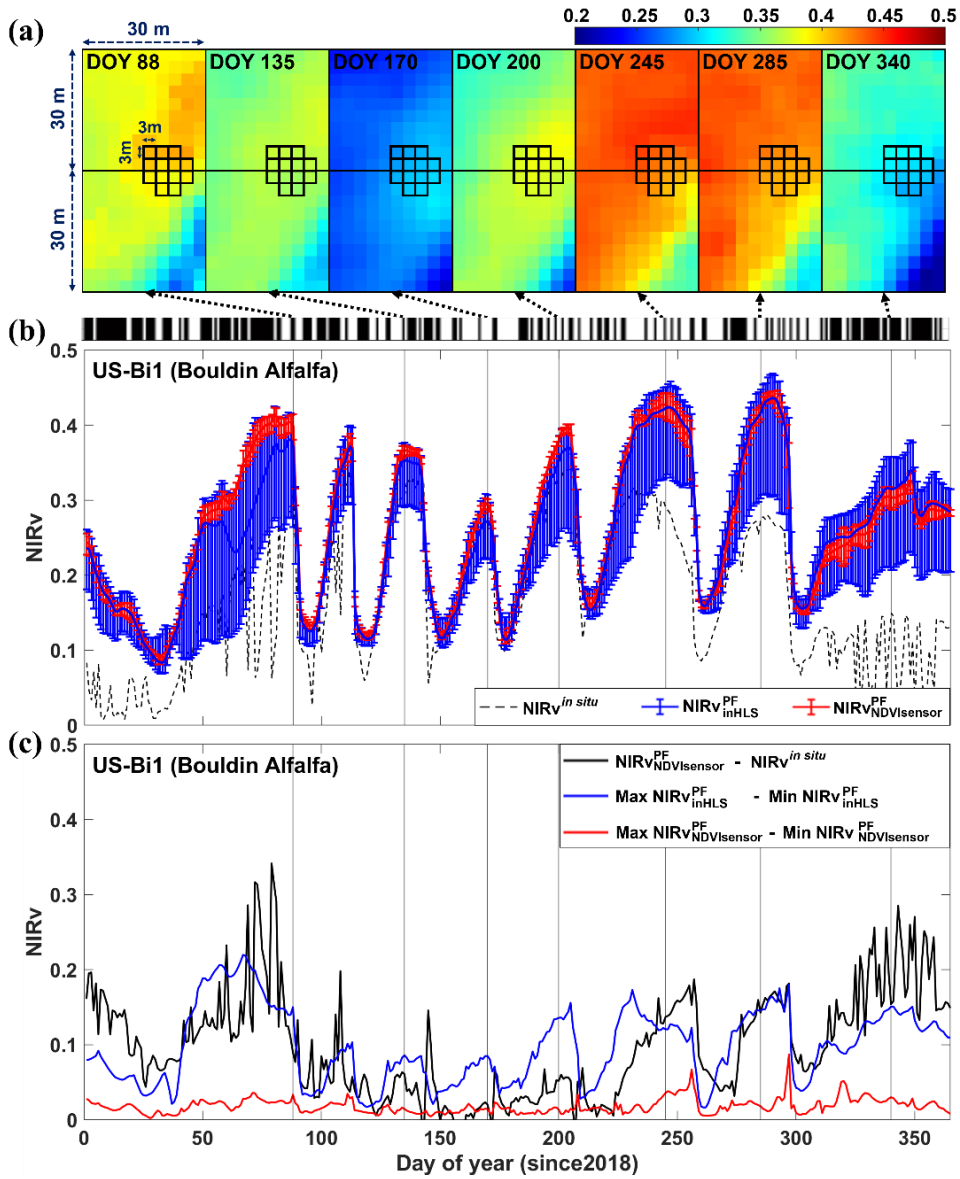

Figure A4.8 (a) Spatial variation in Planet Fusion (PF) NIRv in inHLS footprints, which comprised two 30 m × 30 m boxes, and $NDVI_{sensor}$ footprints, which comprised 13 black boxes (3 m × 3 m in size) at site US−Bi1 (Alfalfa). (b) Seasonal variation in NIRv at site US−Bi1, derived from Planet Fusion with $NDVI_{sensor}$ footprint (red line), Planet Fusion with inHLS footprint (blue line), and *in situ* sensor (black dashed line), where black lines on top of the plot indicate gap−filled data. Vertical lines indicate mean, maximum, and minimum values for $\mathbf{NIRv^{PF}_{NDVIsensor}}$ and $\mathbf{NIRv^{PF}_{inHLS}}$ data. (c) Differences between $\mathbf{NIRv^{PF}_{NDVIsensor}}$ and $\mathbf{NIRv^{in\ situ}}$ (black line). Blue and red lines indicate differences between maximum and minimum $\mathbf{NIRv^{PF}_{inHLS}}$ and $\mathbf{NIRv^{PF}_{NDVIsensor}}$, respectively. NIRv is given in unitless.

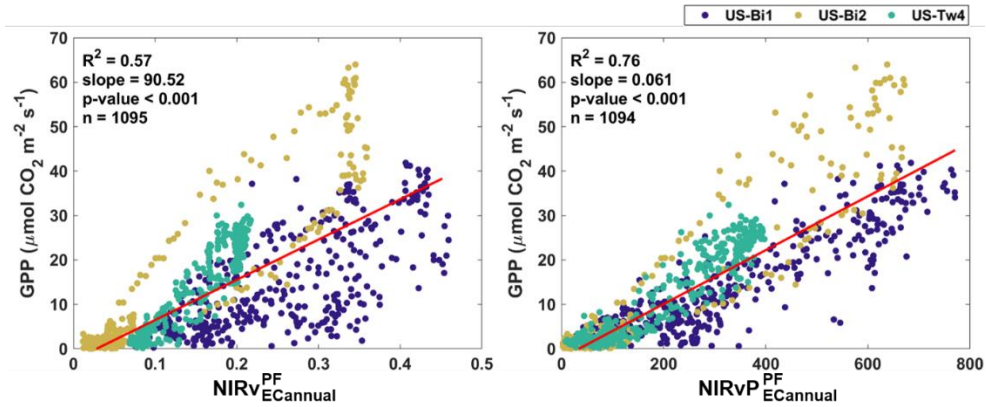

Figure A4.9 Comparison of NIRv and NIRvP measured derived from Planet Fusion (PF) in the annual cumulated eddy covariance footprint ($\mathbf{NIRv(NIRvP)^{PF}_{ECannual}}$) with GPP measured in study sites (colored circles) around satellite overpassing time. Red lines indicate linear regression model slopes for all sites. R^2 is the coefficient of determination, p-value indicates the significance of the linear regression, and n is the number of samples used in the linear regression model. I assumed that the shape of the cumulative footprint over US-Bi1 (Alfalfa) is similar to that over the nearby cropland site (i.e., US-Bi2, Corn), and I considered the inter-annual variations of cumulative footprints were small. The annual cumulative footprint over US-Tw4 (Freshwater wetland) (2016) and US-Bi2 (2017) were used (Figure A3). NIRv and NIRvP are given in unitless and unit of μmol m^{-2} s^{-1}, respectively.

Supplementary Materials

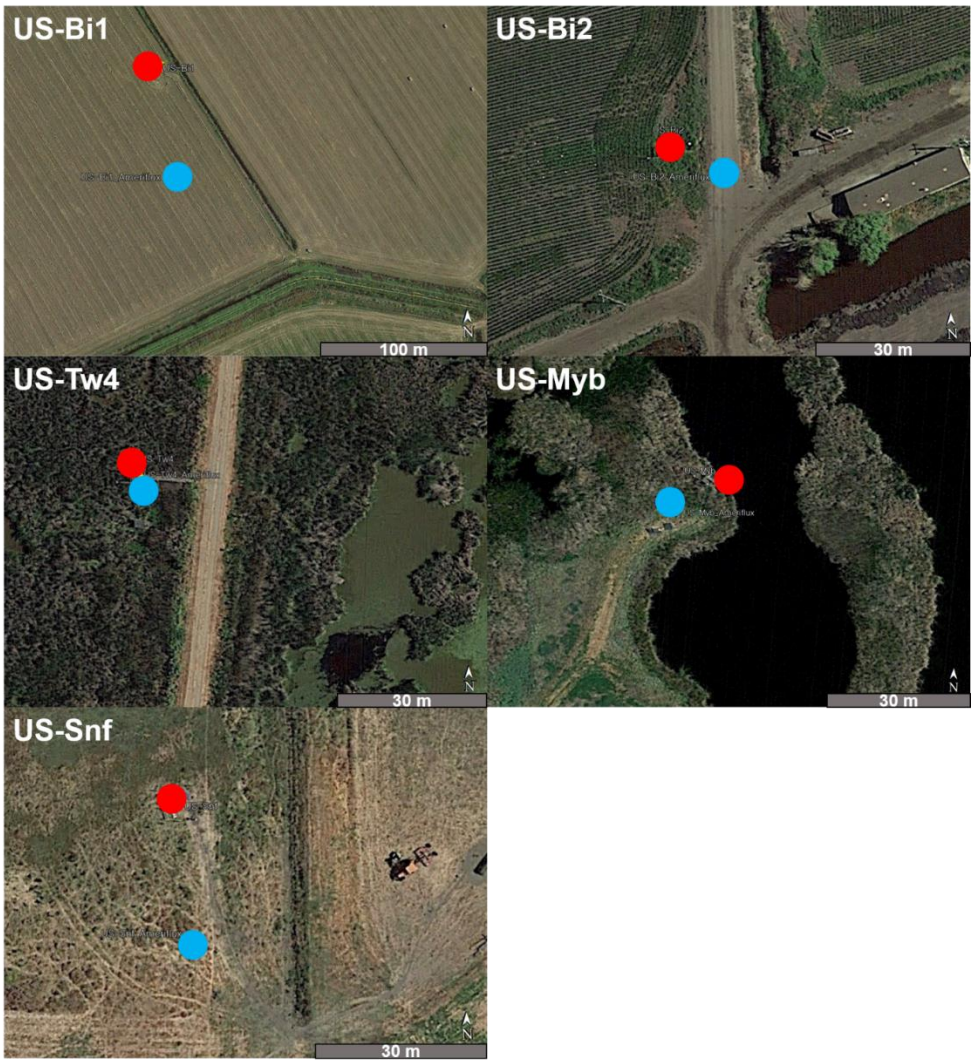

Figure S4.1 Location of fluxtower: registered in Ameriflux (Blue) and corrected location in this study (Red) over the study sites (Image source: Google Earth).

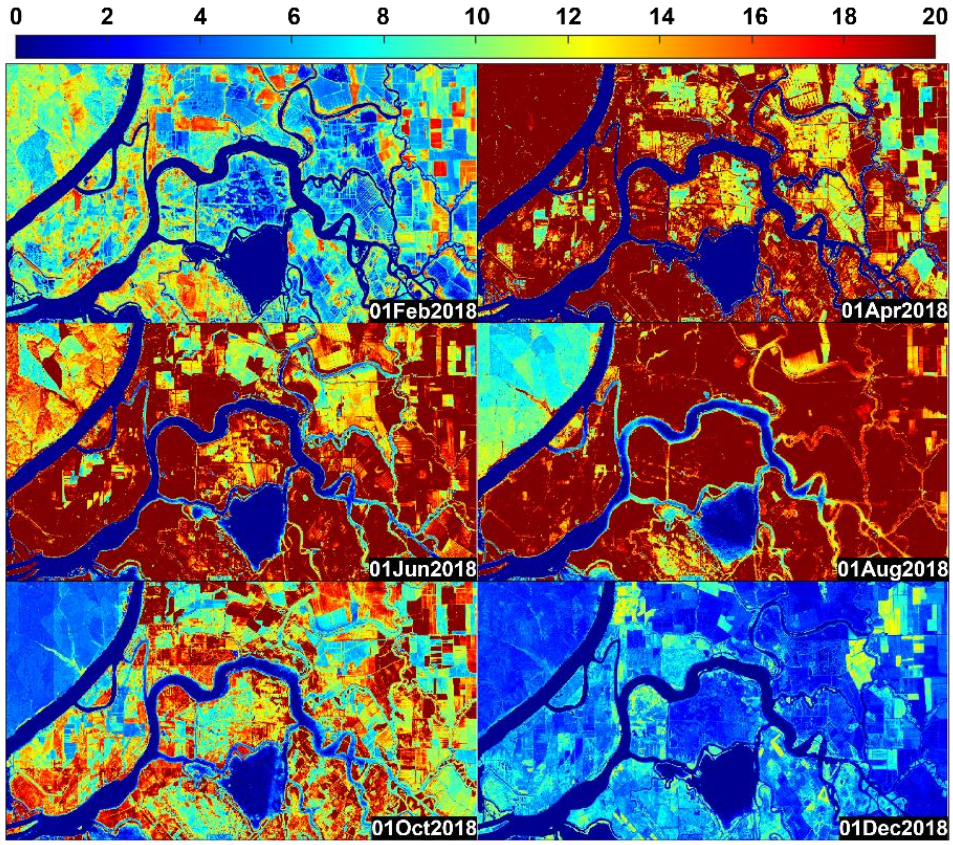

Figure S4.2 Maps of NIRvP derived from the combined Planet Fusion surface reflectance product and BESS daily PAR product throughout 2018 (projection, WGS84/UTM zone 10N; area, 30.6 km × 14.2 km = 433 km^2). NIRvP is given in unit of mol m^{-2} d^{-1}.

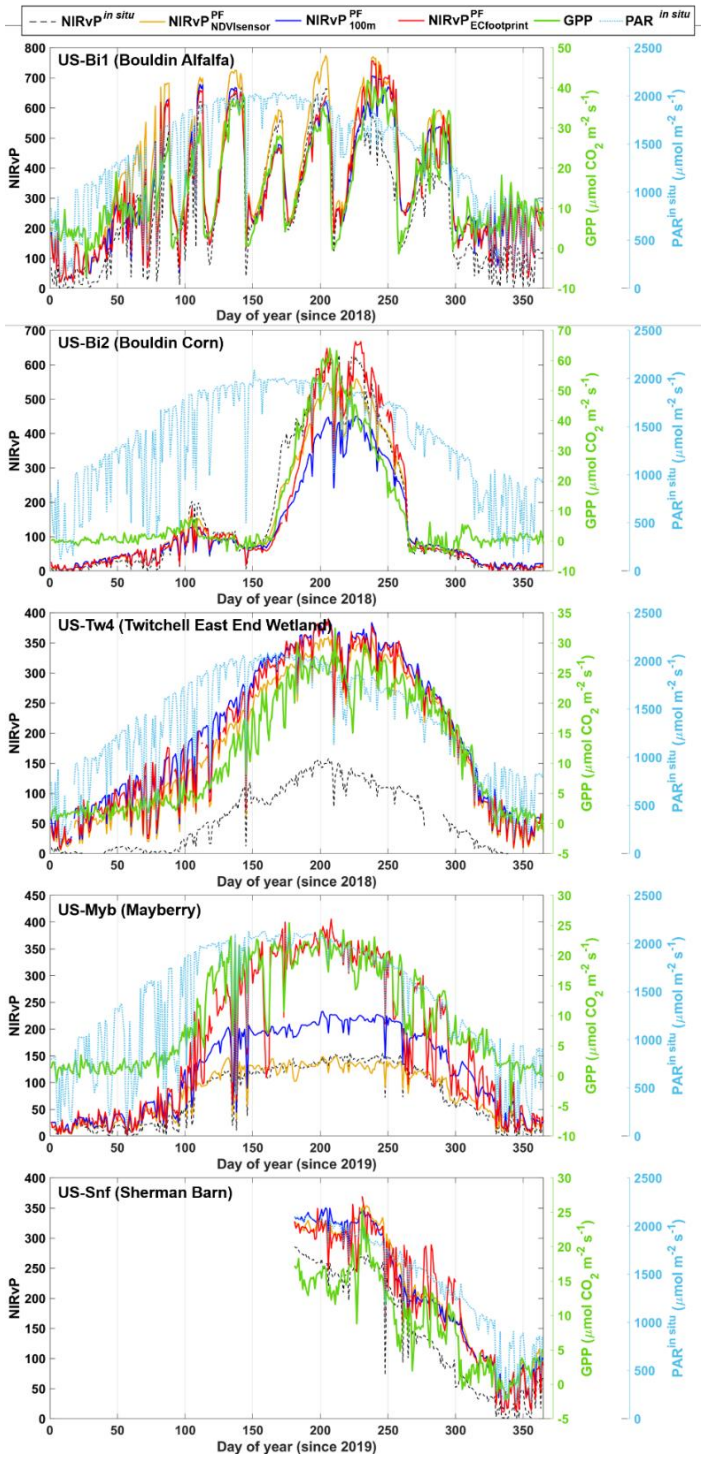

Figure S4.3 Seasonal variation of NIRvP from *in situ* and Planet Fusion (PF) in different footprint types (left axis), that of GPP (right axis; green), and *in situ* PAR (right axis; blue) around satellite passing time. NIRvP is given in unit of μmol m^{-2} s^{-1}.

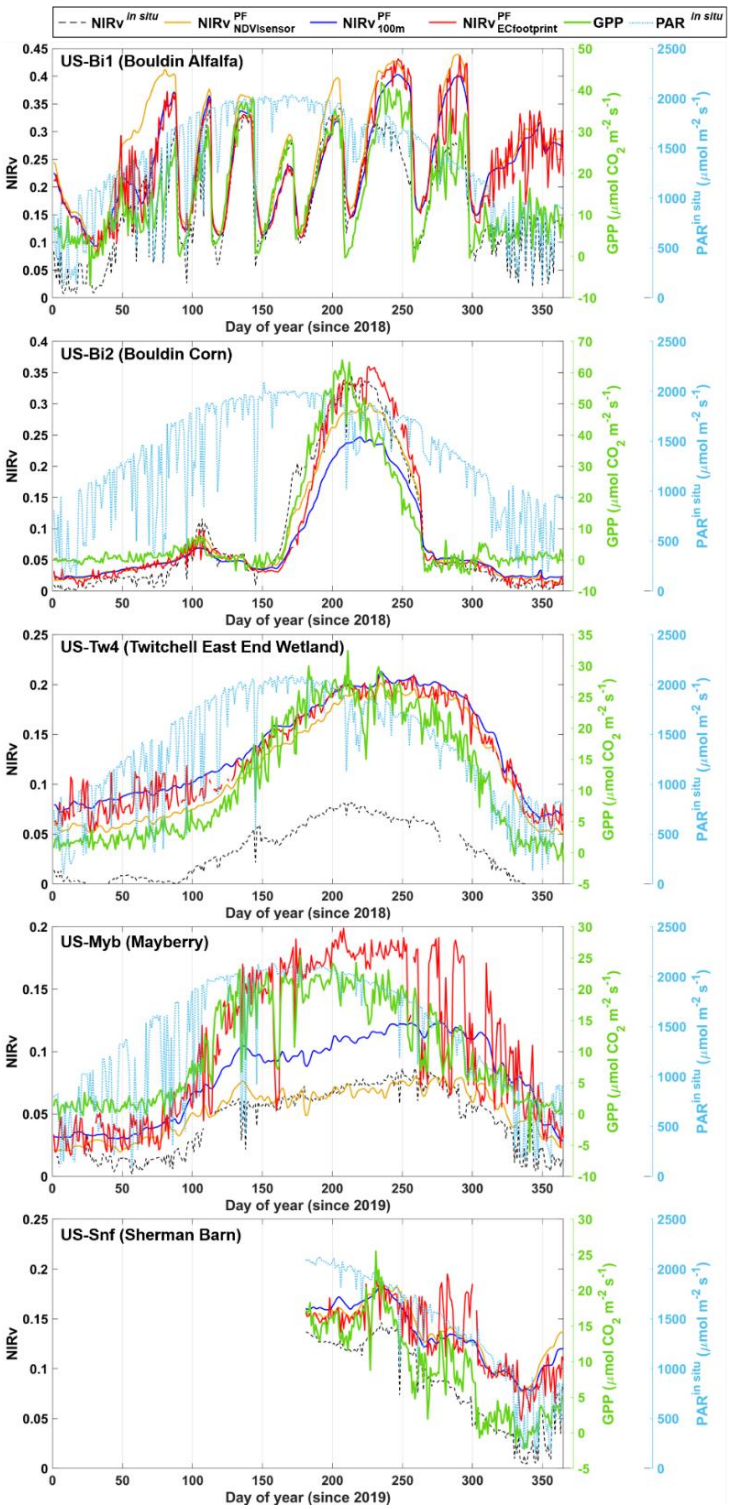

Figure S4.4 Seasonal variation of NIRv from *in situ* and Planet Fusion (PF) in different footprint types (left axis), that of GPP (right axis; green), and *in situ* PAR (right axis; blue) around satellite passing time. NIRv is given in unitless.

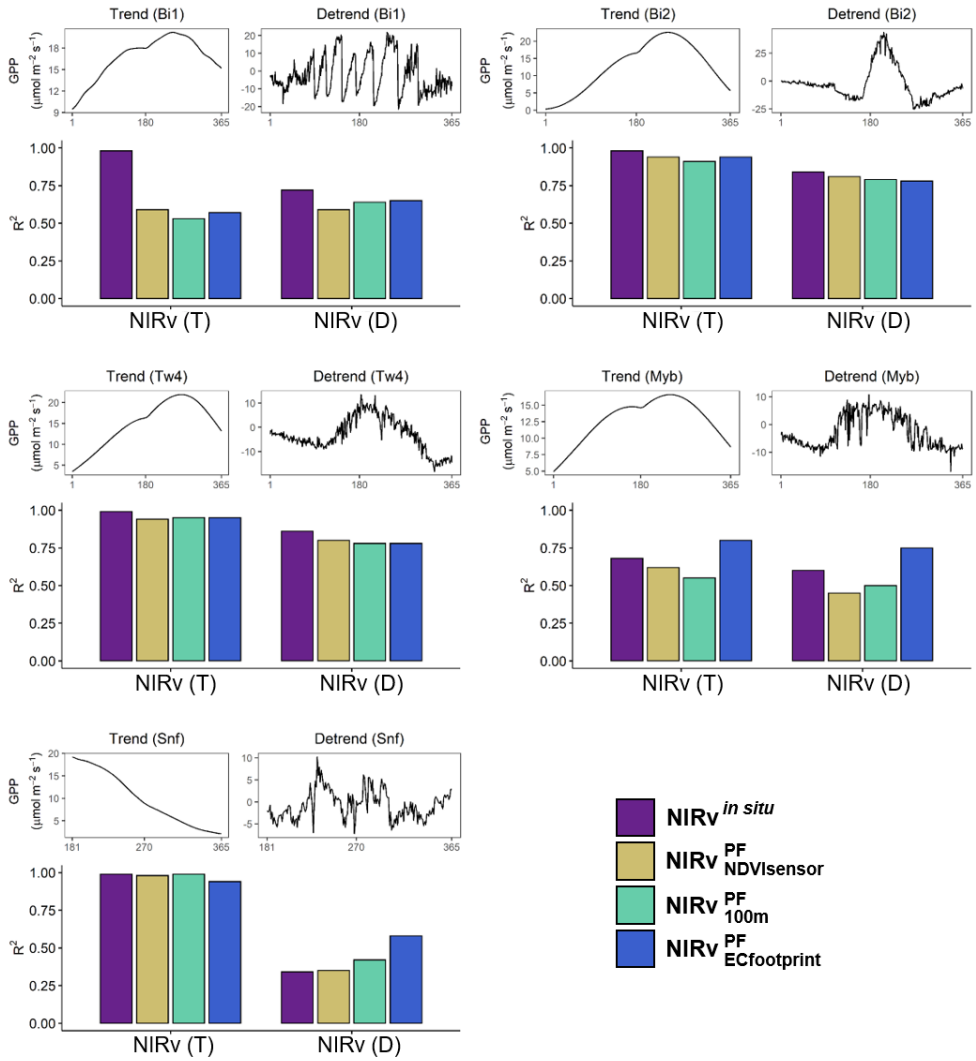

Figure S4.5 The GPP trend (T) and detrended (D) GPP at each site. Linear relationships of gap−filled Planet Fusion (PF) NIRv and *in situ* NIRv with T and D at the satellite passing time are also shown. $\mathbf{NIRv}^{\mathbf{PF}}_{\mathbf{NDVIsensor}}$, $\mathbf{NIRv}^{\mathbf{PF}}_{\mathbf{100m}}$, $\mathbf{NIRv}^{\mathbf{PF}}_{\mathbf{ECfootprint}}$ denotes Planet Fusion −derived NIRv around the local satellite overpassing time in different footprint type (i.e., $NDVI_{sensor}$, 100m, and $EC_{footprint}$). Detailed site data for the entire study period are shown in (Figure S4).

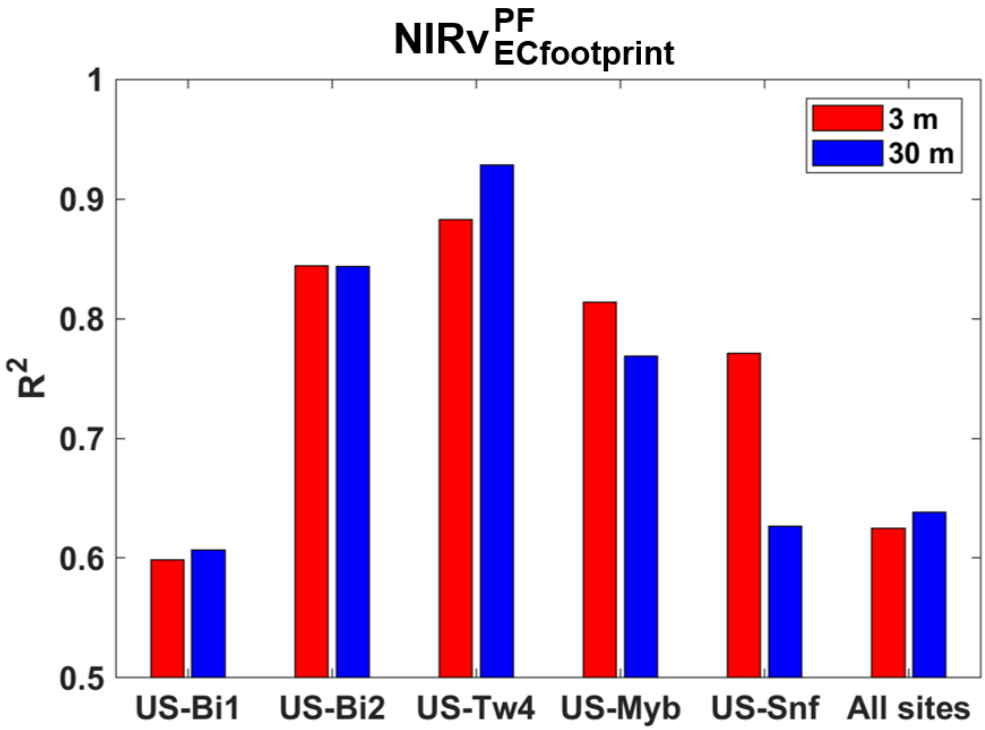

Figure S4.6 Evaluation of Planet Fusion (PF) derived NIRv within eddy covariance (EC) footprint in different spatial resolution against GPP around satellite passing time. $\mathbf{NIRv}^{\mathbf{PF}}_{\mathbf{ECfootprint}}$ denotes Planet Fusion–derived NIRv in daily eddy covariance footprints at the local satellite overpassing time. The linear relationships against GPP are shown. The detailed numbers are in (Table A6).

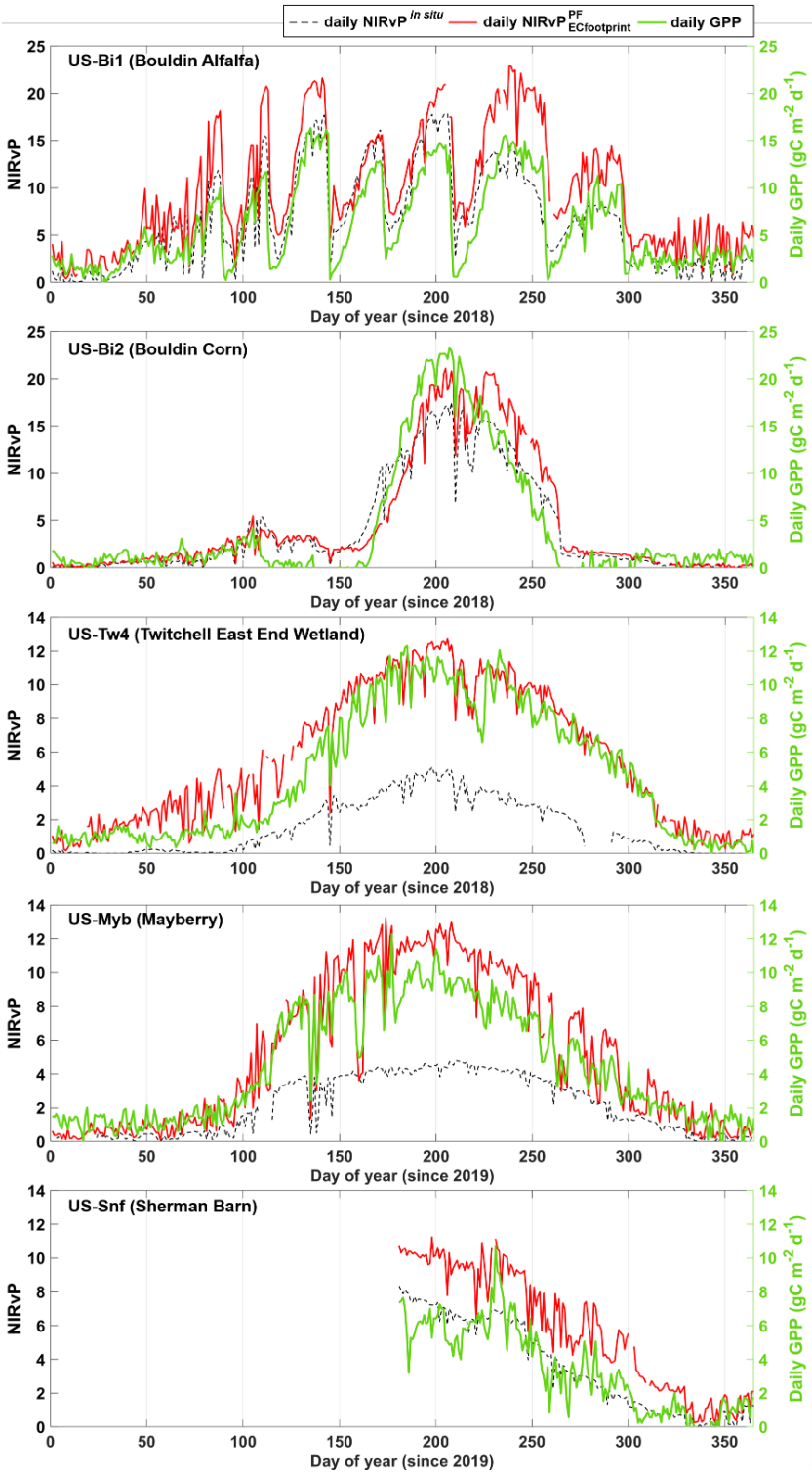

Figure S4.7 Seasonal variation of daily NIRvP from *in situ* and Planet Fusion (PF) in different footprint types (left axis) and that of daily GPP (right axis). NIRvP is given in unit of mol m^{-2} d^{-1}.

Figure S4.8 Examples of daily eddy covariance (EC) footprints at sites (a) US-Bi1 (Alfalfa), (b) US-Bi2 (Corn), (c) US-Tw4 (Freshwater wetland), (d) US-Myb (Palustrine wetland), and (e) US-Snf (Pasture) from July 1-10 (colored lines at each date), 2018 (a-c) and 2019 (d-e). Contour lines delineate footprints within which (a-c) 50-90% and (d) 50-80% of the cumulative flux originated. Image source: red-green-black (RGB) Planet Fusion surface reflectance product (projection, WGS84/UTM zone 10N) for (a-c) July 1, 2018, and (d-e) July 1, 2019.

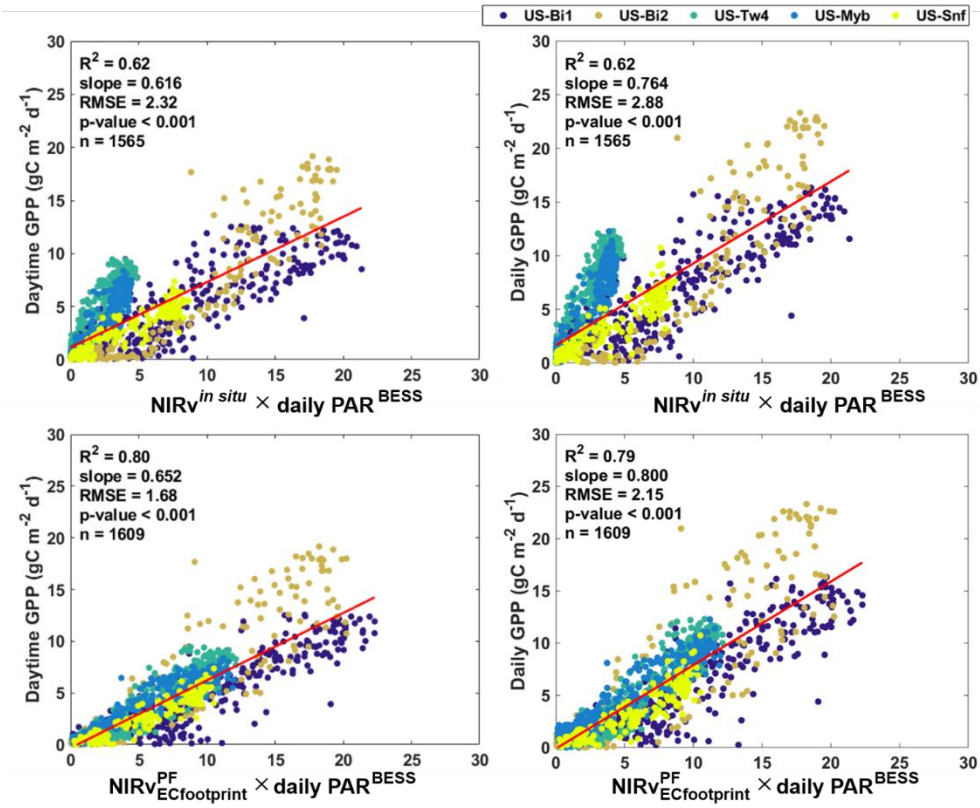

Figure S4.9 Linear relationships between *in situ*–measured and Planet Fusion (PF)–derived daily NIRvP and daily GPP at all sites (colored circles). Daily GPP is the whole day (0000hh – 2400hh) summed value and Daytime GPP is daytime (0800hh–1800hh) summed value. **daily PAR^{BESS}** means daily summed PAR data retrieved from the satellite–based Breathing Earth System Simulator (BESS). Red line indicates the linear regression model slope of overall sites. R^2 is the coefficient of determination, p–value indicates the significance of the linear regression, and n is the number of samples used in the linear regression model. NIRvP is given in unit of mol m^{-2} d^{-1}.

Chapter 5. Conclusion

Enhancement of the spatiotemporal resolution of archived satellite datasets is essential for monitoring long-term changes in vegetation within heterogeneous landscapes. In Chapter 2, the proposed system enables us to monitor daily canopy photosynthesis dynamics among regions of interest worldwide with high spatial resolution. In Chapter 3, I proposed a dual RSS-GAN model using Planet Fusion and Landsat 8 products for generating long-term, super-resolution satellite data. The dual RSS-GAN model retained the strengths of GAN-based methods in terms of rescaling and improving the underestimation of vegetation indices from Landsat 8. The proposed approach offers a promising direction for the adoption of dual RSS-GAN models in monitoring long-term vegetation dynamics among regions of interest worldwide. In Chapter 4, I found that the best agreement between flux tower GPP and NIRvP calculated from the Planet Fusion was achieved when matching the Planet Fusion imagery to the tower flux footprints. In fact, the agreement between Planet Fusion NIRvP and tower GPP was even considerably better than the agreement between *in situ* NIRvP and tower GPP. This indicates a large impact of the mismatch between flux tower footprint and the area covered by optical sensors due to spatial heterogeneity within the temporally varying flux tower footprint. I found the largest effects of such mismatches in wetland sites that have a temporally varying fraction of vegetation in a given area. Accordingly, high spatial resolution GPP maps at the landscape scale could prove very useful for precision agriculture or the monitoring of heterogeneous and dynamic natural ecosystems such as wetlands. Overall, our results demonstrated significant advantages of the high spatiotemporal resolution satellite imageries for daily canopy GPP estimation and for

upscaling flux data for model validation and parameterization. More generally, our findings indicate the large potential of sensor data fusion for high fidelity vegetation monitoring at unprecedented spatial and temporal resolutions. I encourage future efforts to test the proposed approach in a wide variety of ecosystems across diverse environmental conditions.

Bibliography

Achard, F., Eva, H.D., Mayaux, P., Stibig, H.-J. and Belward, A., 2004. Improved estimates of net carbon emissions from land cover change in the tropics for the 1990s. Global Biogeochemical Cycles, 18(2), https://doi.org/10.1029/2003GB002142.

Adeluyi, O., Harris, A., Verrelst, J., Foster, T. and Clay, G.D., 2021. Estimating the phenological dynamics of irrigated rice leaf area index using the combination of PROSAIL and Gaussian Process Regression. International Journal of Applied Earth Observation and Geoinformation, 102: 102454, https://doi.org/10.1016/j.jag.2021.102454.

Alexandrov, T., 2009. A Method of Trend Extraction Using Singular Spectrum Analysis. REVSTAT – Statistical Journa, 7.

Aragon, B., Houborg, R., Tu, K., Fisher, J.B. and McCabe, M., 2018. CubeSats Enable High Spatiotemporal Retrievals of Crop-Water Use for Precision Agriculture. Remote Sensing, 10(12): 1867, https://doi.org/10.3390/rs10121867.

Aragon, B., Ziliani, M.G., Houborg, R., Franz, T.E. and McCabe, M.F., 2021. CubeSats deliver new insights into agricultural water use at daily and 3 m resolutions. Scientific Reports, 11(1): 12131, https://doi.org/10.1038/s41598-021-91646-w.

Atkinson, P.M. and Curran, P.J., 1995. Defining an optimal size of support for remote sensing investigations. IEEE Transactions on Geoscience and Remote Sensing, 33(3): 768-776, https://doi.org10.1109/36.387592.

Badgley, G., Anderegg, L.D.L., Berry, J.A. and Field, C.B., 2019. Terrestrial gross primary production: Using NIRV to scale from site to globe. Global Change Biology, 25(11): 3731–3740, https://doi.org/10.1111/gcb.14729.

Badgley, G., Field, C.B. and Berry, J.A., 2017. Canopy near–infrared reflectance and terrestrial photosynthesis. Science Advances, 3(3): e1602244, https://doi.org/10.1126/sciadv.1602244.

Baldocchi, D. et al., 2012. The challenges of measuring methane fluxes and concentrations over a peatland pasture. Agricultural and Forest Meteorology, 153: 177–187, https://doi.org/10.1016/j.agrformet.2011.04.013.

Baldocchi, D. et al., 2001. FLUXNET: A New Tool to Study the Temporal and Spatial Variability of Ecosystem–Scale Carbon Dioxide, Water Vapor, and Energy Flux Densities. Bulletin of the American Meteorological Society, 82(11): 2415–2434, https://doi.org/10.1175/1520–0477(2001)082<2415:Fantts>2.3.Co;2.

Baldocchi, D.D. et al., 2020. Outgoing Near–Infrared Radiation From Vegetation Scales With Canopy Photosynthesis Across a Spectrum of Function, Structure, Physiological Capacity, and Weather. Journal of Geophysical Research: Biogeosciences, 125(7): e2019JG005534, https://doi.org/10.1029/2019JG005534.

Beaulieu, M., Foucher, S., Haberman, D. and Stewart, C., 2018. Deep Image–To–Image Transfer Applied to Resolution Enhancement of Sentinel–2 Images, IGARSS 2018 – 2018

IEEE International Geoscience and Remote Sensing Symposium, pp. 2611-2614, https://doi.org/10.1109/IGARSS.2018.8517655.

Belov, A.M. and Denisova, A.Y., 2019. Spatial interpolation methods for spectral-spatial remote sensing image super-resolution algorithm based on gradient descent approach. Journal of Physics: Conference Series, 1368(3): 032006, https://doi.org/10.1088/1742-6596/1368/3/032006.

Bessho, K. et al., 2016. An Introduction to Himawari-8/9- Japan's New-Generation Geostationary Meteorological Satellites. 気象集誌. 第2輯, 94(2): 151-183, https://doi.org/10.2151/jmsj.2016-009.

Bierkens, M., Finke, P. and De Willigen, P., 2000. Upscaling and downscaling methods for environmental research. Kluwer Academic,

Blau, Y. and Michaeli, T., 2018. The perception-distortion tradeoff, Proceedings of the IEEE conference on computer vision and pattern recognition, pp. 6228-6237, https://doi.org/10.48550/arXiv.1711.06077.

Blau, Y. and Michaeli, T., 2019. Rethinking Lossy Compression: The Rate-Distortion-Perception Tradeoff. In: C. Kamalika and S. Ruslan (Editors), Proceedings of the 36th International Conference on Machine Learning. PMLR, Proceedings of Machine Learning Research, pp. 675--685, https://doi.org/10.48550/arXiv.1901.07821.

Cao, H., Han, L. and Li, L., 2022. Harmonizing surface reflectance between Landsat-7 ETM + , Landsat-8 OLI, and Sentinel-2 MSI over China. Environmental Science and Pollution Research, https://doi.org/10.1007/s11356-022-20771-4.

Carrer, D. et al., 2021. Casual Rerouting of AERONET Sun/Sky Photometers: Toward a New Network of Ground Measurements Dedicated to the Monitoring of Surface Properties? Remote Sensing, 13(16): 3072, https://doi.org/10.3390/rs13163072.

Chamberlain, S.D. et al., 2018. Soil properties and sediment accretion modulate methane fluxes from restored wetlands. Global Change Biology, 24(9): 4107-4121, https://doi.org/10.1111/gcb.14124.

Chen, B. et al., 2009. Assessing Tower Flux Footprint Climatology and Scaling Between Remotely Sensed and Eddy Covariance Measurements. Boundary-Layer Meteorology, 130(2): 137-167, https://doi.org/10.1007/s10546-008-9339-1.

Chen, B., Chen, L., Huang, B., Michishita, R. and Xu, B., 2018. Dynamic monitoring of the Poyang Lake wetland by integrating Landsat and MODIS observations. ISPRS Journal of Photogrammetry and Remote Sensing, 139: 75-87, https://doi.org/10.1016/j.isprsjprs.2018.02.021.

Chen, B. et al., 2011a. Assessing eddy-covariance flux tower location bias across the Fluxnet-Canada Research Network based on remote sensing and footprint modelling. Agricultural and Forest Meteorology, 151(1): 87-100,

https://doi.org/10.1016/j.agrformet.2010.09.005.

Chen, B. et al., 2012. Characterizing spatial representativeness of flux tower eddy-covariance measurements across the Canadian Carbon Program Network using remote sensing and footprint analysis. Remote Sensing of Environment, 124: 742-755, https://doi.org/10.1016/j.rse.2012.06.007.

Chen, B., Huang, B. and Xu, B., 2015. Comparison of Spatiotemporal Fusion Models: A Review. Remote Sensing, 7(2): 1798-1835.

Chen, J., Zhu, X., Vogelmann, J.E., Gao, F. and Jin, S., 2011b. A simple and effective method for filling gaps in Landsat ETM+ SLC-off images. Remote Sensing of Environment, 115(4): 1053-1064, https://doi.org/10.1016/j.rse.2010.12.010.

Chen, Y., Cao, R., Chen, J., Liu, L. and Matsushita, B., 2021. A practical approach to reconstruct high-quality Landsat NDVI time-series data by gap filling and the Savitzky-Golay filter. ISPRS Journal of Photogrammetry and Remote Sensing, 180: 174-190, https://doi.org/10.1016/j.isprsjprs.2021.08.015.

Cho, S. et al., 2021. Evaluation of forest carbon uptake in South Korea using the national flux tower network, remote sensing, and data-driven technology. Agricultural and Forest Meteorology, 311: 108653, https://doi.org/10.1016/j.agrformet.2021.108653.

Choi, Y., Sharifahmadian, E. and Latifi, S., 2013. Effect of pre-processing on satellite image fusion, The 17th CSI International Symposium on Computer Architecture & Digital

Systems (CADS 2013), pp. 111-115, https://doi.org/10.1109/CADS.2013.6714246.

Chu, H. et al., 2018. Temporal Dynamics of Aerodynamic Canopy Height Derived From Eddy Covariance Momentum Flux Data Across North American Flux Networks. Geophysical Research Letters, 45(17): 9275-9287, https://doi.org/10.1029/2018GL079306.

Chu, H. et al., 2021. Representativeness of Eddy-Covariance flux footprints for areas surrounding AmeriFlux sites. Agricultural and Forest Meteorology, 301-302: 108350, https://doi.org/10.1016/j.agrformet.2021.108350.

Chung, S.-R., Ahn, M.-H., Han, K.-S., Lee, K.-T. and Shin, D.-B., 2020. Meteorological Products of Geo-KOMPSAT 2A (GK2A) Satellite. Asia-Pacific Journal of Atmospheric Sciences, 56(2): 185-185, https://doi.org/10.1007/s13143-020-00199-x.

Ciais, P. et al., 2014. Current systematic carbon-cycle observations and the need for implementing a policy-relevant carbon observing system. Biogeosciences, 11(13): 3547-3602, https://doi.org/10.5194/bg-11-3547-2014.

Claverie, M. et al., 2018. The Harmonized Landsat and Sentinel-2 surface reflectance data set. Remote Sensing of Environment, 219: 145-161, https://doi.org/10.1016/j.rse.2018.09.002.

Cover, T.M., 1999. Elements of information theory. John Wiley & Sons,

Dechant, B. et al., 2022. NIRVP: A robust structural proxy for sun-

induced chlorophyll fluorescence and photosynthesis across scales. Remote Sensing of Environment, 268: 112763, https://doi.org/10.1016/j.rse.2021.112763.

Dechant, B. et al., 2020. Canopy structure explains the relationship between photosynthesis and sun-induced chlorophyll fluorescence in crops. Remote Sensing of Environment, 241: 111733, https://doi.org/10.1016/j.rse.2020.111733.

Dechant, B., Ryu, Y. and Kang, M., 2019. Making full use of hyperspectral data for gross primary productivity estimation with multivariate regression: Mechanistic insights from observations and process-based simulations. Remote Sensing of Environment, 234: 111435, https://doi.org/10.1016/j.rse.2019.111435.

Denton, E.L., Chintala, S., Szlam, A.D. and Fergus, R., 2015. Deep Generative Image Models using a Laplacian Pyramid of Adversarial Networks, NIPS.

Detto, M., Baldocchi, D. and Katul, G.G., 2010. Scaling Properties of Biologically Active Scalar Concentration Fluctuations in the Atmospheric Surface Layer over a Managed Peatland. Boundary-Layer Meteorology, 136(3): 407-430, https://doi.org/10.1007/s10546-010-9514-z.

Dong, C., Loy, C.C., He, K. and Tang, X., 2015. Image super-resolution using deep convolutional networks. IEEE transactions on pattern analysis and machine intelligence, 38(2): 295-307, https://doi.org/10.1109/TPAMI.2015.2439281.

Drusch, M. et al., 2012a. Sentinel-2: ESA's optical high-resolution mission for GMES operational services. Remote sensing of Environment, 120: 25-36, https://doi.org/10.1016/j.rse.2011.11.026.

Drusch, M. et al., 2012b. Sentinel-2: ESA's Optical High-Resolution Mission for GMES Operational Services. Remote Sensing of Environment, 120: 25-36, https://doi.org/10.1016/j.rse.2011.11.026.

Duffy, K., Vandal, T., Wang, W., Nemani, R. and Ganguly, A.R., 2019. Deep Learning Emulation of Multi-Angle Implementation of Atmospheric Correction (MAIAC), pp. arXiv:1910.13408.

Duveiller, G. and Defourny, P., 2010. A conceptual framework to define the spatial resolution requirements for agricultural monitoring using remote sensing. Remote Sensing of Environment, 114(11): 2637-2650, https://doi.org/10.1016/j.rse.2010.06.001.

Eichelmann, E. et al., 2018. The effect of land cover type and structure on evapotranspiration from agricultural and wetland sites in the Sacramento-San Joaquin River Delta, California. Agricultural and Forest Meteorology, 256-257: 179-195, https://doi.org/10.1016/j.agrformet.2018.03.007.

Eichelmann, E. et al., 2021. AmeriFlux US-Tw4 Twitchell East End Wetland, Ver. 11-5, AmeriFlux AMP, https://doi.org/10.17190/AMF/1246151.

Falge, E. et al., 2002. Seasonality of ecosystem respiration and gross

primary production as derived from FLUXNET measurements. Agricultural and Forest Meteorology, 113(1): 53-74, https://doi.org/10.1016/S0168-1923(02)00102-8.

Feddema, J.J. et al., 2005. The importance of land-cover change in simulating future climates. Science, 310(5754): 1674-1678, https://doi/10.1126/science.1118160.

Feng, G., Masek, J., Schwaller, M. and Hall, F., 2006. On the blending of the Landsat and MODIS surface reflectance: predicting daily Landsat surface reflectance. IEEE Transactions on Geoscience and Remote Sensing, 44(8): 2207-2218, https://doi.org/10.1109/TGRS.2006.872081.

Feng, G., Yufang, J., Schaaf, C.B. and Strahler, A.H., 2002. Bidirectional NDVI and atmospherically resistant BRDF inversion for vegetation canopy. IEEE Transactions on Geoscience and Remote Sensing, 40(6): 1269-1278, https://doi.org10.1109/TGRS.2002.800241.

Fensholt, R., Sandholt, I., Proud, S.R., Stisen, S. and Rasmussen, M.O., 2010. Assessment of MODIS sun-sensor geometry variations effect on observed NDVI using MSG SEVIRI geostationary data. International Journal of Remote Sensing, 31(23): 6163-6187, https://doi.org/10.1080/01431160903401387.

Fensholt, R., Sandholt, I., Stisen, S. and Tucker, C., 2006. Analysing NDVI for the African continent using the geostationary meteosat second generation SEVIRI sensor. Remote Sensing of Environment, 101(2): 212-229, https://doi.org/10.1016/j.rse.2005.11.013.

Fisher, J.B. et al., 2020. ECOSTRESS: NASA's Next Generation Mission to Measure Evapotranspiration From the International Space Station. Water Resources Research, 56(4): e2019WR026058, https://doi.org/10.1029/2019WR026058.

Frantz, D., 2019a. FORCE—Landsat + Sentinel-2 Analysis Ready Data and Beyond. Remote Sensing, 11(9), https://doi.org/10.3390/rs11091124.

Frantz, D., 2019b. FORCE—Landsat + Sentinel-2 Analysis Ready Data and Beyond. Remote Sensing, 11(9): 1124, https://doi.org/10.3390/rs11091124.

Gamon, J.A., 2015. Reviews and Syntheses: optical sampling of the flux tower footprint. Biogeosciences, 12(14): 4509-4523, https://doi.org/10.5194/bg-12-4509-2015.

Gao, F., Masek, J. and Wolfe, R., 2009. Automated registration and orthorectification package for Landsat and Landsat-like data processing. Journal of Applied Remote Sensing, 3(1): 033515, https://doi.org/10.1117/1.3104620.

Garrity, S.R., Vierling, L.A. and Bickford, K., 2010. A simple filtered photodiode instrument for continuous measurement of narrowband NDVI and PRI over vegetated canopies. Agricultural and Forest Meteorology, 150(3): 489-496, https://doi.org/10.1016/j.agrformet.2010.01.004.

Gebbers, R. and Adamchuk, V.I., 2010. Precision Agriculture and Food Security. Science, 327(5967): 828-831, https://doi.org/10.1126/science.1183899.

Geman, S., Bienenstock, E. and Doursat, R., 1992. Neural Networks and the Bias/Variance Dilemma. Neural Computation, 4(1): 1–58, https://doi.org/10.1162/neco.1992.4.1.1.

Gevaert, C.M. and García–Haro, F.J., 2015. A comparison of STARFM and an unmixing–based algorithm for Landsat and MODIS data fusion. Remote Sensing of Environment, 156: 34–44, https://doi.org/10.1016/j.rse.2014.09.012.

Ghil, M. et al., 2002. ADVANCED SPECTRAL METHODS FOR CLIMATIC TIME SERIES. Reviews of Geophysics, 40(1): 3–1–3–41, https://doi.org/10.1029/2000RG000092.

Giannico, V. et al., 2018. Contributions of landscape heterogeneity within the footprint of eddy–covariance towers to flux measurements. Agricultural and Forest Meteorology, 260–261: 144–153, https://doi.org/10.1016/j.agrformet.2018.06.004.

Golyandina, N., Korobeynikov, A. and Zhigljavsky, A., 2018. Singular spectrum analysis with R. Springer,

Goodfellow, I. et al., 2014. Generative adversarial nets. Advances in neural information processing systems, 27, https://doi.org/10.48550/arXiv.1406.2661.

Griffiths, P., Nendel, C. and Hostert, P., 2019. Intra–annual reflectance composites from Sentinel–2 and Landsat for national–scale crop and land cover mapping. Remote Sensing of Environment, 220: 135–151, https://doi.org/10.1016/j.rse.2018.10.031.

Haboudane, D., Miller, J.R., Pattey, E., Zarco-Tejada, P.J. and Strachan, I.B., 2004. Hyperspectral vegetation indices and novel algorithms for predicting green LAI of crop canopies: Modeling and validation in the context of precision agriculture. Remote sensing of environment, 90(3): 337-352, https://doi.org/10.1016/j.rse.2003.12.013.

Haboudane, D., Tremblay, N., Miller, J.R. and Vigneault, P., 2008. Remote estimation of crop chlorophyll content using spectral indices derived from hyperspectral data. IEEE Transactions on Geoscience and Remote Sensing, 46(2): 423-437, https://doi.org/10.1109/TGRS.2007.904836.

Hagen, S.C. et al., 2006. Statistical uncertainty of eddy flux-based estimates of gross ecosystem carbon exchange at Howland Forest, Maine. Journal of Geophysical Research: Atmospheres, 111(D8), https://doi.org/10.1029/2005JD006154.

Halabisky, M., Moskal, L.M., Gillespie, A. and Hannam, M., 2016. Reconstructing semi-arid wetland surface water dynamics through spectral mixture analysis of a time series of Landsat satellite images (1984-2011). Remote Sensing of Environment, 177: 171-183, https://doi.org/10.1016/j.rse.2016.02.040.

Hashimoto, H. et al., 2021. New generation geostationary satellite observations support seasonality in greenness of the Amazon evergreen forests. Nature Communications, 12(1): 684, https://doi.org/10.1038/s41467-021-20994-y.

He, T., Zhang, Y., Liang, S., Yu, Y. and Wang, D., 2019. Developing

Land Surface Directional Reflectance and Albedo Products from Geostationary GOES-R and Himawari Data: Theoretical Basis, Operational Implementation, and Validation. Remote Sensing, 11(22): 2655, https://doi.org/doi:10.3390/rs11222655.

Heinsch, F.A. et al., 2006. Evaluation of remote sensing based terrestrial productivity from MODIS using regional tower eddy flux network observations. IEEE Transactions on Geoscience and Remote Sensing, 44(7): 1908-1925, https://doi.org/10.1109/TGRS.2005.853936.

Helder, D. et al., 2020. Observations and Recommendations for Coordinated Calibration Activities of Government and Commercial Optical Satellite Systems. Remote Sensing, 12(15), https://doi.org/10.3390/rs12152468.

Helder, D. et al., 2018. Observations and Recommendations for the Calibration of Landsat 8 OLI and Sentinel 2 MSI for Improved Data Interoperability. Remote Sensing, 10(9): 1340, https://doi.org/10.3390/rs10091340.

Hemes, K.S. et al., 2019. Assessing the carbon and climate benefit of restoring degraded agricultural peat soils to managed wetlands. Agricultural and Forest Meteorology, 268: 202-214, https://doi.org/10.1016/j.agrformet.2019.01.017.

Hemes, K.S., Verfaillie, J. and Baldocchi, D.D., 2020. Wildfire-Smoke Aerosols Lead to Increased Light Use Efficiency Among Agricultural and Restored Wetland Land Uses in California's Central Valley. Journal of Geophysical Research:

Biogeosciences, 125(2): e2019JG005380, https://doi.org/10.1029/2019JG005380.

Houborg, R. and McCabe, M.F., 2016. High-Resolution NDVI from Planet's Constellation of Earth Observing Nano-Satellites: A New Data Source for Precision Agriculture. Remote Sensing, 8(9), https://doi.org/10.3390/rs8090768.

Houborg, R. and McCabe, M.F., 2018a. A Cubesat enabled Spatio-Temporal Enhancement Method (CESTEM) utilizing Planet, Landsat and MODIS data. Remote Sensing of Environment, 209: 211-226, https://doi.org/10.1016/j.rse.2018.02.067.

Houborg, R. and McCabe, M.F., 2018b. Daily Retrieval of NDVI and LAI at 3 m Resolution via the Fusion of CubeSat, Landsat, and MODIS Data. Remote Sensing, 10(6): 890, https://doi.org/10.3390/rs10060890.

Houborg, R. and McCabe, M.F., 2018c. A hybrid training approach for leaf area index estimation via Cubist and random forests machine-learning. ISPRS Journal of Photogrammetry and Remote Sensing, 135: 173-188, https://doi.org/10.1016/j.isprsjprs.2017.10.004.

Houghton, R.A. and Nassikas, A.A., 2017. Global and regional fluxes of carbon from land use and land cover change 1850-2015. Global Biogeochemical Cycles, 31(3): 456-472, https://doi.org/10.1002/2016GB005546.

Huang, Y. et al., 2018. BESS-Rice: A remote sensing derived and biophysical process-based rice productivity simulation model.

Agricultural and Forest Meteorology, 256–257: 253–269, https://doi.org/10.1016/j.agrformet.2018.03.014.

Hwang, Y. et al., 2020. Comprehensive assessments of carbon dynamics in an intermittently–irrigated rice paddy. Agricultural and Forest Meteorology, 285–286: 107933, https://doi.org/10.1016/j.agrformet.2020.107933.

Hwang, Y., Ryu, Y. and Qu, S., 2022. Expanding vegetated areas by human activities and strengthening vegetation growth concurrently explain the greening of Seoul. Landscape and Urban Planning, 227: 104518, https://doi.org/10.1016/j.landurbplan.2022.104518.

Irons, J.R., Dwyer, J.L. and Barsi, J.A., 2012. The next Landsat satellite: The Landsat data continuity mission. Remote Sensing of Environment, 122: 11–21, https://doi.org/10.1016/j.rse.2011.08.026.

Ishii, H.T., Tanabe, S.–i. and Hiura, T., 2004. Exploring the Relationships Among Canopy Structure, Stand Productivity, and Biodiversity of Temperate Forest Ecosystems. Forest Science, 50(3): 342–355, https://doi.org/10.1093/forestscience/50.3.342.

Jiang, C., Guan, K., Wu, G., Peng, B. and Wang, S., 2021. A daily, 250m and real–time gross primary productivity product (2000–present) covering the contiguous United States. Earth Syst. Sci. Data, 13(2): 281–298, https://doi.org/10.5194/essd–13–281–2021.

Johansen, K., Ziliani, M.G., Houborg, R., Franz, T.E. and McCabe, M.F., 2022. CubeSat constellations provide enhanced crop phenology and digital agricultural insights using daily leaf area index retrievals. Scientific Reports, 12(1): 5244, https://doi.org/10.1038/s41598-022-09376-6.

Ju, J. and Roy, D.P., 2008. The availability of cloud-free Landsat ETM+ data over the conterminous United States and globally. Remote Sensing of Environment, 112(3): 1196-1211, https://doi.org/10.1016/j.rse.2007.08.011.

Justice, C.O. et al., 2002. An overview of MODIS Land data processing and product status. Remote Sensing of Environment, 83(1): 3-15, https://doi.org/10.1016/S0034-4257(02)00084-6.

Justice, C.O. et al., 1998. The Moderate Resolution Imaging Spectroradiometer (MODIS): land remote sensing for global change research. IEEE Transactions on Geoscience and Remote Sensing, 36(4): 1228-1249, https://doi.org/10.1109/36.701075.

Karnewar, A. and Wang, O., 2020. Msg-gan: Multi-scale gradients for generative adversarial networks, Proceedings of the IEEE/CVF conference on computer vision and pattern recognition, pp. 7799-7808, https://doi.org/10.48550/arXiv.1903.06048.

Kasak, K. et al., 2021. Restoring wetlands on intensive agricultural lands modifies nitrogen cycling microbial communities and reduces N2O production potential. Journal of Environmental

Management, 299: 113562, https://doi.org/10.1016/j.jenvman.2021.113562.

Kasak, K. et al., 2020. Experimental harvesting of wetland plants to evaluate trade-offs between reducing methane emissions and removing nutrients accumulated to the biomass in constructed wetlands. Science of The Total Environment, 715: 136960, https://doi.org/10.1016/j.scitotenv.2020.136960.

Kawulok, M., Tarasiewicz, T., Nalepa, J., Tyrna, D. and Kostrzewa, D., 2021. Deep Learning for Multiple-Image Super-Resolution of Sentinel-2 Data, 2021 IEEE International Geoscience and Remote Sensing Symposium IGARSS, pp. 3885-3888, https://doi.org/10.1109/IGARSS47720.2021.9553243.

Khan, A.M. et al., 2021. Reviews and syntheses: Ongoing and emerging opportunities to improve environmental science using observations from the Advanced Baseline Imager on the Geostationary Operational Environmental Satellites. Biogeosciences, 18(13): 4117-4141, https://doi.org/10.5194/bg-18-4117-2021.

Kim, J. et al., 2006. Upscaling fluxes from tower to landscape: Overlaying flux footprints on high-resolution (IKONOS) images of vegetation cover. Agricultural and Forest Meteorology, 136(3): 132-146, https://doi.org/10.1016/j.agrformet.2004.11.015.

Kim, J. et al., 2021. Solar-induced chlorophyll fluorescence is non-linearly related to canopy photosynthesis in a temperate

evergreen needleleaf forest during the fall transition. Remote Sensing of Environment, 258: 112362, https://doi.org/10.1016/j.rse.2021.112362.

Kim, J., Ryu, Y., Jiang, C. and Hwang, Y., 2019. Continuous observation of vegetation canopy dynamics using an integrated low-cost, near-surface remote sensing system. Agricultural and Forest Meteorology, 264: 164-177, https://doi.org/10.1016/j.agrformet.2018.09.014.

Kimm, H. et al., 2021. A physiological signal derived from sun-induced chlorophyll fluorescence quantifies crop physiological response to environmental stresses in the U.S. Corn Belt. Environmental Research Letters.

Kimm, H. et al., 2020. Deriving high-spatiotemporal-resolution leaf area index for agroecosystems in the U.S. Corn Belt using Planet Labs CubeSat and STAIR fusion data. Remote Sensing of Environment, 239: 111615, https://doi.org/10.1016/j.rse.2019.111615.

Kljun, N., Calanca, P., Rotach, M.W. and Schmid, H.P., 2015. A simple two-dimensional parameterisation for Flux Footprint Prediction (FFP). Geosci. Model Dev., 8(11): 3695-3713, 10.5194/gmd-8-3695-2015.

Knox, S.H. et al., 2015. Agricultural peatland restoration: effects of land-use change on greenhouse gas (CO2 and CH4) fluxes in the Sacramento-San Joaquin Delta. Global Change Biology, 21(2): 750-765, https://doi.org/10.1111/gcb.12745.

Kobayashi, H. and Iwabuchi, H., 2008. A coupled 1-D atmosphere and 3-D canopy radiative transfer model for canopy reflectance, light environment, and photosynthesis simulation in a heterogeneous landscape. Remote Sensing of Environment, 112(1): 173-185, https://doi.org/10.1016/j.rse.2007.04.010.

Kong, J. et al., 2021. Evaluation of four image fusion NDVI products against in-situ spectral-measurements over a heterogeneous rice paddy landscape. Agricultural and Forest Meteorology, 297: 108255, https://doi.org/10.1016/j.agrformet.2020.108255.

Kong, J. et al., 2022. Matching high resolution satellite data and flux tower footprints improves their agreement in photosynthesis estimates. Agricultural and Forest Meteorology, 316: 108878, https://doi.org/10.1016/j.agrformet.2022.108878.

Kormann, R. and Meixner, F.X., 2001. An Analytical Footprint Model For Non-Neutral Stratification. Boundary-Layer Meteorology, 99(2): 207-224, 10.1023/A:1018991015119.

Kumari, S., Kambhammettu, B.V.N.P. and Niyogi, D., 2020. Sensitivity of Analytical Flux Footprint Models in Diverse Source-Receptor Configurations: A Field Experimental Study. Journal of Geophysical Research: Biogeosciences, 125(8): e2020JG005694, https://doi.org/10.1029/2020JG005694.

Kusak, K., Rey-Sanchez, C., Szutu, D. and Baldocchi, D., 2020. AmeriFlux US-Snf Sherman Barn, Ver. 3-5, AmeriFlux AMP, https://doi.org/10.17190/AMF/1579718.

Lai, W.-S., Huang, J.-B., Ahuja, N. and Yang, M.-H., 2017. Deep laplacian pyramid networks for fast and accurate super-resolution, Proceedings of the IEEE conference on computer vision and pattern recognition, pp. 624-632, https://doi.org/10.48550/arXiv.1704.03915.

Latte, N. and Lejeune, P., 2020. PlanetScope Radiometric Normalization and Sentinel-2 Super-Resolution (2.5 m): A Straightforward Spectral-Spatial Fusion of Multi-Satellite Multi-Sensor Images Using Residual Convolutional Neural Networks. Remote Sensing, 12(15): 2366, https://doi.org/10.3390/rs12152366.

Le Maire, G. et al., 2008. Calibration and validation of hyperspectral indices for the estimation of broadleaved forest leaf chlorophyll content, leaf mass per area, leaf area index and leaf canopy biomass. Remote sensing of environment, 112(10): 3846-3864, https://doi.org/10.1016/j.rse.2008.06.005.

Ledig, C. et al., 2017. Photo-realistic single image super-resolution using a generative adversarial network, Proceedings of the IEEE conference on computer vision and pattern recognition, pp. 4681-4690, https://doi.org/10.48550/arXiv.1609.04802.

Lee, K.-S. et al., 2020. Development of Land Surface Albedo Algorithm for the GK-2A/AMI Instrument. Remote Sensing, 12(15): 2500.

Li, F., Kustas, W.P., Anderson, M.C., Prueger, J.H. and Scott, R.L., 2008. Effect of remote sensing spatial resolution on interpreting tower-based flux observations. Remote Sensing

of Environment, 112(2): 337-349, https://doi.org/10.1016/j.rse.2006.11.032.

Li, X. et al., 2020. SFSDAF: An enhanced FSDAF that incorporates sub-pixel class fraction change information for spatio-temporal image fusion. Remote Sensing of Environment, 237: 111537, https://doi.org/10.1016/j.rse.2019.111537.

Li, X. and Strahler, A.H., 1986. Geometric-Optical Bidirectional Reflectance Modeling of a Conifer Forest Canopy. IEEE Transactions on Geoscience and Remote Sensing, GE-24(6): 906-919, 10.1109/TGRS.1986.289706.

Li, X., Xiao, J., Fisher, J.B. and Baldocchi, D.D., 2021. ECOSTRESS estimates gross primary production with fine spatial resolution for different times of day from the International Space Station. Remote Sensing of Environment, 258: 112360, https://doi.org/10.1016/j.rse.2021.112360.

Liang, S. et al., 2019. Evaluating the Spatial Representativeness of the MODerate Resolution Image Spectroradiometer Albedo Product (MCD43) at AmeriFlux Sites. Remote sensing., 11(5): 547, https://doi.org/10.3390/rs11050547.

Lindeberg, T., 1994. Scale-space theory: a basic tool for analyzing structures at different scales. Journal of Applied Statistics, 21(1-2): 225-270, https://doi.org/10.1080/757582976.

Liu, L. et al., 2020. Estimating Maize GPP using Near-infrared Radiance of Vegetation. Science of Remote Sensing: 100009, https://doi.org/10.1016/j.srs.2020.100009.

Liu, X., Liu, L., Hu, J. and Du, S., 2017a. Modeling the Footprint and Equivalent Radiance Transfer Path Length for Tower-Based Hemispherical Observations of Chlorophyll Fluorescence. Sensors (Basel), 17(5): 1131, https://doi.org/10.3390/s17051131.

Liu, X., Liu, L., Hu, J. and Du, S., 2017b. Modeling the Footprint and Equivalent Radiance Transfer Path Length for Tower-Based Hemispherical Observations of Chlorophyll Fluorescence. Sensors, 17(5): 1131, https://doi.org/10.3390/s17051131.

Lucht, W., Schaaf, C.B. and Strahler, A.H., 2000. An algorithm for the retrieval of albedo from space using semiempirical BRDF models. IEEE Transactions on Geoscience and Remote Sensing, 38(2): 977-998, https://doi.org/10.1109/36.841980.

Luo, Y., Guan, K. and Peng, J., 2018. STAIR: A generic and fully-automated method to fuse multiple sources of optical satellite data to generate a high-resolution, daily and cloud-/gap-free surface reflectance product. Remote Sensing of Environment, 214: 87-99, https://doi.org/10.1016/j.rse.2018.04.042.

Luo, Y., Guan, K., Peng, J., Wang, S. and Huang, Y., 2020. STAIR 2.0: A Generic and Automatic Algorithm to Fuse Modis, Landsat, and Sentinel-2 to Generate 10 m, Daily, and Cloud-/Gap-Free Surface Reflectance Product. Remote Sensing, 12(19): 3209, https://doi.org/doi:10.3390/rs12193209.

Lyapustin, A., Martonchik, J., Wang, Y., Laszlo, I. and Korkin, S., 2011. Multiangle implementation of atmospheric correction (MAIAC): 1. Radiative transfer basis and look-up tables. Journal of

Geophysical Research: Atmospheres, 116(D3), https://doi.org/10.1029/2010JD014985.

Mahecha, M.D. et al., 2007. Characterizing ecosystem–atmosphere interactions from short to interannual time scales. Biogeosciences, 4(5): 743–758, https://doi.org/10.5194/bg-4-743-2007.

Marcolla, B. and Cescatti, A., 2018. Geometry of the hemispherical radiometric footprint over plant canopies. Theoretical and Applied Climatology, 134(3): 981–990, https://doi.org/10.1007/s00704-017-2326-z.

Masek, J.G. et al., 2020. Landsat 9: Empowering open science and applications through continuity. Remote Sensing of Environment, 248: 111968, https://doi.org/10.1016/j.rse.2020.111968.

Matthes, J.H. et al., 2021. AmeriFlux US-Myb Mayberry Wetland, Ver. 12-5, AmeriFlux AMP, https://doi.org/10.17190/AMF/1246139.

Matthes, J.H., Sturtevant, C., Verfaillie, J., Knox, S. and Baldocchi, D., 2014. Parsing the variability in CH4 flux at a spatially heterogeneous wetland: Integrating multiple eddy covariance towers with high-resolution flux footprint analysis. Journal of Geophysical Research: Biogeosciences, 119(7): 1322–1339, https://doi.org/10.1002/2014jg002642.

McCombs, A.G., Hiscox, A.L. and Suyker, A.E., 2019. Point-to-Grid Conversion in Flux Footprints: Implications of Method Choice

and Spatial Resolution for Regional-Scale Studies. Boundary-Layer Meteorology, 172(3): 457-479, https://doi.org/10.1007/s10546-019-00455-2.

McCorkel, J., Efremova, B., Hair, J., Andrade, M. and Holben, B., 2020. GOES-16 ABI solar reflective channel validation for earth science application. Remote Sensing of Environment, 237: 111438, https://doi.org/10.1016/j.rse.2019.111438.

Mittal, A., Moorthy, A.K. and Bovik, A.C., 2012. No-Reference Image Quality Assessment in the Spatial Domain. IEEE Transactions on Image Processing, 21(12): 4695-4708, 10.1109/TIP.2012.2214050.

Miura, T., Nagai, S., Takeuchi, M., Ichii, K. and Yoshioka, H., 2019. Improved Characterisation of Vegetation and Land Surface Seasonal Dynamics in Central Japan with Himawari-8 Hypertemporal Data. Scientific Reports, 9(1): 15692, https://doi.org/10.1038/s41598-019-52076-x.

Miyato, T., Kataoka, T., Koyama, M. and Yoshida, Y., 2018. Spectral Normalization for Generative Adversarial Networks, International Conference on Learning Representations, https://doi.org/10.48550/arXiv.1802.05957.

Moffat, A.M. et al., 2007. Comprehensive comparison of gap-filling techniques for eddy covariance net carbon fluxes. Agricultural and Forest Meteorology, 147(3): 209-232, https://doi.org/10.1016/j.agrformet.2007.08.011.

Moreno-Martínez, Á. et al., 2020. Multispectral high resolution

sensor fusion for smoothing and gap-filling in the cloud. Remote Sensing of Environment, 247: 111901, https://doi.org/10.1016/j.rse.2020.111901.

Morton, D.C. et al., 2014. Amazon forests maintain consistent canopy structure and greenness during the dry season. Nature, 506(7487): 221-224, https://doi.org/10.1038/nature13006.

Myneni, R.B., Hall, F.G., Sellers, P.J. and Marshak, A.L., 1995. The interpretation of spectral vegetation indexes. IEEE Transactions on Geoscience and Remote Sensing, 33(2): 481-486, https://doi.org/10.1109/TGRS.1995.8746029.

Pastorello, G. et al., 2020. The FLUXNET2015 dataset and the ONEFlux processing pipeline for eddy covariance data. Scientific Data, 7(1): 225, https://doi.org/10.1038/s41597-020-0534-3.

Pennypacker, S. and Baldocchi, D., 2016. Seeing the Fields and Forests: Application of Surface-Layer Theory and Flux-Tower Data to Calculating Vegetation Canopy Height. Boundary-Layer Meteorology, 158(2): 165-182, https://doi.org/10.1007/s10546-015-0090-0.

Pielke Sr, R.A., 2005. Land use and climate change. Science, 310(5754): 1625-1626, https://doi.org/10.1126/science.112052.

Planet Fusion Team, 2022. Planet Fusion Monitoring Technical Specification, Version 1.0.0. In: P.F. Team (Editor), San Francisco, CA., https://support.planet.com/hc/en-

us/articles/4406292582673-Planet-Fusion-Monitoring-Technical-Specification.html.

PlanetFusionTeam, 2021. Planet Fusion Monitoring Technical Specification, Version 1.0.0-beta.3. In: P.F. Team (Editor), San Francisco, CA.

Pohl, C. and Van Genderen, J.L., 1998. Review article Multisensor image fusion in remote sensing: Concepts, methods and applications. International Journal of Remote Sensing, 19(5): 823-854, https://doi.org/10.1080/014311698215748.

Prabha, T.V., Leclerc, M.Y. and Baldocchi, D., 2008. Comparison of In-Canopy Flux Footprints between Large-Eddy Simulation and the Lagrangian Simulation. Journal of Applied Meteorology and Climatology, 47(8): 2115-2128, https://doi.org/10.1175/2008jamc1814.1.

Pringle, M.J., Schmidt, M. and Muir, J.S., 2009. Geostatistical interpolation of SLC-off Landsat ETM+ images. ISPRS Journal of Photogrammetry and Remote Sensing, 64(6): 654-664, https://doi.org/10.1016/j.isprsjprs.2009.06.001.

Proud, S.R. et al., 2014. The Normalization of Surface Anisotropy Effects Present in SEVIRI Reflectances by Using the MODIS BRDF Method. IEEE Transactions on Geoscience and Remote Sensing, 52(10): 6026-6039, https://doi.org/10.1109/TGRS.2013.2294602.

Puig-Suari, J., Turner, C. and Ahlgren, W., 2001. Development of the standard CubeSat deployer and a CubeSat class PicoSatellite,

2001 IEEE aerospace conference proceedings (Cat. No. 01TH8542). IEEE, pp. 1/347-1/353 vol. 1, https://doi.org/10.1109/AERO.2001.931726.

Qiao, K., Zhu, W., Xie, Z. and Li, P., 2019. Estimating the Seasonal Dynamics of the Leaf Area Index Using Piecewise LAI-VI Relationships Based on Phenophases. Remote Sensing, 11(6): 689.

Qiu, S., Zhu, Z. and He, B., 2019. Fmask 4.0: Improved cloud and cloud shadow detection in Landsats 4-8 and Sentinel-2 imagery. Remote Sensing of Environment, 231: 111205, https://doi.org/10.1016/j.rse.2019.05.024.

Rahmani, S., Strait, M., Merkurjev, D., Moeller, M. and Wittman, T., 2010. An adaptive IHS pan-sharpening method. IEEE Geoscience and Remote Sensing Letters, 7(4): 746-750, https://doi.org/10.1109/LGRS.2010.2046715.

Ran, Y. et al., 2016. Spatial representativeness and uncertainty of eddy covariance carbon flux measurements for upscaling net ecosystem productivity to the grid scale. Agricultural and Forest Meteorology, 230-231: 114-127, https://doi.org/10.1016/j.agrformet.2016.05.008.

Rasmussen, C.E., 2004. Gaussian Processes in Machine Learning. In: O. Bousquet, U. von Luxburg and G. Rätsch (Editors), Advanced Lectures on Machine Learning: ML Summer Schools 2003, Canberra, Australia, February 2 - 14, 2003, Tübingen, Germany, August 4 - 16, 2003, Revised Lectures. Springer Berlin Heidelberg, Berlin, Heidelberg, pp. 63-71,

10.1007/978-3-540-28650-9_4.

Reichstein, M. et al., 2005. On the separation of net ecosystem exchange into assimilation and ecosystem respiration: review and improved algorithm. Global Change Biology, 11(9): 1424-1439, https://doi.org/10.1111/j.1365-2486.2005.001002.x.

Ren, C., Wang, X., Gao, J., Zhou, X. and Chen, H., 2020. Unsupervised change detection in satellite images with generative adversarial network. IEEE Transactions on Geoscience and Remote Sensing, 59(12): 10047-10061, https://doi.org/10.1109/TGRS.2020.3043766.

Rey-Sanchez, C. et al., in prep. Assessing Methane Emission Hotspots using Footprint-Weighed Flux maps. To be submitted to Journal of Geophysical Research: Biogeosciences.

Rey-Sanchez, C., Szutu, D., Hemes, K., Verfaillie, J. and Baldocchi, D., 2021a. AmeriFlux US-Bi2 Bouldin Island corn, Ver. 11-5, AmeriFlux AMP, https://doi.org/10.17190/AMF/1419513.

Rey-Sanchez, C. et al., 2021b. AmeriFlux US-Bi1 Bouldin Island Alfalfa, Ver. 5-5, AmeriFlux AMP, https://doi.org/10.17190/AMF/1480317.

Rey-Sanchez, C. et al., 2021c. Evaluation of Atmospheric Boundary Layer Height From Wind Profiling Radar and Slab Models and Its Responses to Seasonality of Land Cover, Subsidence, and Advection. Journal of Geophysical Research: Atmospheres, 126(7): e2020JD033775, https://doi.org/10.1029/2020JD033775.

Richardson, A.D. et al., 2006. A multi-site analysis of random error in tower-based measurements of carbon and energy fluxes. Agricultural and Forest Meteorology, 136(1): 1-18, https://doi.org/10.1016/j.agrformet.2006.01.007.

Ronneberger, O., Fischer, P. and Brox, T., 2015. U-net: Convolutional networks for biomedical image segmentation, International Conference on Medical image computing and computer-assisted intervention. Springer, pp. 234-241, https://doi.org/10.1007/978-3-319-24574-4_28.

Roth, K.L., Roberts, D.A., Dennison, P.E., Peterson, S.H. and Alonzo, M., 2015. The impact of spatial resolution on the classification of plant species and functional types within imaging spectrometer data. Remote Sensing of Environment, 171: 45-57, https://doi.org/10.1016/j.rse.2015.10.004.

Roujean, J.-L., Leroy, M. and Deschamps, P.-Y., 1992. A bidirectional reflectance model of the Earth's surface for the correction of remote sensing data. Journal of Geophysical Research: Atmospheres, 97(D18): 20455-20468, https://doi.org/10.1029/92JD01411.

Rouse, J.W., Haas, R.H., Schell, J.A., Deering, D.W., 1974. Monitoring vegetation systems in the Great Plains with ERTS. Third ERTS Symposium(NASA SP-351 1): 309-317, https://ntrs.nasa.gov/citations/19740004927.

Roy, D.P., Huang, H., Houborg, R. and Martins, V.S., 2021. A global analysis of the temporal availability of PlanetScope high spatial resolution multi-spectral imagery. Remote Sensing of

Environment, 264: 112586, https://doi.org/10.1016/j.rse.2021.112586.

Roy, D.P. et al., 2016a. Characterization of Landsat-7 to Landsat-8 reflective wavelength and normalized difference vegetation index continuity. Remote Sensing of Environment, 185: 57-70, https://doi.org/10.1016/j.rse.2015.12.024.

Roy, D.P. et al., 2017. Examination of Sentinel-2A multi-spectral instrument (MSI) reflectance anisotropy and the suitability of a general method to normalize MSI reflectance to nadir BRDF adjusted reflectance. Remote Sensing of Environment, 199: 25-38, https://doi.org/10.1016/j.rse.2017.06.019.

Roy, D.P. et al., 2014a. Landsat-8: Science and product vision for terrestrial global change research. Remote Sensing of Environment, 145: 154-172, https://doi.org/10.1016/j.rse.2014.02.001.

Roy, D.P. et al., 2014b. Landsat-8: Science and product vision for terrestrial global change research. Remote sensing of Environment, 145: 154-172.

Roy, D.P. et al., 2016b. A general method to normalize Landsat reflectance data to nadir BRDF adjusted reflectance. Remote Sensing of Environment, 176: 255-271, https://doi.org/10.1016/j.rse.2016.01.023.

Ryu, Y. et al., 2012. On the temporal upscaling of evapotranspiration from instantaneous remote sensing measurements to 8-day mean daily-sums. Agricultural and Forest Meteorology, 152:

212–222, https://doi.org/10.1016/j.agrformet.2011.09.010.

Ryu, Y. et al., 2011. Integration of MODIS land and atmosphere products with a coupled–process model to estimate gross primary productivity and evapotranspiration from 1 km to global scales. Global Biogeochemical Cycles, 25(4), https://doi.org/10.1029/2011GB004053.

Ryu, Y. et al., 2010. Testing the performance of a novel spectral reflectance sensor, built with light emitting diodes (LEDs), to monitor ecosystem metabolism, structure and function. Agricultural and Forest Meteorology, 150(12): 1597–1606, https://doi.org/10.1016/j.agrformet.2010.08.009.

Ryu, Y., Berry, J.A. and Baldocchi, D.D., 2019. What is global photosynthesis? History, uncertainties and opportunities. Remote Sensing of Environment, 223: 95–114, https://doi.org/10.1016/j.rse.2019.01.016.

Ryu, Y., Jiang, C., Kobayashi, H. and Detto, M., 2018. MODIS–derived global land products of shortwave radiation and diffuse and total photosynthetically active radiation at 5km resolution from 2000. Remote Sensing of Environment, 204: 812–825, https://doi.org/10.1016/j.rse.2017.09.021.

Ryu, Y., Kang, S., Moon, S.–K. and Kim, J., 2008. Evaluation of land surface radiation balance derived from moderate resolution imaging spectroradiometer (MODIS) over complex terrain and heterogeneous landscape on clear sky days. Agricultural and Forest Meteorology, 148(10): 1538–1552, https://doi.org/10.1016/j.agrformet.2008.05.008.

Ryu, Y., Lee, G., Jeon, S., Song, Y. and Kimm, H., 2014. Monitoring multi-layer canopy spring phenology of temperate deciduous and evergreen forests using low-cost spectral sensors. Remote Sensing of Environment, 149: 227-238, https://doi.org/10.1016/j.rse.2014.04.015.

Salgueiro Romero, L., Marcello, J. and Vilaplana, V., 2020. Super-Resolution of Sentinel-2 Imagery Using Generative Adversarial Networks. Remote Sensing, 12(15): 2424, https://doi.org/10.3390/rs12152424.

Schaaf, C.B. et al., 2002. First operational BRDF, albedo nadir reflectance products from MODIS. Remote Sensing of Environment, 83(1): 135-148, https://doi.org/10.1016/S0034-4257(02)00091-3.

Schaepman-Strub, G., Schaepman, M.E., Painter, T.H., Dangel, S. and Martonchik, J.V., 2006. Reflectance quantities in optical remote sensing—definitions and case studies. Remote Sensing of Environment, 103(1): 27-42, https://doi.org/10.1016/j.rse.2006.03.002.

Scheffler, D., Hollstein, A., Diedrich, H., Segl, K. and Hostert, P., 2017. AROSICS: An automated and robust open-source image co-registration software for multi-sensor satellite data. Remote sensing, 9(7): 676, https://doi.org/10.3390/rs9070676.

Schimel, D. et al., 2015. Observing terrestrial ecosystems and the carbon cycle from space. Global Change Biology, 21(5): 1762-1776, https://doi.org/10.1111/gcb.12822.

Schmid, H.P., 1997. Experimental design for flux measurements: matching scales of observations and fluxes. Agricultural and Forest Meteorology, 87(2): 179-200, https://doi.org/10.1016/S0168-1923(97)00011-7.

Sellers, P.J., 1987. Canopy reflectance, photosynthesis, and transpiration, II. The role of biophysics in the linearity of their interdependence. Remote Sensing of Environment, 21(2): 143-183, https://doi.org/10.1016/0034-4257(87)90051-4.

Sellers, P.J., Berry, J.A., Collatz, G.J., Field, C.B. and Hall, F.G., 1992. Canopy reflectance, photosynthesis, and transpiration. III. A reanalysis using improved leaf models and a new canopy integration scheme. Remote Sensing of Environment, 42(3): 187-216, https://doi.org/10.1016/0034-4257(92)90102-P.

Seong, N.-H., Jung, D., Kim, J. and Han, K.-S., 2020. Evaluation of NDVI Estimation Considering Atmospheric and BRDF Correction through Himawari-8/AHI. Asia-Pacific Journal of Atmospheric Sciences, 56(2): 265-274, https://doi.org/10.1007/s13143-019-00167-0.

Shang, R. and Zhu, Z., 2019. Harmonizing Landsat 8 and Sentinel-2: A time-series-based reflectance adjustment approach. Remote Sensing of Environment, 235: 111439, https://doi.org/10.1016/j.rse.2019.111439.

Shannon, C.E., 1959. Coding theorems for a discrete source with a fidelity criterion. IRE Nat. Conv. Rec, 4(142-163): 1.

Shendryk, Y., Rist, Y., Ticehurst, C. and Thorburn, P., 2019. Deep

learning for multi-modal classification of cloud, shadow and land cover scenes in PlanetScope and Sentinel-2 imagery. ISPRS Journal of Photogrammetry and Remote Sensing, 157: 124-136, https://doi.org/10.1016/j.isprsjprs.2019.08.018.

Shu, H. et al., 2022. Fusing or filling: Which strategy can better reconstruct high-quality fine-resolution satellite time series? Science of Remote Sensing, 5: 100046, https://doi.org/10.1016/j.srs.2022.100046.

Shuai, Y., Masek, J.G., Gao, F. and Schaaf, C.B., 2011. An algorithm for the retrieval of 30-m snow-free albedo from Landsat surface reflectance and MODIS BRDF. Remote Sensing of Environment, 115(9): 2204-2216, https://doi.org/10.1016/j.rse.2011.04.019.

Shuai, Y., Masek, J.G., Gao, F., Schaaf, C.B. and He, T., 2014. An approach for the long-term 30-m land surface snow-free albedo retrieval from historic Landsat surface reflectance and MODIS-based a priori anisotropy knowledge. Remote Sensing of Environment, 152: 467-479, https://doi.org/10.1016/j.rse.2014.07.009.

Sishodia, R.P., Ray, R.L. and Singh, S.K., 2020. Applications of Remote Sensing in Precision Agriculture: A Review. Remote Sensing, 12(19): 3136, https://doi.org/10.3390/rs12193136.

Storey, J. et al., 2016. A note on the temporary misregistration of Landsat-8 Operational Land Imager (OLI) and Sentinel-2 Multi Spectral Instrument (MSI) imagery. Remote Sensing of Environment, 186: 121-122,

https://doi.org/10.1016/j.rse.2016.08.025.

Stow, D.A. et al., 2004. Remote sensing of vegetation and land-cover change in Arctic Tundra Ecosystems. Remote Sensing of Environment, 89(3): 281-308, https://doi.org/10.1016/j.rse.2003.10.018.

Stoy, P.C., Khan, A.M., Wipf, A., Silverman, N. and Powell, S.L., 2022. The spatial variability of NDVI within a wheat field: Information content and implications for yield and grain protein monitoring. PloS one, 17(3): e0265243, https://doi.org/10.1371/journal.pone.0265243.

Teillet, P.M., Staenz, K. and William, D.J., 1997. Effects of spectral, spatial, and radiometric characteristics on remote sensing vegetation indices of forested regions. Remote Sensing of Environment, 61(1): 139-149, https://doi.org/10.1016/S0034-4257(96)00248-9.

Tran, N.N. et al., 2020. Seasonal Comparisons of Himawari-8 AHI and MODIS Vegetation Indices over Latitudinal Australian Grassland Sites. Remote Sensing, 12(15), https://doi.org/10.3390/rs12152494

Tucker, C.J., 1979. Red and photographic infrared linear combinations for monitoring vegetation. Remote Sensing of Environment, 8(2): 127-150, https://doi.org/10.1016/0034-4257(79)90013-0.

Turner, B.L., Lambin, E.F. and Reenberg, A., 2007. The emergence of land change science for global environmental change and

sustainability. Proceedings of the National Academy of Sciences, 104(52): 20666–20671, https://doi.org/10.1073/pnas.0704119104.

Turner, M.G., O'Neill, R.V., Gardner, R.H. and Milne, B.T., 1989. Effects of changing spatial scale on the analysis of landscape pattern. Landscape Ecology, 3(3): 153–162, https://doi.org/10.1007/BF00131534.

Valach, A.C. et al., 2021. Productive wetlands restored for carbon sequestration quickly become net CO2 sinks with site–level factors driving uptake variability. PLOS ONE, 16(3): e0248398, https://doi.org/10.1371/journal.pone.0248398.

Verma, M. et al., 2015. Improving the performance of remote sensing models for capturing intra– and inter–annual variations in daily GPP: An analysis using global FLUXNET tower data. Agricultural and Forest Meteorology, 214–215: 416–429, https://doi.org/10.1016/j.agrformet.2015.09.005.

Vermote, E.F., Tanre, D., Deuze, J.L., Herman, M. and Morcette, J., 1997. Second Simulation of the Satellite Signal in the Solar Spectrum, 6S: an overview. IEEE Transactions on Geoscience and Remote Sensing, 35(3): 675–686, https://doi.org/10.1109/36.581987.

Walther, S. et al., 2022. Technical note: A view from space on global flux towers by MODIS and Landsat: the FluxnetEO data set. Biogeosciences, 19(11): 2805–2840, https://doi.org/10.5194/bg–19–2805–2022.

Wang, J. et al., 2022. A new object-class based gap-filling method for PlanetScope satellite image time series. Remote Sensing of Environment, 280: 113136, https://doi.org/10.1016/j.rse.2022.113136.

Wang, J. et al., 2020a. Multi-scale integration of satellite remote sensing improves characterization of dry-season green-up in an Amazon tropical evergreen forest. Remote Sensing of Environment, 246: 111865, https://doi.org/10.1016/j.rse.2020.111865.

Wang, J.A. et al., 2020b. Extensive land cover change across Arctic-Boreal Northwestern North America from disturbance and climate forcing. Global Change Biology, 26(2): 807-822, https://doi.org/10.1111/gcb.14804.

Wang, X., Chen, J.M. and Ju, W., 2020c. Photochemical reflectance index (PRI) can be used to improve the relationship between gross primary productivity (GPP) and sun-induced chlorophyll fluorescence (SIF). Remote Sensing of Environment, 246: 111888, https://doi.org/10.1016/j.rse.2020.111888.

Wang, X., Xie, L., Dong, C. and Shan, Y., 2021. Real-esrgan: Training real-world blind super-resolution with pure synthetic data, Proceedings of the IEEE/CVF International Conference on Computer Vision, pp. 1905-1914, https://doi.org/10.1109/ICCVW54120.2021.00217.

Wang, X. et al., 2018a. Esrgan: Enhanced super-resolution generative adversarial networks, Proceedings of the European

conference on computer vision (ECCV) workshops, pp. 0-0, https://doi.org/10.1007/978-3-030-11021-5_5.

Wang, Z., Jiang, K., Yi, P., Han, Z. and He, Z., 2020d. Ultra-dense GAN for satellite imagery super-resolution. Neurocomputing, 398: 328-337, https://doi.org/10.1016/j.neucom.2019.03.106.

Wang, Z., Schaaf, C.B., Sun, Q., Shuai, Y. and Román, M.O., 2018b. Capturing rapid land surface dynamics with Collection V006 MODIS BRDF/NBAR/Albedo (MCD43) products. Remote Sensing of Environment, 207: 50-64, https://doi.org/10.1016/j.rse.2018.02.001.

Wanner, W., Li, X. and Strahler, A.H., 1995. On the derivation of kernels for kernel-driven models of bidirectional reflectance. Journal of Geophysical Research: Atmospheres, 100(D10): 21077-21089, https://doi.org/10.1029/95JD02371.

Weiss, D.J. et al., 2014. An effective approach for gap-filling continental scale remotely sensed time-series. ISPRS Journal of Photogrammetry and Remote Sensing, 98: 106-118, https://doi.org/10.1016/j.isprsjprs.2014.10.001.

Weiss, D.J. and Crabtree, R.L., 2011. Percent surface water estimation from MODIS BRDF 16-day image composites. Remote Sensing of Environment, 115(8): 2035-2046, https://doi.org/10.1016/j.rse.2011.04.005.

Wheeler, K.I. and Dietze, M.C., 2019. A Statistical Model for Estimating Midday NDVI from the Geostationary Operational Environmental Satellite (GOES) 16 and 17. Remote Sensing,

11(21), https://doi.org/10.3390/rs11212507.

Wheeler, K.I. and Dietze, M.C., 2021. Improving the monitoring of deciduous broadleaf phenology using the Geostationary Operational Environmental Satellite (GOES) 16 and 17. Biogeosciences, 18(6): 1971–1985, https://doi.org/10.5194/bg-18-1971-2021.

Woodcock, C.E. and Strahler, A.H., 1987. The factor of scale in remote sensing. Remote Sensing of Environment, 21(3): 311–332, https://doi.org/10.1016/0034-4257(87)90015-0.

Wu, G. et al., 2020. Radiance-based NIRv as a proxy for GPP of corn and soybean. Environmental Research Letters, 15(3): 034009, https://doi.org/10.1088/1748-9326/ab65cc.

Wu, P., Shen, H., Zhang, L. and Göttsche, F.-M., 2015. Integrated fusion of multi-scale polar-orbiting and geostationary satellite observations for the mapping of high spatial and temporal resolution land surface temperature. Remote Sensing of Environment, 156: 169–181, https://doi.org/10.1016/j.rse.2014.09.013.

Wulder, M.A., Hermosilla, T., White, J.C., Hobart, G. and Masek, J.G., 2021. Augmenting Landsat time series with Harmonized Landsat Sentinel-2 data products: Assessment of spectral correspondence. Science of Remote Sensing, 4: 100031, https://doi.org/10.1016/j.srs.2021.100031.

Wulder, M.A. et al., 2019. Current status of Landsat program, science, and applications. Remote Sensing of Environment, 225: 127–

147, https://doi.org/10.1016/j.rse.2019.02.015.

Xiao, J., Fisher, J.B., Hashimoto, H., Ichii, K. and Parazoo, N.C., 2021. Emerging satellite observations for diurnal cycling of ecosystem processes. Nature Plants, 7(7): 877-887, https://doi.org/10.1038/s41477-021-00952-8.

Yan, D., Zhang, X., Yu, Y. and Guo, W., 2016a. A Comparison of Tropical Rainforest Phenology Retrieved From Geostationary (SEVIRI) and Polar-Orbiting (MODIS) Sensors Across the Congo Basin. IEEE Transactions on Geoscience and Remote Sensing, 54(8): 4867-4881, https://doi.org/10.1109/TGRS.2016.2552462.

Yan, L. and Roy, D.P., 2018. Large-Area Gap Filling of Landsat Reflectance Time Series by Spectral-Angle-Mapper Based Spatio-Temporal Similarity (SAMSTS). Remote Sensing, 10(4): 609, https://doi.org/10.3390/rs10040609.

Yan, L. and Roy, D.P., 2020. Spatially and temporally complete Landsat reflectance time series modelling: The fill-and-fit approach. Remote Sensing of Environment, 241: 111718, https://doi.org/10.1016/j.rse.2020.111718.

Yan, L., Roy, D.P., Zhang, H., Li, J. and Huang, H., 2016b. An Automated Approach for Sub-Pixel Registration of Landsat-8 Operational Land Imager (OLI) and Sentinel-2 Multi Spectral Instrument (MSI) Imagery. Remote Sensing, 8(6): 520, https://doi.org/10.3390/rs8060520.

Yang, H. and E, W., 2021. Generalization error of GAN from the

discriminator's perspective. Research in the Mathematical Sciences, 9(1): 8, https://doi.org/10.1007/s40687-021-00306-y.

Yang, H. and E, W., 2022. Generalization and Memorization: The Bias Potential Model. In: B. Joan, H. Jan and Z. Lenka (Editors), Proceedings of the 2nd Mathematical and Scientific Machine Learning Conference. PMLR, Proceedings of Machine Learning Research, pp. 1013--1043, https://doi.org/10.48550/arXiv.2011.14269.

Yang, K. et al., 2018. Sun-induced chlorophyll fluorescence is more strongly related to absorbed light than to photosynthesis at half-hourly resolution in a rice paddy. Remote Sensing of Environment, 216: 658-673, https://doi.org/10.1016/j.rse.2018.07.008.

Yang, X. and Lo, C., 2000. Relative radiometric normalization performance for change detection from multi-date satellite images. Photogrammetric engineering and remote sensing, 66(8): 967-980.

Yazici, Y., Foo, C.S., Winkler, S., Yap, K.H. and Chandrasekhar, V., 2020. Empirical Analysis Of Overfitting And Mode Drop In Gan Training, 2020 IEEE International Conference on Image Processing (ICIP), pp. 1651-1655, 10.1109/ICIP40778.2020.9191083.

Yeom, J.-m. et al., 2018. Monitoring paddy productivity in North Korea employing geostationary satellite images integrated with GRAMI-rice model. Scientific Reports, 8(1): 16121,

https://doi/org/10.1038/s41598-018-34550-0.

Yeom, J.-M. and Kim, H.-O., 2013. Feasibility of using Geostationary Ocean Colour Imager (GOCI) data for land applications after atmospheric correction and bidirectional reflectance distribution function modelling. International Journal of Remote Sensing, 34(20): 7329-7339, 10.1080/2150704X.2013.817708.

Yeom, J.-M., Roujean, J.-L., Han, K.-S., Lee, K.-S. and Kim, H.-W., 2020. Thin cloud detection over land using background surface reflectance based on the BRDF model applied to Geostationary Ocean Color Imager (GOCI) satellite data sets. Remote Sensing of Environment, 239: 111610, https://doi.org/10.1016/j.rse.2019.111610.

Yin, G. et al., 2019. Retrieval of High Spatiotemporal Resolution Leaf Area Index with Gaussian Processes, Wireless Sensor Network, and Satellite Data Fusion. Remote Sensing, 11(3): 244, https://doi/org/doi:10.3390/rs11030244.

Yost, M.A. et al., 2017. Long-term impact of a precision agriculture system on grain crop production. Precision Agriculture, 18(5): 823-842, https://doi.org/10.1007/s11119-016-9490-5.

Zeng, Y. et al., 2019. A practical approach for estimating the escape ratio of near-infrared solar-induced chlorophyll fluorescence. Remote Sensing of Environment, 232: 111209, https://doi.org/10.1016/j.rse.2019.05.028.

Zhang, H. et al., 2021. Retrieving high-resolution surface

photosynthetically active radiation from the MODIS and GOES-16 ABI data. Remote Sensing of Environment, 260: 112436, https://doi.org/10.1016/j.rse.2021.112436.

Zhang, Y. et al., 2018. On the relationship between sub-daily instantaneous and daily total gross primary production: Implications for interpreting satellite-based SIF retrievals. Remote Sensing of Environment, 205: 276-289, https://doi.org/10.1016/j.rse.2017.12.009.

Zhang, Z. et al., 2020. Reduction of structural impacts and distinction of photosynthetic pathways in a global estimation of GPP from space-borne solar-induced chlorophyll fluorescence. Remote Sensing of Environment, 240: 111722, https://doi.org/10.1016/j.rse.2020.111722.

Zhou, W., Bovik, A.C., Sheikh, H.R. and Simoncelli, E.P., 2004. Image quality assessment: from error visibility to structural similarity. IEEE Transactions on Image Processing, 13(4): 600-612, https://doi.org/10.1109/TIP.2003.819861.

Zhu, X., Cai, F., Tian, J. and Williams, T.K.-A., 2018. Spatiotemporal Fusion of Multisource Remote Sensing Data: Literature Survey, Taxonomy, Principles, Applications, and Future Directions. Remote Sensing, 10(4): 527, https://doi.org/10.3390/rs10040527.

Zhu, X., Chen, J., Gao, F., Chen, X. and Masek, J.G., 2010. An enhanced spatial and temporal adaptive reflectance fusion model for complex heterogeneous regions. Remote Sensing of Environment, 114(11): 2610-2623,

https://doi.org/10.1016/j.rse.2010.05.032.

Zhu, X. and Helmer, E.H., 2018. An automatic method for screening clouds and cloud shadows in optical satellite image time series in cloudy regions. Remote Sensing of Environment, 214: 135–153, https://doi.org/10.1016/j.rse.2018.05.024.

Zhu, X. et al., 2016. A flexible spatiotemporal method for fusing satellite images with different resolutions. Remote Sensing of Environment, 172: 165–177, https://doi.org/10.1016/j.rse.2015.11.016.

Zhu, X., Liu, D. and Chen, J., 2012. A new geostatistical approach for filling gaps in Landsat ETM+ SLC–off images. Remote Sensing of Environment, 124: 49–60, https://doi.org/10.1016/j.rse.2012.04.019.

Zhukov, B., Oertel, D., Lanzl, F. and Reinhackel, G., 1999. Unmixing–based multisensor multiresolution image fusion. IEEE Transactions on Geoscience and Remote Sensing, 37(3): 1212–1226, https://doi.org10.1109/36.763276.

Ziliani, M.G. et al., 2022. Early season prediction of within–field crop yield variability by assimilating CubeSat data into a crop model. Agricultural and Forest Meteorology, 313: 108736, https://doi.org/10.1016/j.agrformet.2021.108736.

Abstract in Korea

시공간 해상도 향상을 통한 식생 변화 모니터링

공주원
서울대학교 환경대학원 협동과정 조경학
논문지도교수: 류영렬

육상 생태계에서 대기권과 생물권의 상호 작용을 이해하기 위해서는 식생 변화의 모니터링이 필요하다. 이 때, 위성영상은 지표면을 관측하여 식생지도를 제공할 수 있지만, 지표변화의 상세한 정보는 구름이나 위성 이미지의 공간 해상도에 의해 제한되었다. 또한 위성영상의 시공간 해상도가 식생지도를 통한 광합성 모니터링에 미치는 영향은 완전히 밝혀지지 않았다.

본 논문에서는 고해상도 식생 지도를 일단위로 생성하기 위성 영상의 시공간 해상도를 향상시키는 것을 목표로 하였다. 고해상도 위성영상을 활용한 식생 변화 모니터링을 시공간적으로 확장하기 위해 1) 정지궤도 위성을 활용한 영상융합을 통해 시간해상도 향상, 2) 적대적생성네트워크를 활용한 공간해상도 향상, 3) 시공간해상도가 높은 위성영상을 토지피복이 균질하지 않은 공간에서 식물 광합성 모니터링을 수행하였다. 이처럼, 위성기반 원격탐지에서 새로운 기술이 등장함에 따라 현재 및 과거의 위성영상은 시공간 해상도 측면에서 향상되어 식생 변화의 모니터링 할 수 있다.

제2장에서는 정지궤도위성영상을 활용하는 시공간 영상융합으로 식물의 광합성을 모니터링 했을 때, 시간해상도가 향상됨을 보였다. 시공간 영상융합 시, 구름탐지, 양방향 반사 함수 조정, 공간 등록, 시공간 융합, 시공간 결측치 보완 등의 과정을 거친다. 이 영상융합 산출물은 경작관리 등으로 식생 지수의 연간 변동이 큰 두 장소(농경지와 낙엽수림)에서 평가하였다. 그 결과, 시공간 영상융합 산출물은 결측치 없이

현장관측을 예측하였다 (R^2 = 0.71, 상대 편향 = 5.64% 농경지; R^2 = 0.79, 상대 편향 = −13.8%, 활엽수림). 시공간 영상융합은 식생 지도의 시공간 해상도를 점진적으로 개선하여, 식물 생장기동안 위성영상이 현장 관측을 과소 평가를 줄였다. 영상융합은 높은 시공간 해상도로 광합성 지도를 일간격으로 생성하기에 이를 활용하여 위성 영상의 제한된 시공간 해상도로 밝혀지지 않은 식물변화의 과정을 발견하길 기대한다.

식생의 공간분포은 정밀농업과 토지 피복 변화 모니터링을 위해 필수적이다. 고해상도 위성영상으로 지구 표면을 관측하는 것을 용이하게 해졌다. 특히 Planet Fusion은 초소형위성군 데이터를 최대한 활용해 데이터 결측이 없는 3m 공간 해상도의 지표 표면 반사도이다. 그러나 과거 위성 센서(Landsat의 경우 30~60m)의 공간 해상도는 식생의 공간적 변화를 상세 분석하는 것을 제한했다. 제3장에서는 Landsat 데이터의 공간 해상도를 향상하기 위해 Planet Fusion 및 Landsat 8 데이터를 사용하여 이중 적대적 생성 네트워크(the dual RSS−GAN)를 학습시켜, 고해상도 정규화 식생 지수(NDVI)와 식물 근적외선 반사(NIRv)도를 생성하는 한다. 타워기반 현장 식생지수(최대 8년)와 드론기반 초분광지도로 the dual RSS−GAN의 성능을 대한민국 내 두 대상지(농경지와 활엽수림)에서 평가했다. The dual RSS−GAN은 Landsat 8 영상의 공간해상도를 향상시켜 공간 표현을 보완하고 식생 지수의 계절적 변화를 포착했다(R^2> 0.96). 그리고 the dual RSS−GAN은 Landsat 8 식생 지수가 현장에 비해 과소 평가되는 것을 완화했다. 현장 관측에 비해 이중 RSS−GAN과 Landsat 8의 상대 편향 값 각각 −0.8% 에서 −1.5%, −10.3% 에서 −4.6% 였다. 이러한 개선은 Planet Fusion의 공간정보를 이중 RSS−GAN로 학습하였기에 가능했다. 헤당 연구 결과는 Landsat 영상의 공간 해상도를 향상시켜 숨겨진 공간 정보를 제공하는 새로운 접근 방식이다.

고해상도에서 식물 광합성 지도는 토지피복이 복잡한 공간에서 탄소 순환 모니터링시 필수적이다. 그러나 Sentinel−2, Landsat 및 MODIS와 같이 태양 동조 궤도에 있는 위성은 공간 해상도가 높거나 시간 해상

도 높은 위성영상만 제공할 수 있다. 최근 발사된 초소형위성군은 이러한 해상도 한계을 극복할 수 있다. 특히 Planet Fusion은 초소형위성 자료의 시공간 해상도로 지표면을 관측할 수 있다. 4장에서, Planet Fusion 지표반사도를 이용하여 식생에서 반사된 근적외선 복사(NIRvP)를 3m 해상도 지도를 일간격으로 생성했다. 그런 다음 미국 캘리포니아주 새크라멘토-샌 호아킨 델타의 플럭스 타워 네트워크 데이터와 비교하여 식물 광합성을 추정하기 위한 NIRvP 지도의 성능을 평가하였다. 전체적으로 NIRvP 지도는 습지의 잦은 수위 변화에도 불구하고 개별 대상지의 식물 광합성의 시간적 변화를 포착하였다. 그러나 대상지 전체에 대한 NIRvP 지도와 식물 광합성 사이의 관계는 NIRvP 지도를 플럭스 타워 관측범위와 일치시킬 때만 높은 상관관계를 보였다. 관측범위를 일치시킬 경우, NIRvP 지도는 식물 광합성을 추정하는 데 있어 현장 NIRvP보다 우수한 성능을 보였다. 이러한 성능 차이는 플럭스 타워 관측범위를 일치시킬 때, 연구 대상지 간의 NIRvP-식물 광합성 관계의 기울기가 일관성을 보였기 때문이다. 본 연구 결과는 위성 관측을 플럭스 타워 관측범위와 일치시키는 것의 중요성을 보여주고 높은 시공간 해상도로 식물 광합성을 원격으로 모니터링하는 초소형위성군 자료의 잠재력을 보여준다.

Keyword: 초해상도 (Super-resolution), 위성원격탐사, 광합성, 큐브위성, 정지궤도위성, 적대적생성네트워크(GAN)

Student Number: 2019-39602

Acknowledgements

I would like to thank my advisor, Prof. Youngryel Ryu of Department of Landscape Architecture and Rural System Engineering at Seoul National University. He led me to the science world and the scientific network for next step of my career.

The chairman and member of the committee, Prof. Dongkun Lee, Prof. Junsuk Kang, Prof. Youngkeun Song, and Ph.D. Minseok Kang, provide insightful comments and question. I would also like to acknowledge Ph.D. Benjamin Dechant, Ph.D. Jiangong Liu, Ph.D. Zilong Zhong, and M.S. Sungchan Jeong as the second reader of my research results, and I am gratefully indebted to their comments on this dissertation. I also want to thank all my current and previous lab members – Ph.D. Jongmin Kim, Ph.D. Yourum Huang, Ph.D. Jeehwan Bae, Ph.D. Yulin Yan, M.S. Wonseok Choi, M.S Jeongho Lee, M.S. Sangjun Lee, Ryeongseob Kwon, Tackang Yang – for constructive discussions and field works during the past four years.

I must express gratitude to my parents – Ph.D. Dukam Kong, Ph.D. Haesun Song–, my sister –Hyunwook Kong –, and her family –Seungmin Lee, Doyeon Lee, Siyoon Lee– for their support through prayers, encouragement, and smile. When I was frustrated and having a hard time, I was able to continue my research with their support and smile. From my parents' career, I have learned how to be loyal and trustworthy person in daily life. By the dedication of my parents, I could free myself from the financial burden until now. With their love and guidance, I could accomplish every step of my research life.

Last, I am much obliged to Suan Lee for being with me. The existence of herself inspired my daily research life and I could refine my research with her fresh mind and idea. It was precious time to me when she tried to understand my research until the end. Moreover, I could maintain a healthy mind and body as I mirrored her to myself.